UAB
Universitat Autònoma de Barcelona

Superinductive Ultrastrong Couplings in Superconducting Quantum Circuits

Alba Torras Coloma

Superinductive Ultrastrong Couplings in Superconducting Quantum Circuits

Alba Torras Coloma

Director: Pol Forn-Díaz
Tutora: Marta Gonzalez Silveira

Programa de Doctorat en Física

Universitat Autònoma de Barcelona

Cerdanyola del Vallès, 2025

Preface

I joined the newly established QCT lab at the end of 2020. Back then, everyone was still wearing a face mask and strict rules were imposed on the number of people allowed in the rooms. At that moment, the QCT lab had one dilution fridge with hardly a microwave line installed. During the upcoming months, a lot of efforts were put to set up the lab. This included designing new pieces for the refrigerator, preparing microwave cables, building furniture... It was not until the summer of 2021 that we managed to get the different cleanroom access to start fabricating devices. It took a lot of trials to get the first working resonators, we did not have the recipes properly calibrated and the Plassys had only recently been installed. It was also around that time that I started *playing* with the Plassys to fabricate granular aluminum and that we started the very long collaboration to prepare the first NitrAl films. It was around 2022 that we managed to observe the first superconducting transition of a NitrAl film. That same year, I also had the opportunity to visit the Néel Institute in Grenoble for a month. I met amazing people and learned a lot about experiments very different from to the ones we were conducting in Barcelona. In the upcoming years, I recall spending many hours in the cleanroom, the problems with the Plassys were almost constant and the Josephson junctions were not working properly. It was not until the end of 2024 that I managed to fabricate the first working flux qubit device of the lab. It took many many trials and a lot of efforts. The device was not on target, but we soon saw that it might still show ultrastrong coupling features. Many devices followed that one with the misfortune that some of the delicate structures broke at some point or another of the fabrication process. The time to complete the PhD is not infinite (fortunately) and at some point one has to move on and start writing the manuscript. Hopefully, the recipes, codes, analysis etc. developed during this time help the future generations of students of the QCT lab.

This journey would not have been possible if back in 2020 Pol had not accepted the request of that young photonics student to join the lab. I am sincerely very grateful for the opportunity that he granted me and for the guidance provided during these years. From him, I am taking home some very valuable lessons that go beyond science and important values that made me grow both as a person and as a researcher. Although he is one of the busiest people I have ever met, he has always been able to find time to discuss any issue and take action. I had to

admit that if I enjoyed the PhD and managed to get to this point, it is in part, thanks to him. Gràcies Pol!

These nearly five years have also brought a number of good friendships, especially those forged in the lab. Here I need to start with Luca, whom I like to call my *PhD twin*. We started the same day and have gone through the same ups and downs. Whenever I felt down, he had a kind word (or a cold beer) to cheer me up. I learned a lot about superconducting circuits from him, but the best discussions have always been about Napolitan food. I have always admired his conviction and his strength, he has always been able to pull everything together and keep moving forward. I hope we can continue sharing beers, gossip and food for many years after the PhD. However, if I became fluent in Italian, that is not only thanks to Luca, but also to Elia. From him I learned to be resourceful and how to make ingenious *chapuzas*. But more importantly, he has always been around to provide guidance, advice, and help. On a side note, I have been fascinated from day 1 by his passion for mushroom hunting and his willingness to teach how to distinguish properly *ceps*. Thanks to him, we have all became mycologist apprentices.

I cannot forget to mention David L., he was the very first PhD student in the group and the first to start tracing the path for the others. His notes on circuit quantization, videos on qubit measurements, diagonalization codes... Everything made our life easier. I have always admired his Galician patience and his passion for cheese and delicious food. I have to admit that I would not have been able to obtain half of the results without his help. Similarly, I would like to make a special mention to my cleanroom *Padawan*, Ari. Although she only recently started the PhD, she has been around the lab since summer 2021. During this time, I had the pleasure of working with her in multiple projects. She is an incredible fast learner, motivated and always willing to help and learn. I had a lot of fun in the cleanroom with her and she definitely made the long EBL sessions more bearable.

These years around the lab also brought a long list of people in and out. David E. and Yifei, we shared many hours and fun times during the early years in the lab. You are both incredible hard-working people that I have admired from the first day. There is a long list that follows: Manel, Guille, Fabian, Chris, Ramiro, Fabio, Cata, María H., Daniel, Nandini... and many more people from Qilimanjaro. I have learned a lot from you and I am grateful for the help you have provided during these years. I cannot forget either the people from the module: Juan, Pablo, Niraj, Quim... We became a small family in IFAE and it has always been fun to go for *asados* and drinks together.

If I managed to fabricate working devices in the cleanroom, it is also thanks to many technicians who have been repeatedly willing to help. Thank you for the very valuable tips Albert, Javi, Hector, Luís, Xevi, Raúl... In the same line,

I am also very grateful to all our collaborators for the insights and comments provided on our research. In particular, I would like to thank the colleagues from Grenoble for always giving us a hand whenever we had problems with the evaporator. Thank you Nico, Gwen, Sam, Shelender, Giulio, Quintin, Wäel, Dorian,...

Going though a PhD requires mental strength but also learning to disconnect. If I have managed to go though all this is also thanks to the friends I made outside the lab. A special mention goes to Pere and all the colleagues from *El Rei de la Màgia*. Thinking about ingenious tricks and discussing about magic has become a fun way to disconnect from physics.

Close to my heart are all my dear friends from uni: Mercè, Carla, Roger, Santi, Carlos, Raúl and Marta. We all took similar paths at very distant places. Even though we live very far from each other, the online calls, visits and trips made it feel like you were next door. You were always there to listen and help during good and bad times and your support made this PhD journey much easier. Thank you!

Finally, I cannot conclude without expressing my gratitude to my family, who have been supporting my journey in science since the very first day. Gràcies a tots.

Summary

One of the simplest systems to study light-matter interactions in superconducting quantum circuits consists of a superconducting qubit coupled to a resonator. In general, for quantum computing and other qubit-related applications, the qubit-resonator coupling is designed well below the bare frequencies of the individual elements, allowing for a set of approximations which yield a relatively simple framework. As the coupling increases, the approximations begin to fail and the system enters the so-called ultrastrong coupling regime (USC), where the physics of the system have been largely unexplored.

In this thesis, we introduce superinductor materials as an approach to couple a flux qubit ultrastrongly to a resonator. Usually, achieving the USC regime has led to circuit designs that impaired qubit coherence. Hence, we study a new approach with superinductors to circumvent these complications. The large kinetic inductance provided by these materials allows one to design large shared linear inductors while keeping relatively small qubit loops and low persistent currents. We present a device consisting of a C-shunted 3-Josephson junction flux qubit galvanically coupled to a resonator with a wire of granular Aluminum (grAl). We derive the necessary Hamiltonians and numerical methods to analyze the theoretical spectrum and obtain an estimate of the coupling coefficient of the system. Additionally, we provide the details of the developed multi-step qubit fabrication recipe which allows to adjust each component to guarantee that the final chip is in the USC regime. In terms of design, special attention is put to obtain a qubit-resonator system close to resonance, at a range of measurable frequencies, and coherent enough.

We report the spectral measurements of a flux-qubit resonator device with low persistent current and a large shared inductance. We observe USC features such as the effect of counter-rotating terms, evidenced as a Bloch-Siegert shift of 23 MHz. The coupling coefficient is large enough to be in the perturbative USC regime with $g/\omega_r \simeq 0.13$. The measured circuit serves as a proof-of-concept for the possibility of reaching large qubit-resonator couplings with low persistent current qubits and opens the door to coherent studies in the USC regime.

The use of superinductors to study USC also motivates the search for new materials with superior properties to grAl. We present the development a novel superconducting material based on Alumium nitridization which can be obtained by sputtering Aluminum in different N_2/Ar fractional flows. In this thesis, we an-

alyze the main superconducting properties of nitridized Aluminum (NitrAl) thin films of 100 nm. We report the measurement of enhanced critical temperatures reaching $T_c = (3.38 \pm 0.01)$ K and resilience to in-plane magnetic fields well above 1 T. Similarly to granular aluminum, we observe a dome-shape like distribution of the critical temperature versus room-temperature resistivity. Additionally, we estimate a kinetic inductance ranging from 1 pH/□ for the least resistive samples to 400 pH/□ for higher resistivity films. Finally, we present the first steps towards the characterization of losses of NitrAl and the implementation of the material as a superinductor in superconducting quantum circuit technologies.

Resum

Un dels sitemes més simples per estudiar la interacció llum-matèria en circuits superconductors quàntics consisteix en un qubit superconductor acoblat a un ressonador. En general, per aplicacions de computació quàntica o altres aplicacions relacionades amb qubits, l'acoblament entre el qubit i el ressonador es dissenya amb valors molt per sota de les freqüències naturals individuals del sistema, permetent així aproximacions que resulten en un marc matemàtic relativament simple. A mesura que l'acoblament augmenta, les aproximacions comencen a fallar i el sistema entra el que es coneix com a règim d'acoblament ultrafort (USC de les sigles en anglès), on la física del sistema encara es troba en gran part inexplorada.

En aquesta tesi proposem materials superinductors com a un nou enfoc per acoblar un qubit de flux de manera ultraforta a un ressonador. Generalment, aconseguir acoblaments en el rang d'USC ha comportat dissenys que perjudicaven la coherència dels qubits. Per eludir complicacions, introduïm aquest nou enfoc amb superinductors. L'elevada inductància cinètica associada a aquests materials permet dissenyar grans inductàncies compartides a la vegada que es mantenen dimensions del qubit relativament petites i corrents persistents baixes. Així mateix, presentem un disseny que consisteix en un qubit de flux de 3 unions Josephson amb derivació capacitiva acoblat galvànicament a un ressonador mitjançant un fil d'Alumini granular (grAl). Derivem els Hamiltonians necessaris així com els mètodes numèrics per analitzar de manera teòrica l'espectre i obtenir una estimació del coeficient d'acoblament del sistema. D'altra banda, proporcionem els detalls de la recepta de fabricació de qubits consistent en múltiples passos que permeten assegurar que el xip final es trobi en el règim d'USC.

Mostrem també les mesures de l'espectre d'un sistema qubit de flux ressonador amb corrent persistent baixa i una inductància compartida elevada. Observem elements característics del règim USC, com ara l'efecte dels termes contra-rotants que s'evidencia com a un desplaçament de Bloch-Siegert de 23 MHz. El coeficient d'acoblament és prou gran per entrar al rang pertorbatiu del règim USC amb un valor $g/\omega_r \simeq 0.13$. El circuit mesurat serveix com a prova de concepte per demostrar la possibilitat d'arribar a acoblaments ultraforts qubit-ressonador amb corrents persistents baixes i obre la possibilitat de realitzar estudis coherents al règim d'USC.

L'ús de superinductors per estudiar el règim USC també motiva la cerca de

nous materials amb propietats superiors a les del grAl. Així mateix, presentem el desenvolupament d'un nou material superconductor basat en nitridació d'Alumini i que es pot obtenir mitjançant la deposició per pulverització catòdica d'Alumini en differents fraccions de flux de N_2/Ar. En aquesta tesi, anlitzem les principals propietats superconductores de capes fines de 100 nm d'Alumini nitridat (NitrAl). Mostrem mesures de l'increment de temperatures crítiques que arriben al valor màxim de $T_c = (3.38 \pm 0.01)$ K i resil·liències a camps magnètics en el pla per sobre d'1 T. De la mateixa manera que en grAl, observem una distribució en foma de cúpula de la temperatura crítica en funció de la resistivitat a tempertura ambient. Addicionalment, estimem la inductància cinètica que va des d'1 pH/□ per les mostres menys resistives, fins a 400 pH/□ per aquelles capes més resistives. Finalment, presentem els primers passos en la caracterització de les pèrdues del NitrAl i la implementació del material com a superconductor i superinductor en tecnologies de circuits quàntics.

Resumen

Uno de los sistemas más simples para estudiar la interacción luz-materia en circuitos superconductores cuánticos se compone de un cúbit superconductor acoplado a un resonador. En general, para aplicaciones de computación cuántica u otras aplicaciones relacionadas con qubits, el acoplamiento entre qubit y resonador se diseña con valores muy por debajo de las frecuencias naturales individuales del sistema, permitiendo así aproximaciones que resultan en un marco matemático relativamente simple. A medida que el acoplamiento aumenta, las aproximaciones empiezan a fallar y el sistema entra dentro de lo que se conoce como régimen de acoplamiento ultrafuerte (USC, de sus siglas en inglés), donde la física del sistema se encuentra en gran parte inexplorada.

En esta tesis, proponemos materiales superinductores como un nuevo enfoque para acoplar un cúbit de flujo de manera ultrafuerte a un resonador. Generalmente, conseguir acoplamientos en el rango de USC ha implicado diseños que perjudicaban la coherencia de los cúbits. Para eludir complicaciones, introducimos este nuevo enfoque con superinductores. La elevada inductancia cinética asociada con estos materiales permite diseñar grandes inductancias compartidas a la vez que se mantienen dimensiones del cúbit relativamente pequeñas y corrientes persistentes bajas. Asimismo, presentamos un diseño que consiste en un cúbit de flujo de 3 uniones Josephson con derivación capacitiva acoplado galvánicamente a un resonador mediante un hilo de Aluminio granular (grAl). Derivamos los Hamiltonianos necesarios, así como los métodos numéricos para analizar de manera teórica el espectro y obtener una estimación del coeficiente de acoplamiento del sistema. Por otro lado, proporcionamos los detalles de la receta de fabricación de cúbits, consistente en múltiples pasos y que permite asegurar que el chip final se encuentra en el rango de USC.

Mostramos también las medidas del espectro de un sistema cúbit de flujo resonador con una corriente persistente baja y una inductancia compartida elevada. Observamos elementos característicos del régimen USC, como por ejemplo, el efecto de los términos contra-rotantes, que se evidencia como un desplazamiento de Bloch-Siegert de 23 MHz. El coeficiente de acoplamiento es lo suficientemente grande para entrar en el rango perturbativo del régimen de USC, con un valor de $g/\omega_r \simeq 0.13$. El circuito medido sirve como prueba de concepto para demostrar la posibilidad de llegar a acoplamientos cúbit-resonador ultrafuertes con corrientes persistentes bajas y abre la posibilidad de realizar estudios coherentes en

el régimen USC.

El uso de superinductores para estudiar el régimen de USC también motiva la búsquda de nuevos materiales con propiedades superiores a las del grAl. Así, presentamos el desarrollo de un nuevo material superconductor basado en la nitridación de Aluminio y que se puede obtener mediante la deposición por pulverización catódica de Aluminio en distintas fracciones de flujo de N_2/Ar. En esta tesis, analizamos las principales propiedades superconductoras de capas finas de 100 nm de Aluminio nitridado (NitrAl). Mostramos las medidas del incremento de temperaturas críticas, que llegan a un valor máximo de $T_c = (3.38 \pm 0.01)\,\mathrm{K}$, y resiliencias a campos magnéticos en el plano por encima de 1 T. Del mismo modo que en grAl, observamos una distribución en forma de cúpula de la temperatura crítica en función de la resistividad a temperatura ambiente. Adicionalmente, estimamos la inductancia cinética, que toma valores entre 1 pH/□ para las muestras menos resistivas y 400 pH/□ para aquellas capas más resistivas. Finalmente, presentamos los primeros pasos en la caracterización de las pérdidas del NitrAl y la implementación del material como superconductor y superinductor en tecnologías de circuitos cuánticos.

List of publications

- Superconducting nitridized-aluminum thin films. ***Alba Torras-Coloma****, Leyre Martínez de Olcoz, Eva Céspedes, Elia Bertoldo, David López-Núñez, Sagar Paul, Wolfgang Wernsdorfer, Gemma Rius, Pol Forn-Díaz.* Supercond. Sci. Technol. 37 035017 (2024)

- Direct detection of down-converted photons spontaneously produced at a single Josephson junction. *Dorian Fraudet, Izak Snyman, Denis M. Basko, Sébastien Léger, Théo Sépulcre, Arpit Ranadive, Gwenael Le Gal,* ***Alba Torras-Coloma****, Wiebke Guichard, Serge Florens and Nicolas Roch.* Phys. Rev. Lett. 134, 013804 (2025)

- Magnetic penetration depth of Aluminum thin films. *David López-Núñez,* ***Alba Torras-Coloma****, Queralt Portell Montserrat, Elia Bertoldo, Luca Cozzolino, Giovanni Alberto Ummarino, Alessio Zaccone,, Gemma Rius, M. Martínez, P. Forn-Díaz* Supercond. Sci. Technol (accepted, 2025)

- Superinductor-based ultrastrong coupling in a superconducting circuit. ***Alba Torras-Coloma****, Luca Cozzolino, Ariadna Gómez-del-Pulgar-Martínez, Elia Bertoldo, P. Forn-Díaz.* (preprint arXiv:2507.09339)

- Effective circuit QED models in the ultrastrong coupling regime. ***Alba Torras-Coloma****, P. Forn-Díaz, J.J Garcia-Ripoll.* (in preparation)

Contents

Chapter 1

Introduction and Summary

Contents

The early developments in the study of light-matter interaction revolved around light and atomic systems. Although these systems provided a large variety of groundbreaking observations, they are limited by the nature of atoms and optical cavities [Wal+06]. Recently, with the fast development of new quantum technologies, the study of light-matter interaction has taken a new perspective. Platforms such as superconducting quantum circuits have shown great potential to study fundamental quantum optics phenomena unattainable by atomic systems. The research in this direction is also motivated by the fast development of quantum computing, where an in depth understanding of fundamental light-matter interactions is of importance to develop reliable qubit control, measurement, and couplings.

Light-matter interactions with couplings of the order of the frequencies of the system are a clear example where superconducting qubits can offer an advantage

over atomic systems. The possibility of engineering each of the elements that form the system allows to design artificial atoms with the desired properties and interactions with arbitrarily large strengths. Although ultrastrong couplings in superconducting quantum circuits have been extensively studied over the past two decades, there is still a long list of experimentally unexplored phenomena, mostly related to the coherence of the system [For+19; Fri+19]. Coherent superconducting quantum systems in the ultrastrong coupling regime are an ongoing quest. The improvement of fabrication techniques and the development of new superconducting materials has opened the door to new and more robust design possibilities. This is the case of superinductors, structures able to provide a large linear inductance without the need for intricate geometric structures such as thin and narrow meandered wires. Systems in the ultrastrong coupling regime, where there is a need for large shared inductances, can greatly benefit from superinductors to reduce design constrains and potentially improve coherence.

The aim of this first chapter is to introduce the basic concepts needed to understand the core topics of this thesis: the ultrastrong coupling regime of light-matter interaction and superinductors. We start in Sec. 1.1 by giving an overview on superconducting qubits with a special focus on flux qubits. We continue in Sec. 1.2 by reviewing the basics of light-matter interaction. This section reveals the convenience of superconducting quantum circuits to study regimes of interaction reaching the ultrastrong coupling regime and how to use them to observe unexplored phenomena. In Sec. 1.3, we introduce the concept of superinductors and their most common implementations. Finally, we conclude the chapter with an overview of the thesis organization putting into context the different topics that will be discussed throughout the text.

1.1 Superconducting qubits

The quantum harmonic oscillator constitutes one of the fundamental systems in quantum mechanics. In the context of superconducting quantum circuits, it can be realized by connecting an inductor together with a capacitor. The resulting potential is harmonic, and the spectrum of the system consists of equally spaced energy levels given by $E_n = \hbar\omega(n + 1/2)$ with ω the resonance frequency of the oscillator. The fact that all transitions are equally spaced makes it very challenging to single out two levels and operate them as a qubit.

Superconducting qubits, instead, rely on anharmonic oscillator potentials built from superconducting circuit elements such as Josephson junctions, capacitors and inductors [Kra+19]. Josephson junction are non-linear inductive elements characterized by the Josephson inductance L_J which can be derived

from the Josephson equations [Jos62] and takes the following form,

$$L_{\mathrm{J}} = \frac{\Phi_0}{2\pi I_{\mathrm{c}} \cos\varphi} = \frac{\Phi_0}{2\pi\sqrt{I_c^2 - I^2}}, \tag{1.1}$$

where Φ_0 is the superconducting flux quantum, I_{c} is the critical current of the junction and φ the phase difference between the wave functions of the two superconductors that constitute the junction. The associated non-linear potential is described by

$$U_{\mathrm{JJ}} = -E_J \cos\varphi, \tag{1.2}$$

where $E_J = \Phi_0 I_C/2\pi$ is the Josephson energy. The addition of the Josephson junction into the well-known harmonic oscillator potential modifies the energy spectrum. The energy difference between the lowest and first excited state will be different from the one between the first and second excited state and, similarly, for the rest of the consecutive transitions. In other words, $\hbar\omega_{0,1} \neq \hbar\omega_{n,n+1}$. Therefore, the anharmonic potential makes the different transitions distinguishable allowing to single out for example, the two lowest states to build a qubit [Rip22].

1.1.1 Types of superconducting qubits

There is a plethora of superconducting qubit types. The choice of circuit elements, their arrangement and their values can define qubits with very different properties, including the resonance frequency, anharmonicity, and resilience to certain types of noise. These properties arise from the difference between intrinsic energy scales of the different circuit elements. These energies consist of the Josephson energy $E_J = \Phi_0 I_{\mathrm{c}}/2\pi$, with I_{c} the critical current of the Josephson junction, the capacitance charging energy $E_C = e^2/2C$, with C the capacitance associated to a capacitor or Josephson junction, and the inductive energy $E_L = \Phi_0^2/(4\pi^2 L)$ with L the inductance associated to an inductor [Kja+20].

Traditionally, qubits have been categorized in two big groups, charge and flux, depending on which is the best well-defined quantum number of the circuit and what elements can modify their eigenstates. Charge qubits can be built connecting a superconducting island to a large reservoir by means of a Josephson junction. The charge is well defined in the island and becomes a good quantum number. Flux qubits, on the other hand, have a well-defined phase. These qubits are built from at least a superconducting loop interrupted by a Josephson junction and an inductor and the resulting eigenstates can be modified by the application of an external flux. Examples of charge qubits include the well-known Cooper-pair box ($E_C \gg E_J$) [Nak+99] and the transmon ($E_J/E_C \sim 30-100$) [Koc+07]. Similarly, examples of established flux qubits are the persistent current qubit

($E_J \gg E_C$) [Orl+99] and the fluxonium qubit ($E_J > E_C$, $E_J \gg E_L$) [Man+09]. In the following section, we provide a more in depth description of flux qubits and their properties.

1.1.2 Flux qubits

There are multiple geometries and approaches to build flux qubits. In general, all flux qubits are built from at least a superconducting loop interrupted by an inductive element and one or more Josephson junctions. In these qubits, the states can be described by circulating currents in the loop and the properties of the system can be modified by threading an external magnetic flux through the superconducting loop.

There is a long list of flux qubits built from different circuit elements and having different ranges of operation. The most well-known examples are the radio-frequency superconducting quantum interference device (rf-SQUID), the C-shunted flux qubit and the fluxonium. Examples of circuit schematics for these types of flux qubits are shown in Fig. 1.1. We start this section presenting the simplest case of a flux qubit consisting of a Josephson junction in parallel with an inductor, the rf-SQUID. The rf-SQUID serves as a preamble for the C-shunted 3-Josephson junction flux qubit which will be of importance to understand the devices presented in Ch. 3 and 4.

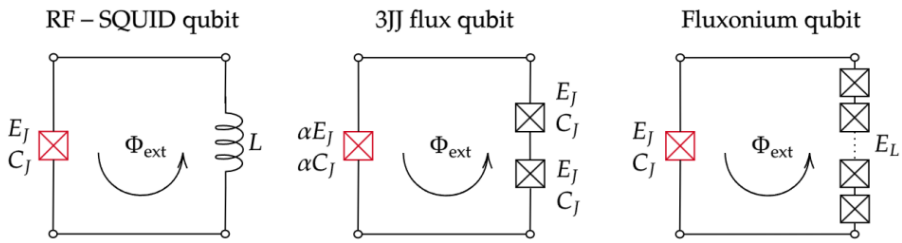

Figure 1.1: Circuit schematics for three different flux qubits: rf-SQUID, 3-Josephson junction flux qubit and fluxonium qubit. Φ_{ext} is the external flux threaded through the loop.

rf-SQUID

Probably one of the simplest anharmonic potentials that can be built from Josephson junctions, capacitors and inductors is the one of the rf-SQUID. The rf-SQUID [Sil+67] consists on a closed superconducting loop interrupted by a

Josephson junction in series with an inductor (see the left panel in Fig. 1.1). The Hamiltonian of this qubit is

$$\hat{\mathcal{H}}_{\text{rf}} = 4E_C\hat{n}^2 + \frac{E_L}{(2\pi)^2}\frac{\hat{\varphi}^2}{2} + E_J\cos(\hat{\varphi} + 2\pi f), \tag{1.3}$$

where E_J and E_C are, respectively, the Josephson and capacitance charging energies of the Josephson junction, E_L is the inductive energy associated to the linear inductor L, and $f = \Phi_{\text{ext}}/\Phi_0$, with Φ_{ext} the external flux applied to the loop.

An intuitive description of the physics of the rf-SQUID can be derived from a simple analysis of its potential energy. The potential consists of a cosine function modulated by a parabolic term. The application of an external flux, f, modifies the overall shape of the potential and, thus, the properties of the system. At zero flux, the minima of the cosine potential aligns with the parabolic term, leading to an effective anharmonic single-well potential. The interesting case comes with the application of an external flux. The flux produces a shift in the cosine term which is maximal for $f = 0.5$. At this flux value, the system has a double-well potential with two equal minima. The lowest two energy states of the system are degenerate and the solutions can be interpreted as a superposition of opposite circulating currents of identical magnitude with wavefunctions localized on each potential well [Rip22]. The system is *frustrated*, thus, there is no favorable current circulation direction in the loop to oppose the external flux $f = 0.5$.

Although the rf-SQUID has a large number of applications as a magnetic flux detector [Cla+06], it presents some challenges when used as a qubit. Since the device contains only one Josephson junction, achieving high reproducibility is difficult. Small deviations in fabrication will significantly impact E_J and, thus, the spectrum of the qubit. On the other hand, the rf-SQUID requires a large loop inductance which implies either using large qubit loops, making the system more sensitive to flux noise [Bra+20], or including materials with high kinetic inductance in the fabrication process [Pel+18].

3-Josephson junction flux qubit

The 3-Josephson junction (3JJ) flux qubit presents a compact design and provides more versatility than the rf-SQUID. The first version of the 3JJ flux qubit was introduced by *Orlando et al.* in 1999 under the name of *persistent-current qubit* [Orl+99] and the first experimental demonstration of the device was carried out by *van der Wal et al.* in year 2000 [Van+00]. The circuit of this qubit consists of a loop interrupted by three Josephson junctions where one of them is made a factor α smaller (see the central panel in Fig. 1.1). The loop inductance is assumed to be small compared with the inductance from the Josephson junctions

and it is neglected during the circuit Hamiltonian derivation. The Hamiltonian of the qubit is

$$\begin{aligned}\hat{\mathcal{H}}_{3\mathrm{JJ}} = 4E_C \left(\frac{1+\alpha}{1+2\alpha}(\hat{n}_1^2 + \hat{n}_2^2) + \frac{2\alpha}{1+2\alpha}\hat{n}_1\hat{n}_2 \right) + \\ - E_J \left(\cos\hat{\varphi}_1 + \cos\hat{\varphi}_2 + \alpha\cos\left(\hat{\varphi}_1 + \hat{\varphi}_2 + 2\pi f\right)\right)\end{aligned} \tag{1.4}$$

where, E_J and E_C are, respectively, the Josephson and capacitance charging energies of the big junctions, α denotes the area ratio between small and big junctions, $f = \Phi_{\mathrm{ext}}/\Phi_0$ with Φ_{ext} the external flux applied to the loop, $\hat{n}_i$ is the charge number operator and $\hat{\varphi}_i$ the phase operator associated to the $i-$th junction.

Depending on the value of α, the 3JJ flux qubit can have very different energy potential landscapes and properties. For values of $\alpha < 0.5$, the potential energy has a single well and the system is said to be in the *plasmon* regime. In this regime, the qubit displays weak anharmonicity and weak flux dispersion. When $\alpha = 0.5$ the system is in the *quarton* regime. For this particular value, the potential can be approximated by a quartic potential ($\sim \hat{\varphi}^4$). The qubit can maintain large anharmonicity ($\sim 1\,\mathrm{GHz}$) and high coherence while keeping a reasonable operating frequency ($\sim 4\,\mathrm{GHz}$). Qubits in the *quarton* regime have also been used as couplers for qubit readout applications[Ye+21; Ye+24]. Finally, the *fluxon* regime arises for $0.5 < \alpha < 1$. In this regime, the potential energy consists of a double-well potential and the qubit is characterized by a strong anharmonicity. [Yan+20]. In Fig. 1.2, we provide three examples of potentials in the *plasmon*, *quarton* and *fluxon* regime, respectively.

In this thesis, we are interested in the *fluxon* regime ($0.5 < \alpha < 1$). To understand the nature of this qubit and its solutions it is convenient to rewrite the potential term in Eq. (1.4) in terms of the sum and difference of phases across the junctions, $\hat{\varphi}_\pm = (\hat{\varphi}_1 \pm \hat{\varphi}_2)/2$, and perform a similar potential study to that given for the rf-SQUID. The potential term of the Hamiltonian under this transformation reads,

$$U_{3\mathrm{JJ}}(\hat{\varphi}_+, \hat{\varphi}_-) = -E_J \left(2\cos\left(\hat{\varphi}_+\right)\cos\left(\hat{\varphi}_-\right) - \alpha\cos\left(2\hat{\varphi}_+ + 2\pi f\right)\right). \tag{1.5}$$

The first term $2\cos\left(\hat{\varphi}_+\right)\cos\left(\hat{\varphi}_-\right)$ has minima at $\hat{\varphi}_\pm = 0$ which can be modified by the second term $\alpha\cos\left(2\hat{\varphi}_+ + 2\pi f\right)$ by applying an external magnetic flux. Similarly to the rf-SQUID case, for $f = 0.5$ the total potential has a double well (see Fig. 1.2 for $\alpha = 0.9$) and the system is frustrated. The qubit will have two stable degenerate states corresponding to each minima of the potential with opposite sign for the phase ($\hat{\varphi}_1 = \hat{\varphi}_2 = \pm\hat{\varphi}^*$), or, similarly, opposite sign circulating currents in the loop [Rip22; Paa09].

3JJ flux qubits are characterized in terms of the qubit gap Δ_{q} and the per-

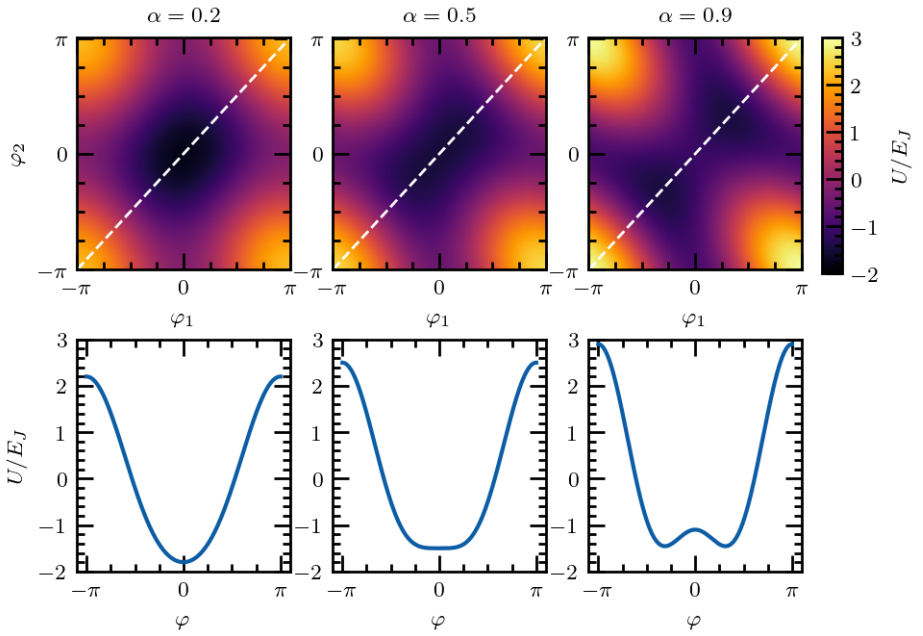

Figure 1.2: Normalized potential (U/E_J) for a 3-Josephson junction flux qubit for three different values of α obtained at the sweetspot $f = 0.5$. The white dashed line indicates the cut $\varphi = \varphi_1 = \varphi_2$ used to obtain the potential profile depicted in the bottom panels.

sistent current I_p. Δ_q represents the qubit energy difference at the sweetspot ($f = 0.5$), while the persistent current gives the magnitude of the circulating current in the qubit ring and can be estimated with $\pm\frac{1}{\Phi_0}\frac{\partial E}{\partial f}$. The expression takes the positive sign for $f > 0.5$ and negative for $f < 0.5$. Since the 3JJ flux qubit can be interpreted in terms of circulating currents, we can also define the associated qubit magnetic dipole moment $\mu = 2I_p$ which will have two preferred directions perpendicular to the qubit plane given by the current direction [Pla07; Rip22].

In general, flux qubits have a high anharmonicity and it is then possible to approximate the system and just keep the two lowest eigenstates. The resulting effective two-level Hamiltonian can be represented in the persistent current basis $\{|L\rangle, |R\rangle\}$,

$$\hat{\mathcal{H}}_{qb} = -\frac{1}{2}\hat{\sigma}_z\epsilon + \frac{1}{2}\Delta_\mathrm{q}\hat{\sigma}_x, \tag{1.6}$$

where $\epsilon = 2I_{\mathrm{p}}(\Phi_{\mathrm{ext}} - \Phi_0/2)$ is the magnetic energy of the qubit. Using these parameters, the frequency of the qubit at an arbitrary external flux point is given by $\hbar\omega_q = \sqrt{\Delta_{\mathrm{q}}^2 + \epsilon^2}$. This expression will become particularly useful when describing the qubit-resonator interaction in Ch. 3.

The original design for a 3JJ flux qubit suffers from low coherence and poor reproducibility [Yos+06; Cha+22]. Asymmetries in the Josephson junctions derived from the fabrication process have a significant impact on the final properties of the qubit and have been known to be one of the major sources of decoherence [Bur+05]. A demonstrated method to improve the design is to include a capacitor shunting the small junction, similar to the approach used in transmons to improve their coherence times. Even though the shunting capacitance decreases the anharmonicity of the qubit, it provides a larger effective capacitance for the small junction and improves reproducibility [Yan+16; Cór+11; Ste+10]. The qubit potential is essentially the same as the one presented in Eq. (1.4) with the change $\alpha \to \alpha + \frac{C_{\mathrm{sh}}}{C_J}$ in the kinetic term.

1.2 Light-matter interaction in superconducting quantum circuits

Circuit Quantum Electrodynamics (circuit QED) studies the interaction of quantized electromagnetic fields with superconducting qubits and other circuit elements such as resonators [Bla+21]. The field was born as an analogy to Cavity QED, which considers the interaction of atoms with electromagnetic field modes confined in high reflective optical cavities [Wal+06]. In circuit QED, superconducting qubits play the role of artificial atoms, and resonators provide the tool to confine an electromagnetic mode. Originally, cQED considered fields in the microwave frequency range, but this can be extended both to low, kHz, frequency cavities as well as THz systems. Superconducting quantum circuits have evolved tremendously since the first experimental observation of coherent oscillations with a superconducting qubit [Nak+99]. Nowadays, new types of qubits, improved fabrication, control and understanding of the system have opened the door to the study quantum optics phenomena in a novel range of parameters unattainable by cavity QED systems. In this section, we provide the basic tools to understand light-matter interaction in superconducting quantum circuits, and we give an overview of the different regimes of interaction that can be explored with such a platform.

1.2.1 The Quantum Rabi Model

The description of the simplest form of light-matter interaction in a quantum system has been known for almost a century. Back in 1936, Isidor I. Rabi proposed a model, which nowadays carries his name, to describe the dipolar interaction of a two-level atom with a classical electromagnetic field [Rab36]. The semi-classical description was able to predict phenomena such as Rabi oscillations and light-shifts, but it failed to describe quantitatively processes such as spontaneous emission [Scu+97; Gry+10]. The fully quantized version of the Rabi model was not introduced until 27 years later by the work of E. T. Jaynes and F. W. Cummings [Jay+63]. The nowadays called Quantum Rabi model introduces the quantized version of the electromagnetic field and its physics is given by the Hamiltonian

$$\hat{\mathcal{H}}_{\mathrm{QRM}} = \hbar\frac{\Omega_q}{2}\hat{\sigma}_z + \hbar\omega_r\hat{a}^\dagger\hat{a} + \hbar g\hat{\sigma}_x(\hat{a} + \hat{a}^\dagger), \tag{1.7}$$

where Ω_q and ω_r are the bare two-level system and electromagnetic field frequencies, respectively, g is the coupling coefficient, $\hat{\sigma}_i$ are the Pauli matrices describing the two-level atom and $\hat{a}^\dagger$, $\hat{a}$ are the creation and annihilation operators associated with the electromagnetic field mode. Although it may appear a simple Hamiltonian, many theoretical studies have made efforts into studying the integrability and solvability of Eq. (1.7). It was not until 2011 that D. Braak proposed an analytical solution to the spectrum of the QRM [Bra11]. Still, the analytical expression is fairly complex and the physics of the model are difficult to grasp from its form.

The QRM has traditionally been used to describe the interaction of single atoms interacting with optical cavities. In these systems, the coupling g is much smaller than the atom's and cavity's bare frequencies, thus satisfying the condition $g \ll \Omega_q, \omega_r$. In this regime of interaction, one can apply the so-called rotating wave approximation (RWA), which consists of neglecting the counter-rotating terms $\hat{a}^\dagger\hat{\sigma}_+$ and $\hat{a}\hat{\sigma}_-$, where $\hat{\sigma}_\pm = (\hat{\sigma}_x \pm i\hat{\sigma}_y)/2$ are the atomic raising and lowering operators [Rip22; For+19]. The remaining interaction terms $(\hat{\sigma}_-\hat{a}^\dagger + \hat{\sigma}_+\hat{a})$ describe the interaction in terms of absorption and emission of photons. The resulting Hamiltonian after the elimination of the counter-rotating terms is the so-called Jaynes-Cummings (JC) Hamiltonian [Jay+63],

$$\hat{\mathcal{H}}_{\mathrm{JC}} = \hbar\frac{\Omega_q}{2}\hat{\sigma}_z + \hbar\omega_r\hat{a}^\dagger\hat{a} + \hbar g(\hat{\sigma}_+\hat{a} + \hat{\sigma}_-\hat{a}^\dagger). \tag{1.8}$$

Contrary to the QRM, the JC model is relatively simple, conserves the number of excitations, and can be solved analytically in a convenient form. The eigenstates of Eq. (1.8) can be described in terms of the bare qubit ($|g\rangle$ $|e\rangle$) and resonator ($|n\rangle$) states $\{|e,n\rangle,\ |g,n+1\rangle\}$, and the energies have an analytical form [Gry+10].

The JC model represents the workhorse in applications of superconducting qubits dealing with qubit-resonator interactions. A well-known example is quantum computing.

The assumption that the coupling coefficient is significantly smaller than the bare frequencies of the system is not necessarily true for all systems described by the Quantum Rabi model. In platforms were the two-level atom and the cavity properties can be fully engineered, one can reach regimes were g is comparable to the frequencies of the system, invalidating the RWA. In this limit, the system enters the so-called ultrastrong (USC) coupling regime and the complete treatment of the Quantum Rabi model is needed to provide accurate predictions of the eigenstates, eigenvalues and dynamical response of the system. As we will see later in this section, superconducting quantum circuits are a clear example of a platform where couplings can be engineered beyond the Jaynes-Cummings Hamiltonian limit.

1.2.2 Ultrastrong coupling regime of light-matter interaction

In the previous section, we have seen that when the coupling coefficient approaches the bare frequencies of the system, the counter rotating terms $\sim (\hat{a}\hat{\sigma}_- + \hat{a}^\dagger\hat{\sigma}_+)$ become sizeable and cannot be neglected. This limit defines the USC regime and extends for couplings $0.1 < g/\omega_r < 1$. Beyond $g/\omega_r > 1$, the system enters a different regime with distinctive features known as the deep strong coupling regime (DSC). The physics in the USC regime gradually changes for increasing couplings. In fact, two distinctive sub-regimes can be identified depending on how the counter-rotating terms are treated and what approximate Hamiltonians can be used [Ros+17b]. They are the perturbative and the non-perturbative USC regimes.

The perturbative USC regime comprises couplings between $0.1 < g/\omega_r \lesssim 0.3$. In this range of interactions, one can consider a perturbative expansion of the counter-rotating terms as an off-resonant field. The physics in the non-perturbative USC regime is well described by the so-called Bloch-Siegert (BS) Hamiltonian [Bea+11; For+10],

$$\begin{aligned}\hat{\mathcal{H}}_{BS} = \hbar\frac{\Omega_q}{2}\hat{\sigma}_z + \hbar\omega_r\left(\hat{N}+\frac{1}{2}\right) + \hbar\omega_{BS}\left(\hat{\sigma}_z\left(\hat{N}+\frac{1}{2}\right)-\frac{1}{2}\right) + \\ + \hbar(g(\hat{N})\hat{a}^\dagger\hat{\sigma}_- + \hat{a}\hat{\sigma}_+ g(\hat{N}))\end{aligned} \tag{1.9}$$

where $\hat{N} = \hat{a}^\dagger\hat{a}$ is the harmonic oscillator number operator, $\omega_{BS} \equiv g^2/(\omega_r + \Omega_q)$ is the Bloch-Siegert shift and $g(\hat{N}) \equiv -g(1 - \hat{N}\omega_{BS}/(\omega_r + \Omega_q))$ is the renormalized coupling constant [Blo+40]. The BS shift quantifies the magnitude of

the perturbative effect of the counter-rotating terms on the system spectra. In fact, these terms produce a repulsion between the atomic and harmonic oscillator levels defined by the JC model. In particular, the oscillator (atomic) transition is shifted a magnitude ω_{BS} downwards (upwards) in frequency.

As the coupling increases to the regime $0.3 < g/\omega_r < 1.0$, the perturbative treatment of the counter-rotating terms fails and the system enters the so-called non-perturbative USC regime. The two-level atom and the electromagnetic field mode become highly hybridized, and one needs to treat the complete QRM (Eq. (1.7)) for arbitrary couplings, where new physics arises. A direct consequence of the presence of the counter-rotating terms is the breaking of the conservation of excitation number. This opens the possibility to absorb/emit multiple photons at the same time in a coherent and reversible manner [Gar+16]. Another consequence is the possibility to have transitions between dressed states containing contributions from various numbers of photons and atomic excitations. This gives rise to possibly one of the most striking particularities of the non-perturbative USC regime, which is the squeezed ground state with a finite number of photons. These photons are sometimes referred as virtual photons because they cannot be directly detected. There are proposals to extract and detect this photons that include using lower uncoupled levels [Gia+24; Fal+19], ancillary qubits [Lol+15], or a fast modulation of the interaction strength [De +09].

In order to illustrate the spectral differences between the coupling regimes presented in this section, Fig. 1.3 provides the spectrum of a qubit-resonator system calculated with the QRM and the JC model for different interaction strengths (see Sec. 1.2.3 for more details on qubit-resonator couplings). As the coupling increases, the differences between models become more pronounced. We observe an increasing shift between JC and QRM in the resonator transition, a direct consequence of the effect of counter-rotating terms. For couplings in the non-perturbative USC regime (third panel), the difference between models becomes significant even outside the qubit sweetspot ($\Phi_{\text{ext}} = 0.5\Phi_0$).

For completeness, let us consider the case of coupling coefficients beyond $g/\omega_r > 1.0$. Under these circumstances, the interaction becomes the dominant energy scale of the system and a new regime of interaction, the DSC regime, arises. One of the main characteristics of this regime is the collapse and revival of the initial population [Cas+10]. The approximate Hamiltonians and physics of the DSC system differ from the USC and require a specific treatment which is beyond the scope of this thesis.

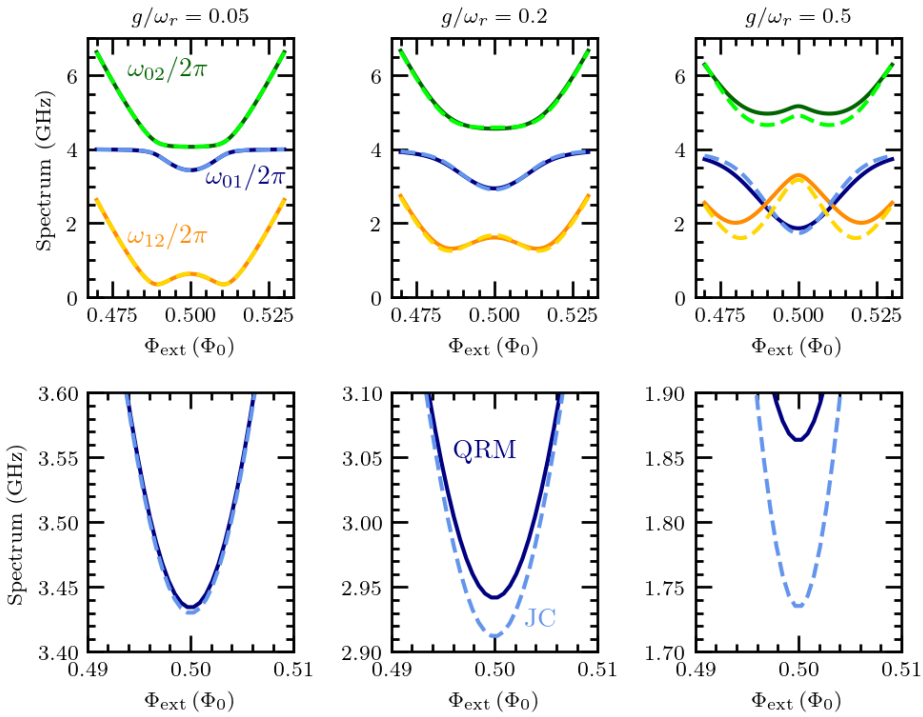

Figure 1.3: Qubit-resonator spectra calculated using the QRM (solid) and JC (dashed) for different couplings g. The parameters used for the simulation are $\Delta_{\rm q}/h = 3.5\,\text{GHz}$, $I_{\rm p} = 30\,\text{nA}$ and $\omega_r/2\pi = 4\,\text{GHz}$. The upper panels show the transitions corresponding to the first two energy levels of the system, while the lower panels are a zoom near the sweetspot for ω_{01}.

1.2.3 Ultrastrong coupling regime with superconducting qubits

In circuit QED, qubits play the role of artificial atoms while resonators provide the tool to confine an electromagnetic mode. There are numerous ways of coupling qubits to resonators. The arrangement and circuit elements used to couple them will depend on the strength of the interaction required, the application and the type of qubit used. For example, ultrastrong inductive couplings will be more suited for flux qubits since their eigenstates correspond to well-defined persistent current states, while ultrastrong capacitive couplings will be more suited for charge-based qubits. In both instances, the description of the interaction is of a

dipolar type and can be rewritten in a similar form to the QRM (see Ch. 3 for an example of a flux qubit-resonator coupling).

Inductors are the preferred choice to study USC in flux qubit-resonator systems. Several approaches can be followed to couple both circuits. Figure 1.4 depicts different inductive coupling strategies: (a) by sharing a Josephson junction, (b) by placing the two circuit elements close to each other (mutual geometric inductance) or (c) by sharing a linear inductor. In the following sections we describe each in more detail and we give some insights on how to achieve the USC regime with each of them.

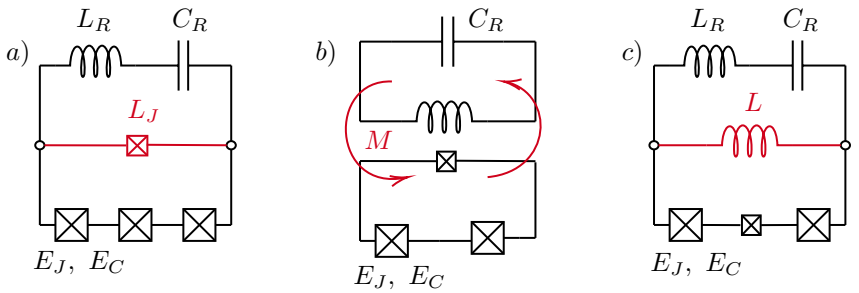

Figure 1.4: Different flux qubit-resonator inductive couplings. (a) Sharing one of the qubit Josephson junctions, (b) mutual geometric inductance and (c) sharing a linear inductor.

Shared Josephson junction

The natural choice to boost the qubit-resonator coupling is to use a shared circuit element, such as a Josephson junction, that can provide a large inductance L_J. There are namely two approaches. The first one consists of sharing a large Josephson junction in the linear regime. This is a junction with critical current I_c much larger than the current flowing through it. Under this condition, the junction can be approximated as a linear inductor with $L_\mathrm{J} = \Phi_0/2\pi I_\mathrm{c}$, with, the dipolar interaction and the coupling coefficient being directly proportional to L_J [Nie+10]. The second approach depicted in Fig. 1.4 (a) consists of sharing one of the qubit junctions with the resonator circuit. The coupling in this case depends on the magnetic dipole moment of the qubit which can be calculated as the expectation value $\langle 0|\hat{\varphi}|1\rangle$, where $\hat{\varphi}$ is the phase across the shared junction [Per+13]. Although it is straightforward to obtain a large coupling using Josephson junctions, they provide a set of inconveniences. Specifically, they can introduce stray nonlinearities in the coupling and may introduce noise in the form of two-level system defects localized in the insulator of the junction [Bil+17] and

quasiparticle tunneling [Ris+13].

The use of shared Josephson junctions has been the most ubiquitous approach to attain qubit-resonator couplings extending from the USC regime up to the DSC regime. Examples include the work from *T. Niemczyk et al.*, which is one of the first experimental demonstrations of USC using superconducting qubits. In [Nie+10], the qubit shares a large Josephson junction between the qubit loop and a transmission line resonator providing $g/\omega_r \sim 0.12$. More recent works have been able to explore couplings in the non-perturbative USC regime [For+17] and, even the DSC regime [Yos+17b; Yos+17a] using shared qubit junctions or SQUIDs.

Mutual inductance

Consider two superconducting loops placed next to each other (Fig. 1.4). The mutual inductance between the two loops is defined as the magnetic flux through the first loop produced per unit current circulating in the second loop. Equivalently to the classical case, this quantity depends on the geometry and the distance between loops [Cot+91]. In quantum annealing, qubit-qubit and qubit-resonator interactions are often mediated by the mutual inductance between the circuits located in different chips [Ros+17a; Web+17].

The caveat of the mutual inductance approach is that in order to boost the coupling, one requires large qubit loops [For+19]. Furthermore, large qubit loops make the qubit more sensitive to flux noise since the noise scales with the perimeter of the loop [Bra+20], making it very challenging to have coherent qubit-resonator systems. In general, mutual inductive couplings are not considered as a practical approach to reach qubit-resonator couplings in the USC regime [For+19].

Shared linear inductor

The last option depicted in Fig. 1.4 (c) comprises the use of a shared linear inductor between qubit and resonator. For inductances of the order of the resonator and qubit junction inductances, the coupling depends on the magnetic dipole moment of the qubit which can be calculated as the expectation value $\langle 0|\hat{\varphi}|1\rangle$, where $\hat{\varphi}$ is the phase across the shared inductor [Per+13]. This approach offers several advantages. First, the inductor is linear so we can avoid stray non-nonlinearities coming from the shared circuit element. Secondly, we can benefit from superconducting materials showcasing large kinetic inductance to provide a large coupling inductance in a relatively small space. These materials are called superinductors and will be presented in the next section. Even though these materials can have a non-linear component, it can be reduced by adjusting the geometry of the design and film resistivity [Mal+18; Ho +12]. The disadvantage of using large shared linear inductors is that they introduce a harmonic term in the qubit potential.

Depending on the qubit design, this can lead to lower qubit persistent currents, possibly decreasing the coupling strength.

To our knowledge, only two experimental proposals used a shared linear inductor as qubit-resonator coupler reaching the USC regime [For+10; Che+17]. The work from *P. Forn-Díaz et al.* used a shared thin Al wire connecting both circuits and providing an estimated inductance of $L \sim 25\,\mathrm{pH}$, enough to reach $g/\omega_r \sim 0.1$. To circumvent the relatively low shared inductance, they used a qubit with an extremely large persistent current ($\sim 500\,\mathrm{nA}$), with the consequent detrimental effect on qubit coherence. The approach followed by the work from *Z. Chen et al.* is similar to [For+10]. The qubit is designed with a large persistent current $I_p \sim 250\,\mathrm{nA}$ and a sufficiently large loop to have enough inductance to reach a coupling $g/\omega_r \sim 0.1$.

Linear galvanic couplings have been realized beyond the scope of USC regime studies. For example, in the work from *A. Fedorov et al.* [Fed+10], a gradiometric flux qubit is coupled galvanically to a resonator with an Al line. The system reached the strong coupling regime with an estimated coupling of $g/\omega_r \sim 0.05$. More recently, in [Gei+24; Ihs+25], the authors proposed a fluxonium qubit-resonator galvanic coupling based purely on kinetic inductance. Unlike the previous cases, the galvanic coupling is implemented in granular Aluminum, a material displaying a high kinetic inductance.

1.3 Superinductors

In Sec. 1.1 we have introduced different circuit elements typically used in superconducting quantum circuits, namely inductors, capacitors and Josephson junctions. In this section, we will focus on superinductors, a new building block for superconducting qubit technologies used in high-impedance qubits such as the fluxonium [Man+09; Grü+19] and in designs of high-impedance environments [Fra+25; Lég+19; Zap+24]. Superinductors are superconducting elements with impedances (Z) similar or greater than the resistance quantum $R_Q = h/(2e)^2 \simeq 6.5\,\mathrm{k\Omega}$. Besides the large impedance, in order to operate in qubit circuits, superinductors are also required to display low microwave losses self resonances well above the operating frequencies of the device, and small nonlinearities [Man12; Mas+12; Bel+12].

Reaching an impedance above R_Q can be challenging with standard geometric inductance. Increasing the length of a straight wire will come with an increase of self-capacitance. Without considering the effect of the kinetic inductance of a film, the maximum impedance that one can achieve is bound by the vacuum impedance $Z_0 = \sqrt{\mu_0/\epsilon_0} \ll R_Q$, with μ_0 and ϵ_0 the vacuum permeability and permitivity, respectively [Man12]. Instead, by considering more complex geometries, the design of the inductor can benefit from the mutual inductance. In

particular, it has been shown that one can reach $Z > R_Q$ by winding the wire in a spiral shape [Per+20].

The space available to pattern the inductor in some qubit applications is limited, and geometric superinductors may be challenging to implement besides having a higher sensitivity to flux noise due to their length. Therefore, one has to resort to alternative methods to build superinductors. In the following subsections, we briefly discuss two approaches to realize superinductors: arrays of Josephson junctions and disordered superconductors. The former one relies on the large inductance provided by Josephson junctions, while the latter exploits the concept of kinetic inductance.

1.3.1 Josephson junction arrays

Usual Josephson tunnel junctions are built from two superconductors separated by an insulating layer. Given the ease in obtaining and manipulating Al, $Al/AlO_x/Al$ Josephson junctions have become the most widespread materials stack in the superconducting quantum circuit community. The properties of the junction, namely the critical current I_c, can be easily tuned by changing the area or the thickness of the insulating oxide layer. This versatility together with the possibility of achieving inductances of the order of few a nH, while keeping them in a near linear response regime, make Josephson junctions an obvious approach to realize superinductors.

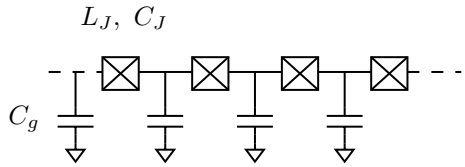

Figure 1.5: Schematics of an array of Josephson junctions. C_J and L_J are the capacitance and inductance associated to a single Josephson junction. C_g indicates the island's capacitance to ground.

By preparing Josephson junction chains with carefully designed junction areas and currents, one can engineer a medium with a large impedance and large inductance $L \simeq NL_J$, where N is the number of Josephson junctions in the chain [Man12]. However, arrays of junctions also introduce a set of inconveniences. First, the system needs to operate in a linear regime, this implies using significantly long chains of junctions with large critical currents to achieve the desired inductance. Also, Josephson junctions have an associated junction capacitance, C_J, and each island has a capacitance to ground, C_g (see Fig. 1.5 for a schematic of an array of junctions). The capacitance and inductance of a junction define

the so-called plasma frequency $\omega_p = 1/\sqrt{L_J C_J}$ which typically takes values in the $\omega_p/2\pi \sim 10 - 40\,\text{GHz}$. The plasma frequency lies above the operating frequencies of superconducting qubit devices, but since the array of junctions has a finite length, it will also have some associated modes with frequencies below ω_p. The frequency of these modes can be pushed towards ω_p by designing a small ratio of C_g/C_J. Overall, designing an array of Josephson junctions operating in a linear regime and suited as a superinductor requires a careful design of C_J, L_J and C_g to avoid parasitic modes and stray nonlinearities [Grü19]. Still, junction arrays achieve the best performance when making qubits so far [Ngu+19; Som+23; Wan+25].

1.3.2 Disordered and granular superconductors

An alternative to Josephson junction arrays are superconducting materials which naturally display large kinetic inductance. In the following subsections, we describe the concept of kinetic inductance and give an overview on disordered and granular superconductors.

Kinetic inductance

To understand the concept of kinetic inductance, we need to introduce three characteristic lengths: the superconducting penetration depth λ, the coherence length ξ and the mean free path l_e. λ represents the distance that a magnetic field penetrates into the superconductor, ξ gives the average distance of electrons forming a Cooper pair and l_e is the average distance traveled by an electron inside the material before a scattering event [Lóp+25; Tin04].

The kinetic inductance of a superconductor is related to the inertia of Cooper pairs and it is defined in terms of the penetration depth [Rot+16],

$$L_k = L_{k,\square} N = \mu_0 \lambda N \tag{1.10}$$

where μ_0 is the magnetic vacuum permeability and N the number of squares of a wire of length l and width w. For thin films where the thickness is much smaller than the penetration depth ($t \ll \lambda$), an external perpendicular magnetic field fully penetrates the sample and a correction to the kinetic inductance has to be considered [Kau78; Lóp+25],

$$L_k \equiv \mu_0 \lambda_{\text{thin}} = \mu_0 \frac{\lambda^2}{t}. \tag{1.11}$$

In disordered and granular superconductors, the impurities modify l_e and,

consequently, ξ [Pip+53]

$$\frac{1}{\xi} = \frac{1}{\xi_0} + \frac{1}{l_e}, \tag{1.12}$$

where ξ_0 is the coherence length of the pure material in the bulk. In the dirty limit ($l_e \ll \xi_0$), the BCS expression for the penetration depth [Tin04] can be approximated by

$$\lambda^2 \simeq \lambda_L(0)^2 \frac{\xi_0}{l_e}, \tag{1.13}$$

where $\lambda_L(0)$ is the London penetration depth in the clean limit at $T = 0\,\mathrm{K}$. Introducing the latter result in Eq. (1.11), and using the BCS definition of $\xi_0 = \hbar v_F/(\pi\Delta(0))$ with v_F the Fermi velocity and $\Delta(0)$ the superconductor gap at $T = 0\,\mathrm{K}$, we obtain an approximation for the kinetic inductance

$$L_\mathrm{k} = \frac{\hbar R_n}{\pi\Delta(0)} = \frac{\hbar R_n}{1.75\pi T_c k_B}, \tag{1.14}$$

where we have employed the concept of normal-state conductivity $\sigma_n = \rho_n^{-1} = (R_n\sigma/l)^{-1}$ [Gle+20]. Equation (1.14) already suggests that a large kinetic inductance will be related to large normal state resistance.

Disordered and granular superconductors

Disordered and granular superconductors generally display large kinetic inductance and their use as a superinductor is widely spread in the superconducting quantum circuit community. Although granular superconductors can be considered disordered from a morphological point of view, the inhomogeneities in these materials are well above the atomic level. These superconductors contain clusters of superconducting metal several nm in size surrounded by a matrix of an insulator or a normal metal. In contrast, in disordered superconductors the disorder is generally considered on the atomic scale [Gan+10; Gle+20].

The most widely used granular superconductor in superconducting qubit circuits is granular Aluminum (grAl). GrAl films are fabricated by evaporating Al in an O_2 atmosphere, the resulting material consisting of Al grains embedded in a matrix of AlO_x. The Al grain size and the AlO_x insulating barriers shape the properties of the material which can differ significantly from Al. In grAl, the resistivity of the film is given by the inter-grain coupling and can be tuned by changing metal deposition parameters such as the evaporation rate, the O_2 concentration or the substrate temperature. One of the well-known properties of grAl is its enhanced critical temperature first reported in the 60s by *Abeles et al.* [Abe+66]. The critical temperature of grAl can be as high as a factor three of the critical temperature of bulk Al. Nowadays, fabrication techniques under cooled

substrates have achieved grAl samples with grain sizes $\sim 2\,\mathrm{nm}$ and critical temperatures above $3\,\mathrm{K}$ [Deu+73a; Des+25]. Yet, probably one of the most striking properties of grAl is its phase diagram, where T_c can be modified with O_2 doping and displays a dome-shape distribution as a function of room-temperature resistivity [Deu+73b; Deu+73a].

On the other hand, materials such as NbN, TiN, or NbTiN are often regarded as highly disordered films with disorder at the atomic scale. The disorder in these type of superconductors can be controlled by changing deposition parameters such as the stoichiometry. The increasing disorder is translated in an increase of normal state resistivity. In contrast to grAl, the critical temperature in atomically disordered superconductors does not display a dome shape. Instead, it decreases with increasing resistivity and disorder until superconductivity is quenched [Gle+20]. In fact, the superconductor-to-insulator transition (SIT) in highly disordered superconductors is generally of an Anderson type (growing disorder in a system of non-interacting electrons). In contrast, for grAl the SIT is of Mott-type, which considers a decreasing electron concentration in the presence of Coulomb electron interactions [Gan+10; Bac+15].

Table 1.1 summarizes $L_{\mathrm{k},\,\square}$ for different superconducting materials measured in the context of superconducting quantum circuits. In general, grAl films have a wider range of L_{k} tunability than other nitride-based superconductors.

Table 1.1: Summary of kinetic inductance per square ($L_{k,\square}$) in different disordered and granular superconductors measured in the context of superconducting quantum circuits.

Material	Reference	$L_{\mathrm{k},\,\square}$ (nH /□)	Structure	Type
grAl	[Grü+18]	2.0	Stripline resonator	Granular
	[Gup+25]	0.05 - 0.32	Resonator	Granular
	[Zha+19]	1.2 - 2.0	Resonator	Granular
	[Grü+19]	0.1	Fluxonium	Granular
NbN_x	[Nie+19]	0.082	Nanowire	Disordered
	[Fra+23]	0.035 - 0.173	Resonator	Disordered
NbTiN	[Sam+16]	0.035 - 0.075	Nanowire resonator	Disordered
	[Bre+22]	0.23-0.40	Transmission line resonator	Disordered
TiN	[Ami+22]	0.001 - 0.239	Resonator	Disordered
	[She+18]	0.001 - 0.234	Thin film / Resonator	Disordered
NitrAl	[Tor+24]	0.001 - 0.422	Thin film	To be studied
	[Lee+24]	0.001 - 0.350	Thin film	To be studied

1.3.3 Superinductors for superconducting quantum circuit applications

In the following, we provide a brief overview of some of the most common uses of superinductors.

Superinductors have been extensively used in the superconducting qubit community. In terms of qubit applications, the fluxonium has probably benefited the most from them. Fluxonium qubits require loop inductances of the order of tens or hundreds of nH. The first experimental demonstration used an array of Josephson junctions [Man+09], however, nowadays it is common to see implementations of fluxoniums with grAl [Grü+19; Rie+23] and other nitride-based disordered superconductors [Haz+19]. Although there are proposals that use superinductors in other types of qubits such as transmons [Win+20], rf-SQUIDs [Pel+18], or other flux qubit types [Gei+24], the applications of these materials go beyond the qubit itself. Resonators fabricated in materials displaying low losses, high critical temperatures, and high resilience to magnetic fields are of key importance for quantum computing and quantum information processing applications. Some disordered nitride-based superconductors like NbTiN and TiN fulfill these requirements, especially when they are far from the SIT [Mül+22; Vis+10; She+18].

Sensing applications have long benefited from high kinetic inductance materials. It is the case for example of kinetic inductance detectors. These systems are based on the change in the imaginary part of the impedance in a resonator produced by the absorption of radiation and the subsequent generation of quasiparticle excitations. Materials such as TiN or NbTiN have traditionally been used to build these type of detectors [Bas12] but there are also proposals with grAl and other superinductors [Val+19].

Superinductors have also enabled novel quantum optics studies in circuit QED. Using Josephson junction chains, one can build high impedance environments. This approach recently allowed the detection of multi-mode fluorescence in a small Josephson junction embedded in a SQUID transmission line [Fra+25; Fra23].

Finally, superinductors can lead to new possibilities to study ultrastrong light-matter couplings. As we will see in Chs. 3 and 4, superinductors can be used to implement flux qubit-resonator couplings well into the non-perturbative USC regime. One of the advantages of this approach is that qubit persistent currents can be kept relatively low, implying larger coherence times, while having access to large shared inductances, and thus, large couplings.

1.4 Thesis overview

The main focus of this thesis is the study of ultrastrong flux qubit-resonator couplings enabled by superinductor materials. We provide two novel studies that define the structure of the thesis: the experimental implementation of a flux qubit galvanically coupled to an LC resonator in the USC regime using grAl as a coupler; and the study of the superconducting properties of Nitridized Aluminum thin films as a potentially new superinductor.

Before entering into the details of the studies mentioned above, we devote a substantial part of Ch. 2 to present the recipes for superconducting qubit fabrication. This thesis is the first in the group to include fabrication in-house of qubits, and many of the procedures have been developed from the ground up. We describe in detail the calibration of Josephson junctions and grAl fabrication. Additionally, we provide the multi-step qubit fabrication procedure developed to include grAl as part of the qubit loop. We conclude the chapter with an overview of the setup and the basic qubit measurement techniques used in Ch. 4.

Chapter 3 is the first devoted to the study of a flux qubit galvanically coupled to a resonator in the USC regime. The chapter presents the basic theory, circuits and Hamiltonians used in Ch. 4 to design the qubit-resontator system. We start from the basic elements: the 3-Josephson junction flux qubit with a non-negligible inductance and build up to the complete flux qubit-resonator system. Along with the different Hamiltonian derivations, we provide the expressions of the coupling coefficient in terms of the circuit elements and different numerical approaches to simulate the qubit-resonator system.

Chapter 4 uses the theoretical tools derived in Ch. 3 to design, implement and measure a flux qubit-resonator system in the USC regime. The design has two main particularities: it uses grAl as a flux qubit-resonator coupler, and it contains two feedlines to probe the qubit and the resonator independently. Besides the previous elements, important efforts are set towards the design of a coherent system in the USC regime. This chapter also includes the first implementation and measurements of a flux qubit coupled galvanically by a superinductor to an LC resonator in the USC regime. We show that even with the low persistent current of the qubit, the coupling is able to reach $g/\omega_r \simeq 0.13$. We conclude the work in superinductor-based USC studies with an outlook on future devices and measurements.

Finally, in Ch. 5 we study the superconducting properties of Nitridized Aluminum (NitrAl) thin films, a novel superinductor material developed in IFAE. This part of the thesis provides an extensive characterization of the critical temperatures, temperature-resistance behavior and critical magnetic fields for a set of 100 nm NitrAl films sputtered in different N_2 flows. We observe enhanced critical temperatures compared to those of Al and a similar dome-shape distribution

of T_c as a function of resistivity compared to grAl. We conclude the chapter with a first set of resonators patterned in this novel superconductor with insights on future studies involving NitrAl films.

The last chapter of the thesis, Ch. 6, reviews the main conclusions of the different studies and provides an outlook into future experiments.

Chapter 2

Experimental methods

Contents

In this chapter, we describe the different fabrication methods used in this thesis to produce flux qubit devices, as well as the different room-temperature and low-temperature setups used to carry out the measurements described in the rest of this thesis. Especial attention is given to the fabrication of granular Aluminum (grAl) and the multi-layer flux qubit fabrication recipe developed for the devices presented in Ch. 4.

2.1 Micro and nanofabrication

The devices presented in this thesis are fabricated in different cleanroom facilities available in Barcelona. The optical lithography is performed at the Institute of Photonic Sciences (ICFO) and the Centro Nacional de Microelectrónica (CNM), the electron beam lithography (EBL) is carried out at CNM and the Catalan Institute of Nanoscience and Nanotechnology (ICN2), and, finally, the evaporations and lift-offs are performed at the Institute of High Energy Physics (IFAE) cleanroom.

The fabrication of qubit devices presented in Ch. 4, and depicted in Fig. 2.1, involves a total of five fabrication steps:

1. Alignment markers

2. Resonators and ground planes
3. Granular Aluminum
4. Josephson junctions
5. Contacts between different layers

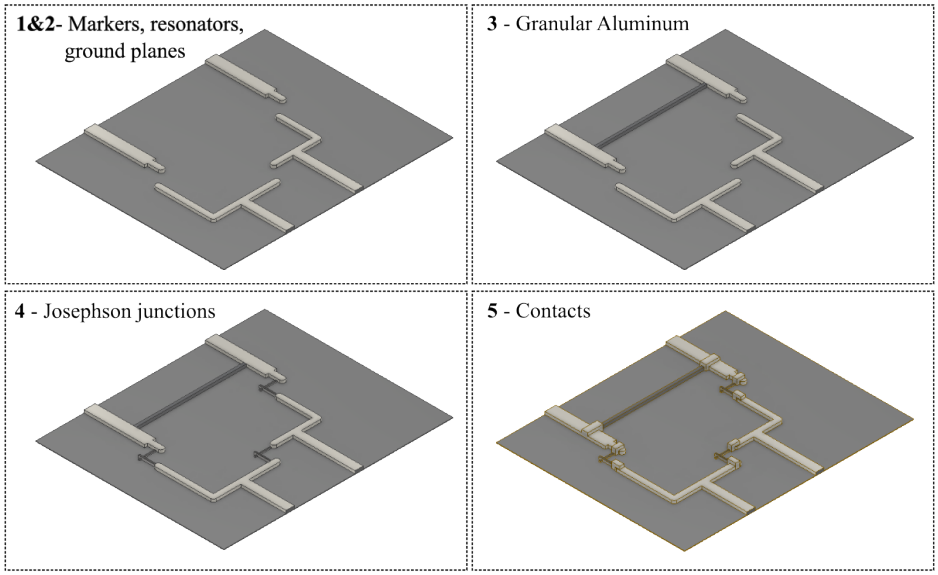

Figure 2.1: Schematics of the qubit loop showing the different fabrication steps. The lighter gray areas represent the Al structures connecting to the resonator, while the darker structures in steps 3-5 show the grAl and Josephson junctions.

Most of the fabrication recipes presented in this chapter had to be developed during the course of this thesis. In the next sections, we present the recipe development for micro- and nanofabrication of superconducting qubit devices with special attention to Josephson junctions and grAl. The detailed fabrication of qubit devices used in this thesis is given in Appendix A.

2.1.1 Microfabrication techniques and recipes

We begin this chapter by the microfabrication. The superconducting qubit devices used throughout the thesis generally require, besides the qubit, large ground planes, feedlines and planar resonators. These structures have dimensions that

can reach up to hundreds of microns and they are suited for optical lithography. The pattern takes between seconds up to few minutes and the resolution can be as good as $\sim 1\,\mu$m depending on the instrument and resist used.

In the following sections, we will assume to start with a substrate which has been previously cleaned in acetone and isopropanol. If the previous fabrication step required the use of resists, we include a plasma descumming step into the cleaning. The full set of fabrication can be found in Appendix A.

Markers

Chips involving more than one fabrication step require alignment markers. Alignment markers are structures designed at the micron scale that help align the different layers of the fabrication process with respect to each other. The choice of shape and material depends mostly on the type of lithography and instruments used throughout the process. In our case, we have access to a Karl SUSS microtech mask aligner, a Heidelberg maskless aligner, and two different 30 kV Raith EBL systems.

Generally, one needs markers of several hundreds of microns in length and tens of microns in width to operate the mask aligner on a chip that already contains a pattern. The requirements are more flexible in the case of the maskless aligner. Squares of few microns in width placed at the corners of the chip are enough to perform a good alignment. Finally, the different Raith EBL units need local markers at the different locations where we want to pattern structures, i.e., they need to fit inside an EBL write-field. The different requirements from each instrument must be taken into account at the time of designing a mask with markers.

The alignment accuracy is different for each system and can be affected by the real dimensions of the markers and the presence of a small vertical tilt in the sample. In general, the Raith EBL units can align with accuracies of few nm while for the optical lithography systems the deviations are in the range 100 nm − 500 nm. Qubit designs should be flexible enough to accommodate misalignments between layers.

Markers are fabricated on a $4''$ wafer-scale using a Karl Suss mask aligner and a stack of LOR3A+HPIR6512 positive photoresist (see Sec. A.2.1 for the detailed recipe). Fig. 2.2 shows a mask design together with different zoom-in images from chips, devices and markers present on the mask. Each device contains "L"-shaped markers accompanied by a circular shape to perform alignment in optical lithography processes. The smaller blocks of four "L"-shaped markers are intended for EBL. The spacing between markers is 90 µm to fit inside a 100 µm write-field. Several device copies also contain blocks of four "L"-shaped markers spaced 190 µm in case bigger write-fields are used.

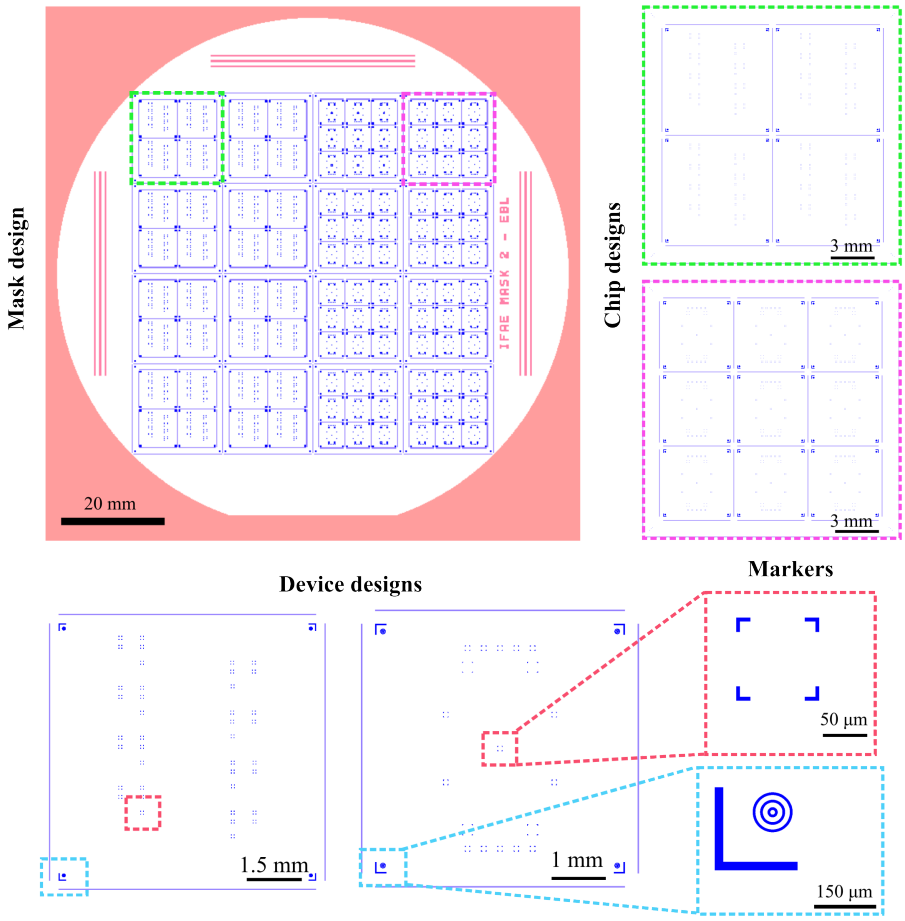

Figure 2.2: Mask design for Pd markers. The mask design contains an array of 16 chips of 2 cm × 2 cm with two different device designs. The device depicted on the left has dimensions 7.5 mm × 7.5 mm and the one on the right is 5 mm × 5 mm. On each device we have mainly two types of markers, four concentric "L"-shaped EBL markers spaced 90 µm and a combination of "L"-shaped and circular markers for optical lithography.

We choose Pd as the material for our markers. The choice of Pd is motivated by the fact that it displays good contrast in the EBL systems and it is chemically compatible with Al. To ensure a good contact with the Si substrate, we first

evaporate a layer of 3 nm of Ti followed by 30 nm of Pd. We use a standard lift-off process consisting in N-methyl-2-pyrrolidone (NMP) at 75 °C for approximately 2 h. Once the residual metal has come off, we clean the wafer in isopropanol and we blow-dry the surface with N_2 gas.

Ground plane, resonators and feedlines

The process followed to fabricate resonators, ground planes and feedlines is similar to the one used for markers. The choice of resist type and instrument will depend on the design and metal deposition technique. Generally, for metal evaporation and designs which are densely metalized, we use a negative photoresists. This is the case of the devices presented in Ch. 4. For designs where only small portions of the device need to be metalized it will be more appropriate to use positive photoresists, which is the case for markers and DC test structures such as the ones presented in Section 2.1.2. In general, we can achieve better resolution with the maskless aligner, reaching down to 1 µm. The detailed photolithography recipes are described in Section A.2.

2.1.2 Granular aluminum fabrication

GrAl can be obtained by evaporating Al in an oxygen atmosphere. Depending on the partial pressure of oxygen and the evaporation rate, the resulting material will display different resistivity, critical temperature, and grain size [Grü19; Lev+19; Bac+14]. The advantage of grAl over other disordered or granular superconductors is the relatively simple fabrication process and compatibility with Al-based Josephson junction fabrication. However, a drawback of grAl is the lack of reproducibility. Small changes in the evaporation rate, in the oxidation, or even the oxygen contamination of the Al source, can affect the properties of the material [Rot+16; Jan+25].

At IFAE, we use an Al-dedicated Plassys electron beam evaporator. This evaporation system has two separate chambers that hold vacuum independently. The top one (load-lock) is smaller and is used to load samples, perform Argon milling, and O_2 microwave plasma descumming. The pressures in this chamber are typically in the 1×10^{-7} mbar range. The bottom chamber (process chamber) contains the different metal targets and holds the lowest pressures ($\sim 2.5 \times 10^{-8}$ mbar). The evaporator has the possibility of incorporating high purity Ar, N_r and O_2 through different valves and mass flow controllers connected to the load-lock. In this section, we will focus on the incorporation of O_2 during metal deposition.

The grAl fabrication process used in this thesis is similar to the one reported previously in the literature [Gei+24; Grü19] and follows these steps:

- Pump down the load-lock chamber for approximately 2.5 h, or until the pressure is around 2.6×10^{-7} mbar. The pressure in the process chamber should lie below 5×10^{-8} mbar.
- Perform and initial Ti evaporation to decrease further the background pressure. During the Ti evaporation, the substrate shutter is closed and the substrate holder is kept in the loading position.
- Select the Al crucible dedicated to grAl depositions and rotate the sample to the evaporation position. Insert an oxygen flow and slowly increase the current on the target to obtain the desired deposition rate. Once it is stable, open the shutter and evaporate the desired grAl thickness.
- Close the substrate shutter, stop the oxygen flow and ramp down the current on the Al target.
- Unload the metalized sample.

Although the granular Al evaporation process is relatively straightforward, there are limitations set by the components that need to be known before starting the recipe calibration. The first limitation is the maximum allowed pressure during evaporation. The value is set by the electron beam gun, which cannot stand pressures above 10^{-5} mbar during operation. In this sense, it is advisable to have a mass flow controller with 0.1 sccm precision or below. Mass flow controllers with higher ranges (e.g. 100 sccm) and precision on the 1 sccm can also be used when they are combined with deposition rates on the order of ~ 1 nm/s [Gei+24; Ihs+25]. An alternative to obtain a wider range of resistivities while keeping a relatively low evaporation rate with a 100 sccm mass flow controller is to introduce argon to reduce the partial pressure of oxygen in the chamber. Still, the system will be limited by the maximum allowed pressure during deposition. The second limitation is related to the maximum current allowed in the crucible pocket which will set a limit to the evaporation rate.

For our grAl calibration we use an evaporation rate of 0.2 nm/s and oxygen flows up to 0.8 sccm. A rate of 0.2 nm/s requires currents in the range 60 mA − 320 mA, depending on whether a liner is used in the crucible pocket or not. On the other hand, when a liner is not used, relatively low deposition rates (0.1-0.2 nm/s) appear to be more stable. The maximum flow is set by the pressure in the process chamber. For a standard grAl deposition in our Plasssys with 0.2 nm/s and 0.8 sccm, the pressure in the process chamber during deposition reaches around 2×10^{-6} mbar[1].

[1]The pressure during evaporation is actually lower than the pressure during the current ramp. During this process and with 0.8 sccm, we can reach up to 5×10^{-5} mbar which is close to the system's limit

Granular Aluminum characterization

Three DC test structures are used to characterize grAl (see right panel in Fig. 2.3). They are designed with a different number of squares and geometries to adapt to samples with a wide range of resistivity values. Additionally, the top two structures in Fig. 2.3 are convenient to perform temperature-dependent resistance measurements. They both have four relatively big pads which are suitable for wire-bonding in 4-probe configuration. In order to pattern different DC test structures, we use the optical lithography process described in Section 2.1.1. Devices are deposited on an intrinsic Si substrate previously cleaned with acetone and isopropanol.

We perform a set of grAl evaporations at different O_2 flows and measure the resulting structures with a 4-probe resistance measurement right after fabrication and after performing a thermal annealing of 13 min at 200 °C. In our qubit devices, grAl is the first EBL layer. During the Josephson junction and contact fabrication the sample undergoes a set of bakes with temperatures ranging from 150 °C to 190 °C and a total duration of approximately 13 min. The bake used in the calibration process is used to estimate the change of resistance due to the multi-layer fabrication process [Rot+16]. Figure 2.3 shows one of the grAl calibration curves for 50 nm-thick samples right after fabrication and after performing a 13 min at 200 °C bake. The sheet resistance increases non-monotonically with the addition of O_2 in the chamber. Annealing the sample reduces the resistance of the film by a $10 - 20\%$. Finally, note that those samples evaporated at 0.8 sccm are significantly less reproducible. This lack of reproducibility is due to difficulties to stabilize the rate at higher O_2 flows.

In this thesis, grAl will be used as a superinductor material to achieve large inductances in reduced volumes (see Ch. 3 and 4). Thus, to complete the calibration, it is important to obtain an estimate of the sheet kinetic inductance ($L_{\mathrm{k},\square}$) of the films as a function of other parameters. Using the Mattis-Bardeen formula for complex conductivity in the local, dirty limit at low frequency ($hf \ll k_B T$) and in the low temperature limit ($T \ll T_c$) we can obtain an estimate for $L_{\mathrm{k},\square}$ [Rot+16],

$$L_{\mathrm{k},\square} = 0.18 \frac{\hbar R_{4\mathrm{K},\square}}{k_{\mathrm{B}} T_{\mathrm{c}}}, \tag{2.1}$$

where T_{c} is the critical temperature, $R_{4\mathrm{K},\square}$ is the normal state sheet resistance measured at 4K and k_{B} is the Boltzmann constant.

The interesting $R_\square$ range in Fig. 2.3 comprises samples evaporated with 0.6 sccm. These samples display a small dispersion of resistance values and their resistance is an order of magnitude larger than Al ($R^{\mathrm{Before}}_{\square,\mathrm{Al}} = (0.89 \pm 0.06)\,\Omega/\square$). In Fig. 2.4, we present an example of a temperature-resistance curve for grAl prepared with 0.6 sccm (the details of these $R(T)$ measurements are presented in

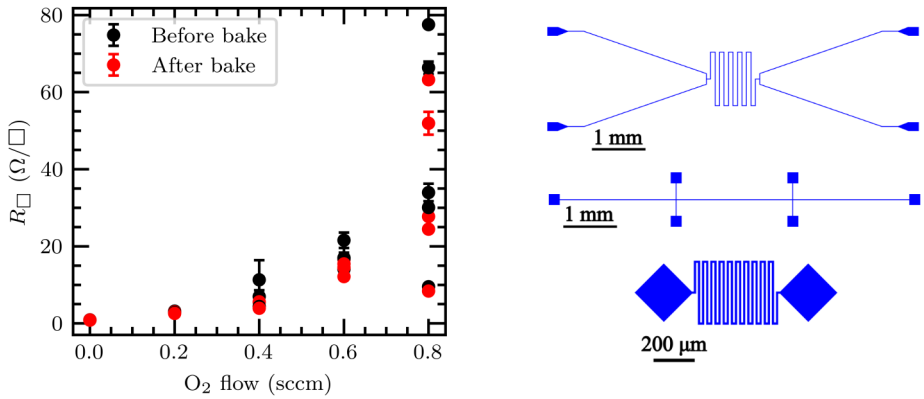

Figure 2.3: GrAl calibration for 50 nm thick samples evaporated at different O_2 flows. The black circles indicate the sheet resistance right after fabrication and the red ones show the sheet resistance after a bake of 13 min at 200 °C. The error bars indicate the spread of values between the different test structures present on each chip. The image on the right, shows different test structures used for the resistance measurements.

Ch. 5). The critical temperature for 0.6 sccm range is estimated around 2 K and the sheet resistance at 4 K is a factor 1.1 smaller than the room temperature sheet resistance $R_{\square,\mathrm{RT}}$. With this information and using Eq. (2.1), we can estimate the sheet kinetic inductance to be around $L_{k,\square} \sim 10\,\mathrm{pH}/\square$.

2.1.3 Qubit and junction fabrication

In this section, we will focus on qubit and Josephson junction fabrication based on electron beam lithography (EBL).

At the IFAE QCT group, we have developed a multi-step qubit fabrication recipe consisting on three steps for the devices presented in Ch. 4 and two steps for standard flux qubit designs. The qubit fabrication consists of grAl deposition, Josephson junction fabrication and contact layer deposition. Dividing the fabrication in multiple steps leads to flexible design geometries and clean contacts between Josephson junctions and other structures already present on the device. Particularly for the devices presented in Ch. 4, our multi-step fabrication allows for adjusting the design parameters after every step of fabrication to make sure the qubit-resonator system is in the USC regime. However, the versatility in our fabrication process comes at the expense of number of lithography, evaporation and cleaning steps. This is in contrast to the three-angle deposition method used

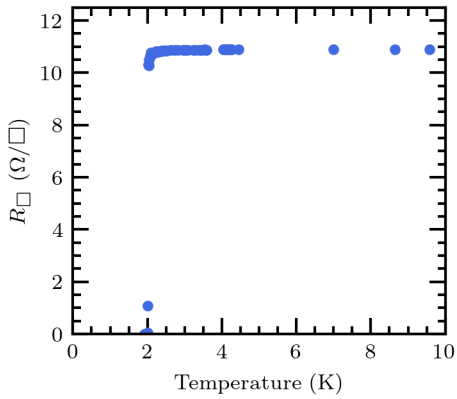

Figure 2.4: Example of T_c for a 50 nm grAl sample with $R_{\square,\mathrm{RT}} = 11.90\,\Omega/\square$ evaporated at 0.2 nm/s and 0.6 sccm of O_2 flow. The estimated critical temperature is $T_c = 2.01 \pm 0.01$ K.

in grAl-based fluxonium qubits where Josephson junctions and grAl are patterned in one EBL step and evaporated consecutively without breaking the evaporator vacuum [Grü+19; Grü19].

The workflow of our qubit fabrication can be summarized as follows:

1. EBL of grAl structures. Before deposition, we clean resist residues using an in-situ O_2 plasma descumming process. Afterwards, grAl is evaporated vertically and subsequently lifted-off.

2. Josephson junctions patterning with EBL. We clean resist residues using an in-situ O_2 plasma descumming step. Keeping the device in vacuum, the junctions are shadow-evaporated with an intermediate static oxidation step. The junctions are lifted-off right after evaporation.

3. Patterning of the contacts by EBL and cleaning of the resist residues using an O_2 microwave plasma ashing. We then perform an Argon ion milling step to ensure a clean and superconducting contact between the different layers of the chip. Finally, the contacts are evaporated in a vertical deposition.

It is essential to have a proper calibration and control of all the steps listed. In the following, we provide a detail of the fabrication process and characterization of Josephson junctions as well as the different intermediate cleaning steps.

Oxygen plasma and Argon ion milling

A proper substrate and metal layer cleaning is key to obtain reproducible devices. Resists such as PMGI SF7 are known to leave a substantial amount of residues, while chemicals like MP-351 (PMGI developer) are not sufficient to remove them. Plasma descumming is a technique used to remove organic residues. The effect of the descumming is to reduce the aging of Josephson junctions and to increase their reproducibility [Pop+12; Kop+07]. We have the capability of performing microwave oxygen plasma descumming in-situ prior to deposition inside the Plassys evaporator. Alternatively, we can use a dedicated TePlA GIGABatch 360M plasma asher machine at the CNM cleanroom. We characterized the descumming effect for both systems and for the different resists used for Josephson junction fabrication. We spin coat samples with CSAR62 and PMGI SF7 independently and dice them into several pieces. The thickness of the resist is measured after each plasma ashing recipe to find the optimal ashing rate.

For the TePlA system we use a recipe with 200 W of power and 50 sccm of O_2 flow. In Fig. 2.5 (a), we show the resulting ashed thickness as a function of time for both PMGI and CSAR. A simple linear fit to the data gives an estimated ashing rate of 40.2 nm/min for PMGI and of 25.4 nm/min CSAR. With ~ 30 s of recipe time should be sufficient to remove resist residues from the surface. The same process is repeated for the plasma descummming available at the Plassys evaporator. In this case, we use a recipe with 50 W of microwave power, 10 sccm of oxygen flow and a source frequency of 2400 MHz. The resulting etched resist thickness is shown in Fig. 2.5 (b). A linear fit to the data provides ashing rates for PMGI of 17.8 nm/min and 16.3 nm/min for CSAR. Similarly to the previous case, ~ 1 min should be enough to clean resist residues.

An additional key cleaning procedure we used in the junction fabrication procedure is the Argon ion milling. This process is usually employed to remove oxides from existing metal layers [Grü+17]. We use Argon ion milling before depositing the contact layer between the Josephson junctions and other metalized areas of the chip. The Plassys evaporator is equipped with a Kaufman ion source allowing us to run the 4 min ion argon milling process in-situ prior to metal deposition. The parameters of the ion source during cleaning are:

- 6 sccm Ar gas flow
- 400 V beam voltage
- 22 mA ion beam current
- 80 V ion beam acceleration voltage
- 40 V EBG discharge voltage

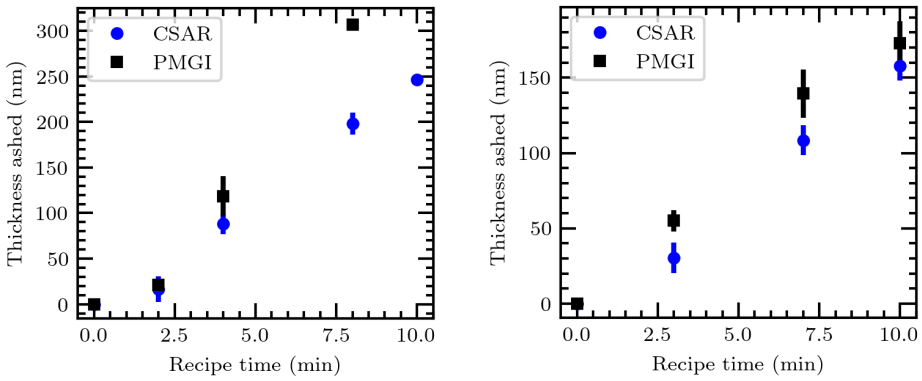

Figure 2.5: CSAR62 and PMGI SF7 resists thickness removed as a function of the descumming recipe time. (a) TePlA system with 200 W of power and 50 sccm of O_2 flow. (b) Plassys with 50 W of microwave power, 10 sccm of O_2 flow and frequency 2400 MHz.

Josephson Junction fabrication

At the IFAE QCT group we developed a recipe for the well-known Manhattan-style Josephson junctions [Pot+01]. We opted for a double-stack resist consisting of a bottom layer of PMGI SF7 of thickness 630 nm and a top layer of CSAR62 of thickness 240 nm. CSAR62 defines the dimensions of the junction leads and areas, while PMGI SF7 gives the necessary undercut for the shadow angle evaporation. The advantage of PMGI SF7 over other resists used for EBL lithography is that no ghost dose is needed to obtain a large enough undercut. The undercut in PMGI depends on the developer used, the development time and the pre-bake.

We pattern the Josephson junctions on a 30 kV Raith EBL system using 20 kV and a 20 µm aperture with a dose of 180 µC cm^{-2}. The samples are developed in two steps, first with a CSAR developer (AR 600-546) and, secondly, the PMGI developer (a solution of 1:3.5 MP − 351 : H_2O). The detailed development process is given in Section A.4. As detailed in the previous section, prior to deposition, the sample undergoes an oxygen plasma descumming to remove organic residues on the substrate, mostly from PMGI.

The Josephson junction deposition is performed in an Al-dedicated Plassys evaporator following the steps:

- Pump the samples down overnight ensuring a load-lock pressure below 1.7×10^{-7}mbar, and a process chamber pressure below 5×10^{-8}mbar.

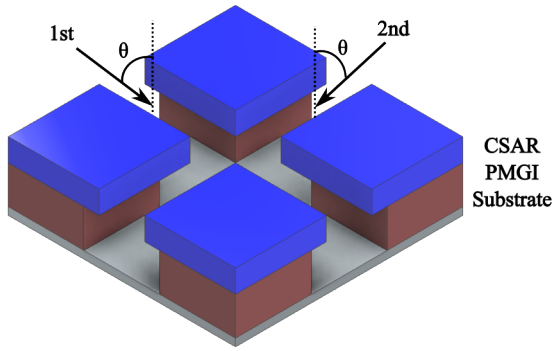

Figure 2.6: Schematics for the resist stack needed for Manhattan-style junctions. The blue layer simulates the CSAR62 resist and the dark brown represents the PMGI SF7. The different arrows indicate the two evaporation directions and θ represents the tilt angle.

- First evaporation at 55° tilt angle of 36 nm of Al at 0.3 nm/s rate.
- Static oxidation at 0.5 mbar.
- Second Al evaporation of 69 nm at 0.3 nm/s rate performed rotating 90° in the planetary direction and tilting the substrate 55°.
- Final oxidation step of 5 min at 0.5 mbar to passivate the electrodes and reduce ageing [Bil+21].

The Manhattan-style Josephson junction deposition is depicted in Fig. 2.6. The effective thickness in each evaporation step results in $\sim$ 20 nm and $\sim$ 40 nm, respectively. The effective thickness is calculated using $t_{\text{set}} \cos\theta$, where t_{set} is the thickness at the evaporator and θ the angle of evaporation. The latter expression can be obtained considering that the target thickness is measured in the vertical direction while the substrate during JJ deposition is tilted an angle θ (see for example Fig. 2.7).

Once the sample has been successfully evaporated, we perform the liftoff in a solution of N-methyl-2-pyrrolidone (NMP) at 75 °C with a stirring magnet set to a rotation of 150 rpm for 2 h. We finish the lift-off process by rinsing the sample in IPA and drying it with N_2. Our fume-hood is covered with an antistatic cage and equipped with an ion fan to avoid electrostatic discharges on samples.

Josephson junction areas and evaporation angle

The maximum and minimum Josephson junction areas are limited by the evaporation angle and the resist height and undercut.

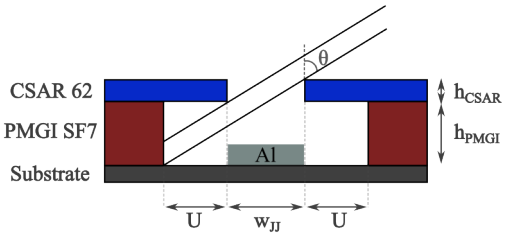

Figure 2.7: Schematics to determine the evaporation angle for Manhattan-style junction evaporation. θ is the angle of evaporation, w_{JJ} is the designed width of the Josephson junction, U is the undercut and h_{CSAR} and h_{PMGI} are the resist thicknesses of CSAR62 and PMGI SF7, respectively.

Using the schematics of Fig. 2.7, we can calculate the minimum angle needed to evaporate Manhattan-style junctions with our resist stack. Let us assume that the first Josephson junction layer has been deposited on the substrate (see the Al rectangle defined in the schematics). We want to obtain the minimum angle for which the Al from the second evaporation will be deposited on the resist wall. This condition will avoid a secondary lead of Al being deposited next to the one defining the Josephson junction. From a mathematical point of view this condition reads,

$$\tan\theta = \frac{w_{\mathrm{JJ}} + U}{h_{\mathrm{PMGI}} + h_{\mathrm{CSAR}}} \quad \Longrightarrow \quad \theta > \arctan\left(\frac{w_{\mathrm{JJ}} + U}{h_{\mathrm{PMGI}} + h_{\mathrm{CSAR}}}\right), \tag{2.2}$$

where h_{PMGI} and h_{CSAR} are, respectively, the thicknesses of the PMGI and CSAR resist layers, U is the undercut and w_{JJ} is the width of the first Josephson junction lead layer. Using a total resist thickness of $h_{\mathrm{PMGI}} + h_{\mathrm{CSAR}} = 870\,\mathrm{nm}$, the estimated undercut U which takes values between 500 nm and 700 nm and a maximum Josephson junction width of 300 nm, we obtain that the evaporation angle should be above $50°$ for $U = 700\,\mathrm{nm}$. The same idea can be used to calibrate the undercut of the resist, which can be determined by designing Josephson junctions of increasing width and evaporating them at a fixed angle. The maximum Josephson junction width will be given by the design that does not show a secondary lead. This width can be used in Eq. (2.2) to obtain an estimate of U.

The minimum Josephson junction width is mostly determined by the length of the Josephson junction lead, the possible angle loading error and the patterning

parameters. With the geometry described in this section and for 55° evaporation angles, we have been able to pattern 160 nm-wide Josephson junctions.

Josephson junction current density estimate

The fabrication process of Josephson junctions includes a static oxidation step at 0.5 mbar. The oxidation time determines the oxide barrier grown between Al leads and, thus, the properties of the Josephson junction [Mos+23]. In general, for flux qubit applications, we need Josephson current densities ranging between $2.0\,\mu\mathrm{A}/\mu\mathrm{m}^2$ and $3.0\,\mu\mathrm{A}/\mu\mathrm{m}^2$. We could also use dynamic oxidation for this range of current densities, but the dynamic oxidation pressures are limited to 0.05 mbar by the 10 sccm O_2 mass flow controller of our setup. Given the low pressures, the samples require between 30 to 40 min of dynamic oxidation to reach the desired target J_c. Instead, with static oxidation, we can reach similar values in a fraction of this time ($\sim 10\,\mathrm{min} - 15\,\mathrm{min}$). We use the structures depicted in Fig. 2.8 to calibrate the Josephson junction oxidation . The first three copies numbered 1-3 are used to calibrate the small Josephson junctions with areas given by αA with $0.5 < \alpha < 1$ (see Ch. 3 for more details on the selection of α). The remaining three copies are used to calibrate the big junctions of area A. The design also includes a vertical and a horizontal short to characterize the Al resistance in each of the two evaporation steps.

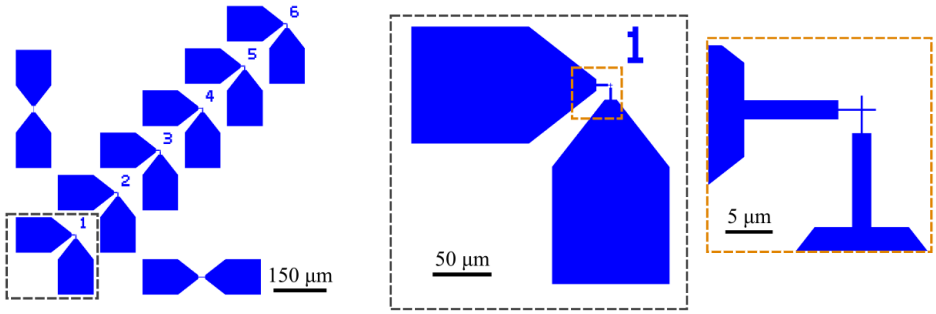

Figure 2.8: Design to test Josephson junction oxidation. Copies 1-3 are used to test the small junctions (αA), while copies 4-6 are used for the big junctions (A). The vertical and horizontal test structures visible in the left image are shorts to test the Al resistance in each evaporation.

Multiple Josephson junction oxidation pressure calibrations have been performed during the course of this thesis. In the following, we present the latest calibrations used for the fabrication of the device studied in Ch. 4.

One can estimate the Josephson junction critical current (I_c) through the Ambegaokar-Baratoff formula [Amb+63],

$$I_c R_n = \frac{\pi \Delta}{2|e|}, \tag{2.3}$$

where R_n is the junction normal state resistance, Δ is the gap of the superconductor and e is the electron charge. We can estimate the superconductor gap by using $\Delta \simeq \Delta_0 \simeq 1.764 k_B T_c$, where Δ_0 is the superconducting gap at zero temperature, and $T_c = 1.2\,\mathrm{K}$ is the critical temperature of Al. As a first approximation, and given the low RRR of our thin films, we use the room temperature resistance obtained by two-probe measurement (see Sec. 2.2 for a description of the setup) of the test junctions presented in Fig. 2.8. With this set of parameters, it is possible to estimate I_c. However, it is relevant to have access to the Josephson junction critical current density $J_c = I_c/A$, which requires an estimate of the junction area, A.

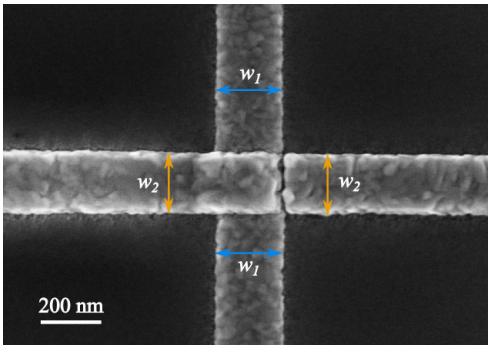

Figure 2.9: Example of a SEM image of a Josephson test junction. The blue and orange arrows indicate the regions used to determine the width of the different junction leads.

The resulting Josephson junction area can differ from the designed value and is strongly influenced by the quality of the EBL focus. In order to obtain a more accurate estimate of Jc, we acquire scanning electron microscope (SEM) images of the different test junctions. In Fig. 2.9, we show an example of a SEM image of a test junction. The blue and orange arrows indicate the regions used to determine the width of the different junction leads. Combining the measured widths (w_1, w_2) together with the nominal thickness of the bottom layer (t_1), we can determine the area of the Josephson junction,

$$A = w_1 w_2 + t_1 w_2. \tag{2.4}$$

Note that Eq. (2.4) considers the surface defined by the two crossing leads and the first edge contact connecting both layers. We neglect the contribution of the second edge contact since it is broken in a vast majority of devices (see the right junction contact in Fig 2.9). To achieve a complete contact from both sides of the Josephson junction a third evaporation angle of 55° tilt and −90° planetary rotation could be included in the deposition process.

Combining the resistance measurements at room temperature and the estimate of the Josephson junction area, we can finally calculate J_c. In Fig. 2.10, we show the resulting set of values obtained for test junctions fabricated with a static oxidation at 0.5 mbar and different oxidation times. Each point represents the averaged J_c for a test junction chip containing four copies of the structures presented in Fig. 2.8. Panel (a) shows J_c obtained for big Josephson junctions ($A \sim 0.078\,\mu m^2$) while panel (b) shows J_c values for small junctions ($A \sim 0.045\,\mu m^2$). We show less points for small Josephson junctions, given that they were breaking more easily due to a slight change in EBL dose factor calibration. We plot together Josephson junctions fabricated with (purple and gray) and

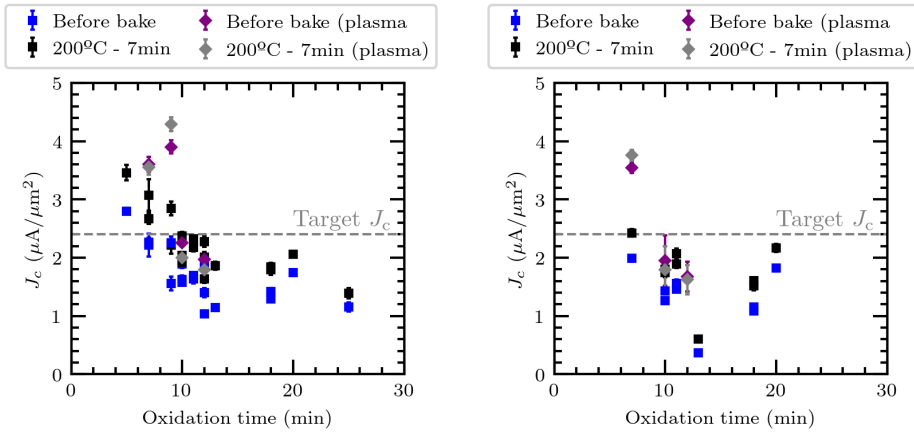

Figure 2.10: Estimated Josephson junction critical current density as a function of the oxidation time for a static oxidation pressure of 0.5 mbar. In blue/purple we show the data obtained right after fabrication, and in black/gray the J_c after a bake of 200 °C for 7 min. Samples corresponding to purple and gray markers underwent an O_2 plasma descum before deposition. The dashed gray line indicates the target $J_c = 2.4\,\mu A/\mu m^2$ value for the design studied in Ch. 4. (a) Estimated J_c for big Josephson junctions ($A \sim 0.078\,\mu m^2$) and (b) estimated J_c for small Josephson junctions ($A \sim 0.045\,\mu m^2$).

without (black and blue) an O_2 plasma descumming step. In general, Josephson junctions fabricated without an O_2 descumming show a higher change in resistance and J_c with a 200 °C bake of 7 min. This significant change in resistance can be linked to resist residues in the vicinity of the junction [Pop+12; Kop+07]. Besides the change in resistance observed after the bake, we also observe a significant spread of J_c values. We attribute the spread of J_c to problems in the rate stabilization during evaporation and changes in the process chamber pressure. Additionally, environmental conditions such as temperature and humidity are not always well controlled and may have an effect on Junction reproducibility.

The calibration of the Josephson junction current density could be improved further. From a fabrication point of view, it is clear that cleaning the substrate before deposition has an impact on the resistance and aging of junctions, thus O_2 descumming needs to be included in the fabrication process. On the other hand, creating a new curve each time the process chamber of the evaporator is opened or setting lower and consistent pressure thresholds before evaporation can help reduce the spread in each calibration curve. By better controlling other ambient elements such as temperature or humidity fluctuations in the cleanroom we can also reduce the spread in junction resistance. Similarly, the spread in area could be improved by introducing a cold development. This process ensures a reproducible temperature of the developer and it is known to yield consistent and reproducible areas [Mil22]. Finally, a possible way in which the Al grain size can be standardized by better stabilizing the evaporation rates. This can be achieved by a proper melting of the crucible metal and a proper allocation of the beam spot.

Fabrication of contacts

The last fabrication step in our qubit recipe consists of patterning and evaporating patches connecting the different metal layers. Previous works [Osm+21] have proposed a method to evaporate the contacts in-situ after junction deposition. However, this process requires thick resist stacks and the calibration of a three-angle shadow evaporation. We decided to follow the standard approach which consists of adding an extra EBL step. On the other hand, this is by far the most common procedure in the community [Dun+17].

In the patch fabrication step we change the resist stack. Instead of PMGI SF7 and CSAR 62, we use MMA EL6 for the bottom layer and PMMA 950 A4 for the top layer. The change of resist stack is motivated for two reasons. First, the increased resistance measured in test junction structures with patches fabricated in PMGI and CSAR. The bad contact is probably due to resist residues in the different metal surfaces left by PMGI. Secondly, the particular stack of MMA EL6 - PMMA 950 A4 used in this work can be patterned at 10 kV. Decreasing the voltage and dose near the Josephson junctions can decrease significantly the

impact on the final resistance due to stray back-scattered electrons [Bal+24].

The evaporation of the contacts requires two separate cleaning procedures. First, an oxygen plasma descumming to remove possible resist residues and, secondly, an Argon ion milling step prior to deposition to eliminate surface oxides. In order to avoid the contacts from breaking, we deposit a total Al thickness of at least 100 nm. This thickness is twice the value used for the optical layer and two to four times thicker than the different junction leads. We validate the quality of the contacts on the same device by measuring Josephson junctions fabricated with patches and comparing them with single-step junctions.

2.2 Experimental setup

In this section, we present the setup used for the experiments detailed in Ch. 4 and 5. We also provide some details on the room-temperature characterization setup used for the calibrations presented in Sec. 2.1.2 and 2.1.3.

2.2.1 Room temperature characterization setup

For room-temperature measurements we employ two-probe or four-probe techniques. In both, we use a manual probe station. For the 4-probe measurements of metal structures or thin films, we use a Keithley 2634B source meter. For Josephson junction characterization, we use 2-probe measurements. In this case, we use a digital Keithely multimeter connected to a home-built *Josephson junction measurement box*. The purpose of this box is to regulate the maximum current bias applied to the Josephson junction by fixing the voltage across the junction to 10 mV.

2.2.2 Qubit and DC measurement setup

The experimental setup used for the qubit measurements and thin film resistance measurements respectively presented in Ch. 4 and 5 is summarized in Fig. 2.11. The setup consists of a BlueFors SD cryogen-free dilution refrigerator equipped with three radio frequency (RF) lines and 24 DC lines. Input 1 is used to drive the sample with a microwave tone, input 2 has less attenuation and it is used to send flux pulses to the qubit control line and, finally, the output line is used to read the transmitted signal through the sample. Besides the difference in attenuation, the last stages of the output line are made of Ag-CuNi cables with Ag center line which decrease the signal loss at the cost of less thermal isolation. The DC lines are used to either drive a coil attached to the sample box, or to perform thin film resistance measurements. In the former case, the DC lines are made from phosphor-bronze until the 4 K stage. From 4 K down to the

mixing chamber, they are uninterrupted and made from CuNi-NbTi not to break superconductivity. For thin film resistance measurements, the DC lines are made entirely out of phosphor-bronze.

Background magnetic fields are screened by a combination of three shields:

- Flexible mu-metal lamina that covers all the surface outside the vacuum.
- A 2 mm-thick mu-metal shield inside the vacuum can expected to provide a 250 factor of attenuation over the Earth's magnetic field.
- A 2 mm-thick Pb shield is installed inside the still can.

The Pb shield provides screening against gamma ray radiation and takes advantage of the fact that Pb is a superconductor below 7.2 K, thus, magnetic fields are expelled by the Meissner effect. The combination of shields is expected to provide a total factor 2×10^5 of attenuation over the Earth's magnetic field.

For qubit experiments the sample is mounted and wire-bonded to a 6-port ceramic PCB and packaged inside a light-tight copper sample box. Below the PCB, a thin rectangular copper piece is used to improve the thermal contact between the sample box and the PCB. Finally, in qubit measurements we usually include a copper spacer to reduce the number of parasitic box-modes (see Fig. 2.13). The sample box is then mounted on the mixing chamber (MXC) stage, reaching ~ 20 mK. In Fig. 2.12 we show a picture of a qubit sample mounted in the dilution refrigerator. For temperature dependent resistance measurements of thin film superconductors, we use commercial non-magnetic chip carriers from Kyocera that can be mounted either on the still or the mixing chamber plate.

Qubit measurements

The qubit presented in Ch. 4 is characterized mainly by spectroscopy measurements use two types of instruments. First, an Agilent E5071B VNA Network Analyzer (300kHz - 8.5GHz) sends a continuous RF tone and reads the transmitted and/or reflected scattering signals. Generally, the signal is attenuated between the VNA output and the sample box by $\simeq 120$ dB to reach the single-photon level at the sample (~ -140 dBm). The second instrument used in spectroscopy measurements is the RF-source able to send tones at GHz frequencies. In our case, we use a Rohde & Schwarz SGS100A SGMA.

We use two types of qubit spectroscopy techniques widely spread in the superconducting qubit community: single-tone spectroscopy, and two-tone spectroscopy. These measurements consider a system of a qubit coupled to a readout resonator, similarly to the experiment presented in Ch. 4. In single-tone spectroscopy one measures the transmission of the RF VNA tone as the magnetic flux at the qubit is swept using a superconducting coil. By changing the current

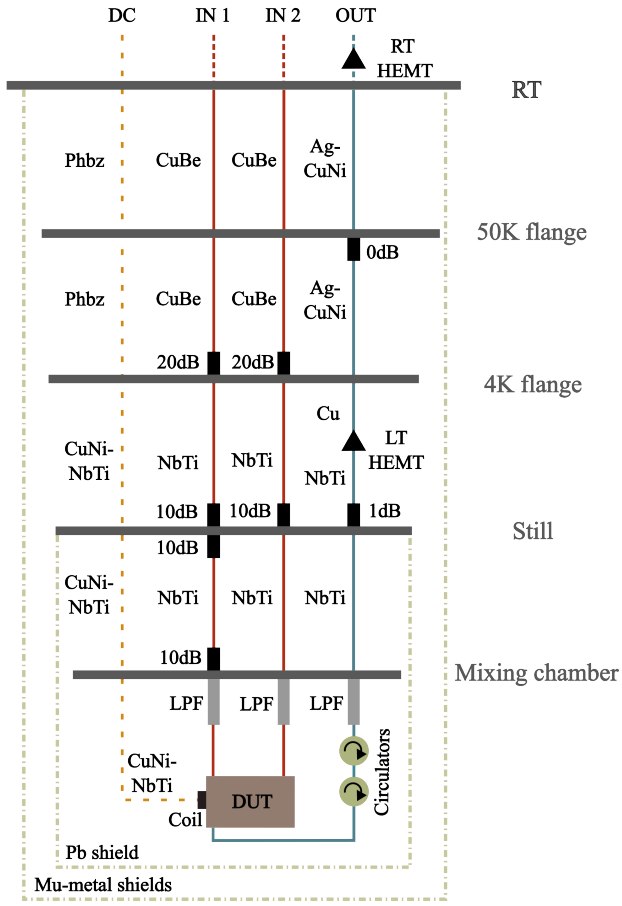

Figure 2.11: Schematics of the dilution refrigerator cabling for qubit and thin film resistance measurements. The material of each cable is indicated next to the line. Phbz stands for phosphor-bronze LT and RT HEMT are the low-temperature and room-temperature microwave HEMT amplifiers, respectively LPF stands for low-pass filters and DUT is the device under test.

in the coil, we tune the magnetic flux through the qubit loop while scanning in frequency with the VNA. The second type of spectroscopy is the two-tone measurement. In this case, we fix the VNA frequency tone at the resonator's resonant frequency while a second tone generated by the RF-source is scanned to

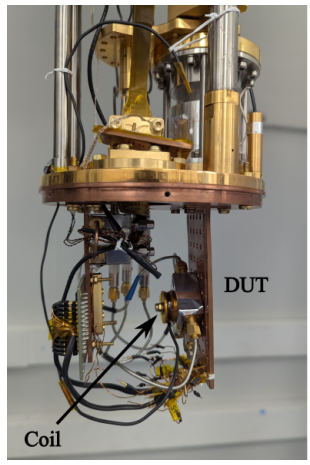

Figure 2.12: Image of the mixing chamber stage wiring. The sample box is mounted on the rightmost bracket. The different RF lines are connected to the side connectors of the sample box and the superconducting coil is screwed on the top lid.

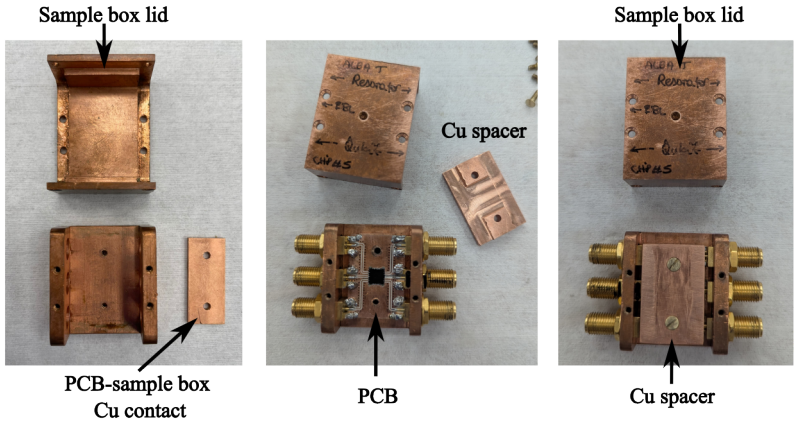

Figure 2.13: Images describing the assembly of the sample box. The Cu spacer piece is used to fill empty space and to avoid unwanted box modes.

search the qubit frequency. When the RF-source frequency matches the qubit, a shift in the resonator transmission amplitude is observed, as the excitation of the

qubit produces a state-dependent dispersive shift in the resonator which depends on detuning and coupling. One can obtain the qubit spectrum by running this measurement as a function of the magnetic flux. A detailed description of qubit measurements and the setup used in the group can be found in the PhD work of [Lóp24].

Chapter 3

Superinductive ultrastrong couplings: Theory

Alba Torras-Coloma, J.J. Garcia-Ripoll and P. Forn-Díaz

Contents

In this chapter, we present the derivations of the circuit Hamiltonians as well as the simulation methods to obtain the spectra of the different circuits studied in this thesis. We start from the smallest building block: the flux qubit with a non-negligible inductor. Then, we build up towards the complete qubit-resonator

system. The results and techniques developed in this chapter will be employed in Ch. 4 where the experimental implementation is presented.

3.1 Introduction and description of the system

Circuit quantum electrodynamics (circuit QED) is the study of quantum optics with superconducting quantum circuits. The physics of circuit QED systems arises from the engineering of linear and non-linear superconducting elements and their interaction with quantized electromagnetic fields [Bla+21]. One of the advantages of circuit QED over cavity QED with atoms is the possibility of engineering the individual circuit elements composing the atom-like and photon-like excitations. In particular, in circuit QED, the dipolar interaction between the artificial atom and the electromagnetic mode can be tuned well beyond the limitation imposed by dipole moment and cavity volumes typically used in cavity QED [For+19; Wal+06]. Such a design freedom opens the door to studying physics phenomena and light-matter interaction regimes unattainable with atoms and cavities.

The recent studies in the ultrastrong coupling (USC) regime are a clear example of how experimental quantum optics has been enriched by the developments in circuit QED and superconducting qubits. The design flexibility of superconducting quantum circuits allows the engineering of interactions which are comparable to the frequencies of the individual elements of the system [For+19]. In the past decade, experiments using flux qubits inductively coupled to resonators have been able to reach couplings beyond $g/\omega_{\mathrm{r}} > 0.1$, with ω_{r} being the frequency of the resonator. These studies centered mostly on the properties of the USC regime transmission spectra [Nie+10; Yos+17b; Yos+17a], the counter-rotating wave physics in the perturbative USC regime [For+16; Che+17] or the effect of noise in the USC spectra [Tom+21]. Still, very few experiments have studied the role of dissipation in the USC regime. Some examples include the works [Mag+18; For+17] where a flux qubit is coupled to a waveguide that plays the role of the dissipative environment.

The USC regime has distinctive features that go beyond the spectral differences with other coupling regimes[For+19; Fri+19]. Theoretical works have described striking phenomena derived from the dynamics in the non-perturbative USC regime such as the prediction of light-matter excitations in the ground state and the possibility of having extracavity radiation originated from the spontaneous emission of virtual photons [De +09]. The observation of USC physics beyond the spectral features requires coherent systems in the USC regime. However, up to date, no experimental demonstrations exist of coherent superconducting qubit-resonator systems in the USC regime.

In Ch. 3 and 4, we present the experimental work inspired by the theoretical proposal from [Mag+21]. The work from *Magazzù, et al.* studies a flux qubit galvanically coupled to a dissipative resonator in the ultrastrong coupling regime. The particularity of *Magazzù, et al.* proposal is that the system has two probing lines, one coupling to each element of the circuit. By using either line, information of the complete system can be extracted using resonator or qubit observables. From an experimental point of view, implementing a qubit-resonator system with two probing lines requires a thorough study of the circuit Hamiltonian and its parameters followed by a design of the device and the chip fabrication and measurements.

The circuit that we aim to study is a C-shunted 3-Josephson junction flux qubit galvanically coupled to an LC oscillator by a shared linear inductor in the USC regime. We begin this chapter by studying the Hamiltonian of the qubit-resonator circuit, a key step before proceeding to design and fabrication. During this process, we show how to derive the coupling coefficient from the circuit parameters and how to link the Quantum Rabi model to our circuit design. The derivations shown here will then be used in Ch. 4 to design a chip in the ultrastrong coupling regime.

3.2 3-junction flux qubit with a non-negligible loop inductance

Before diving into the derivation of the complete qubit-resonator circuit, it is necessary to understand the effect an inductor has on the flux qubit properties. These results will help to understand the resulting Hamiltonian and the spectrum of the coupled system. In Fig. 3.1, we present the circuit for a 3-junction flux qubit with a non-negligible loop inductance, L_{c}. The central junction of the design is a factor α smaller than the rest and it is shunted by a capacitor C_{sh}.

The Hamiltonian of the circuit is given by

$$\begin{aligned}\hat{\mathcal{H}} =& 4E_C\left((\hat{n}_1+\hat{n}_4)^2+(\hat{n}_3+\hat{n}_4)^2+\frac{\hat{n}_4^2}{\tilde{\alpha}}\right)-E_{\mathrm{J}}\cos\hat{\varphi}_1+\\ &-E_{\mathrm{J}}\cos\hat{\varphi}_3-\alpha E_{\mathrm{J}}\cos\left(\hat{\varphi}_4-\hat{\varphi}_1-\hat{\varphi}_3+2\pi f\right)+\frac{E_{\mathrm{J}}}{2\beta_L}\hat{\varphi}_4^2,\end{aligned} \tag{3.1}$$

where the charging energy is given by $E_C=\frac{2e^2}{C_{\mathrm{J}}}$ with C_{J} the Josephson capacitance. The Josephson energy is defined as $E_{\mathrm{J}}=\Phi_0 I_c/2\pi$, with I_C the critical current of the junction, and we use $\tilde{\alpha}=\alpha+C_{sh}/C_{\mathrm{J}}$ and $\beta_L=L_{\mathrm{c}}/L_J=2\pi L_{\mathrm{c}}I_c/\Phi_0=E_{\mathrm{J}}/E_L$, with $E_L=\Phi_0^2/4\pi^2L_{\mathrm{c}}$ being the inductive energy from the inductor. Note that the Hamiltonian is essentially the same as the one of a

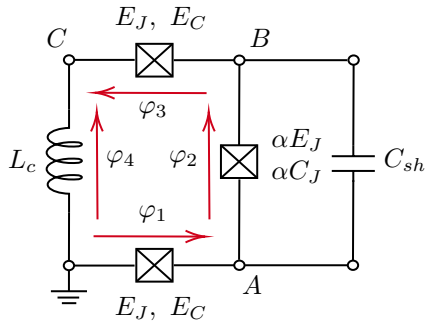

Figure 3.1: Circuit for a C-shunted 3-junction flux with a non-negligible loop inductance.

3-junction flux qubit but the linear inductance introduces a new harmonic term with the qubit capacitance proportional to $\hat{\varphi}_4^2$.

In Fig. 3.2 we compare the spectrum and the potential energy of a 3-junction flux qubit with and without loop inductance. The parameters used for the simulations are listed in Table 3.1. The selection of parameters is motivated by the design presented in Ch. 4. In particular, we choose a value of $L_c = 0.5\,\mathrm{nH}$ since it is relatively easy to obtain in terms of fabrication (see Sec. 4.1) yielding $\beta_L < 1$, so that the circuit is still in the flux qubit regime as we will discuss below.

Table 3.1: Simulation parameters for a 3-junction flux qubit with a non-negligible loop inductance. The resulting energies for these set of parameters are $E_C/h = 4.9\,\mathrm{GHz}$ and $E_J/h = 93.5\,\mathrm{GHz}$. S_c and C_c are estimated while C_{sh} is simulated.

J_c (μA/μm^2)	A (μm^2)	α	S_c (fF/μm^2)	C_{sh} (fF)	C_c (fF)	L (nH)	β_L
2.4	0.0784	0.58	50	7.3	0.447	0.5	0.29

The incorporation of the loop inductance has several effects on the energy and spectrum of the flux qubit. In Fig. 3.2, we see that it brings the qubit gap to lower frequencies while relaxing the condition for the double-well potential energy [Rob+06]. The latter will be discussed in more detail in Sec. 3.2.1. The addition of an inductance in the loop has also an effect on the anharmonicity and persistent current of the qubit. For $\beta_L \lesssim 1$, or equivalently $E_J \lesssim E_L$, at the sweetspot both the persistent current and the anharmonicity of the qubit increase, while the qubit gap decreases compared to the 3JJ case. However, for values of $\beta_L \gg 1$, we start entering the fluxonium regime [Yan+20; Man+09], the persistent current decreases while the system keeps a large anharmonicity and a small gap. In Fig. 3.3, we present the evolution of the persistent current as a

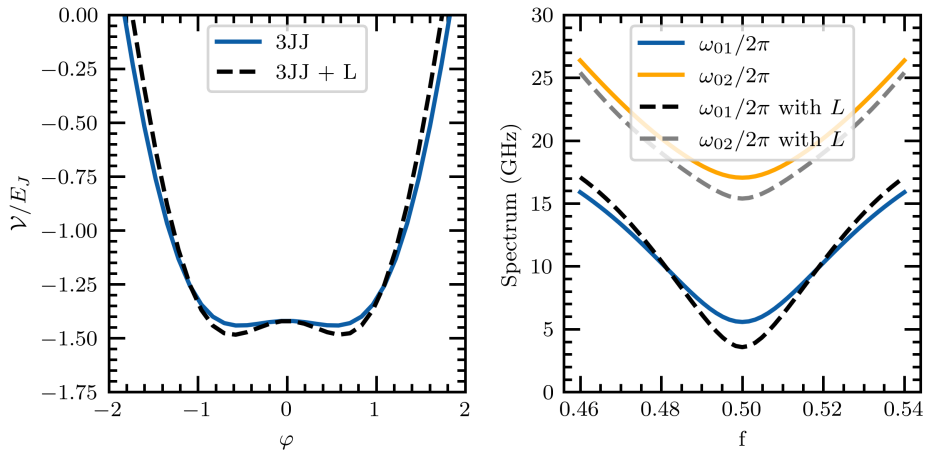

(a) (b)

Figure 3.2: Comparison of a flux qubit with and without loop inductance. (a) Potential cut defined by Eqs. (3.3) and (3.4) displaying a double well for a 3-junction flux qubit (solid line) and a 3-junction flux qubit with an inductance L in the loop (dashed line). (b) Comparison of the resulting spectrum for a 3-junction flux qubit with (dashed) and without (solid) loop inductance. The parameters used for the simulations are listed in Table 3.1.

function of β_L for the parameters listed in Table 3.1. The maximum persistent current occurs for $\beta_L \sim 1.2$ and it drops below the 3-Josephson junction case without inductance for $\beta_L \sim 3.9$ for the particular set of parameters used in our simulation.

3.2.1 Criteria for a double-well potential

As we have seen in the previous section, the potential energy of a 3-junction flux qubit is significantly modified by the incorporation of a non-negligible loop inductance, or in other words when E_J is comparable to E_L [Rob+06]. In this section, we study the conditions for a double-well potential energy in this regime. We start considering the potential energy in Eq. (3.1),

$$\begin{aligned}\hat{\mathcal{V}}/E_J = &-\cos\hat{\varphi}_1 - \cos\hat{\varphi}_3 - \alpha\cos\left(\hat{\varphi}_4 - \hat{\varphi}_1 - \hat{\varphi}_3 + 2\pi f\right) + \\ &+ \frac{1}{2\beta_L}\hat{\varphi}_4^2.\end{aligned} \tag{3.2}$$

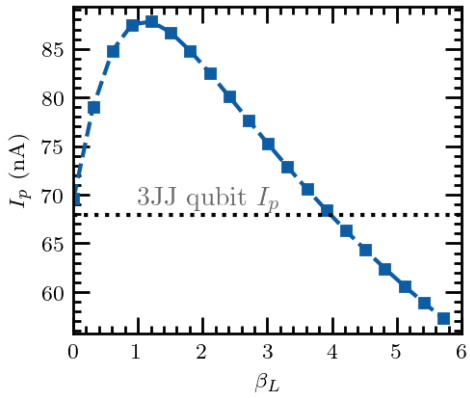

Figure 3.3: Persistent current of a 3JJ flux qubit with a loop inductance as a function of the parameter $\beta_L = E_J/E_L$. The parameters used for the simulation are listed in Table 3.1. The dashed line indicates the resulting I_p for the same 3JJ flux qubit without inductance.

To derive the condition for a double-well potential energy we need to calculate $\nabla\hat{\mathcal{V}} = 0$, which leads to the relations

$$\varphi_1^* = \varphi_3^* = \varphi^*, \tag{3.3}$$

$$\varphi_4^* = -\beta_L \sin\varphi^*, \tag{3.4}$$

$$\sin\varphi^* = \alpha \sin\left(-\beta_L \sin\varphi^* + 2\pi f - 2\varphi^*\right). \tag{3.5}$$

The first two relations define the cut plane across the double-well potential, while the last one gives the condition to reach to a critical point in the function in Eq. (3.2). For a double-well potential we need two minima which corresponds to imposing that Eq. (3.5) has at least two solutions. If we set $f = 0.5$, we see that the trivial solution $\varphi^* = 0$ fulfills the relation. To find a second solution, we use a numerical approach. In Fig. 3.4, we plot the region where the double-well condition is fulfilled for different values of α and β_L. Note that for a standard 3-junction flux qubit we need $\alpha > 0.5$, while adding an inductor to the system relaxes this constraint. The double-well condition is especially important at the time of designing the flux qubit. In order to operate in the flux qubit regime, we want the qubit to have a double-well potential energy with energies $E_J \lesssim E_L$. Having Josephson energies below or on the order of the inductive energies ensures that the harmonic potential in Eq. (3.1) does not dominate over the non-linear terms.

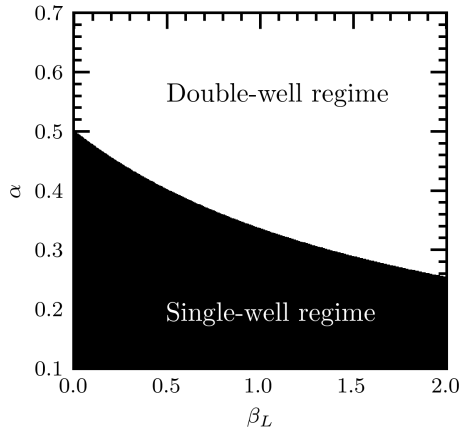

Figure 3.4: Condition for a double-well potential in a 3JJ flux qubit with a non-negligible loop inductance. The white area corresponds to the values of α and β that give two solutions to Eq. (3.5)

3.3 3-junction flux qubit galvanically coupled to an LC resonator

In this thesis, we are particularly interested in the study of the circuit consisting of a 3-Josephson junction flux qubit galvanically coupled to an LC oscillator. The circuit schematics is shown in Fig. 3.5. The qubit loop is interrupted by three junctions and an inductance L_c shared with the resonator. The central junction of the loop is made a factor $\alpha \simeq 0.6$ smaller and $\beta_L \lesssim 1$, in order to operate the flux qubit in the double-well regime (see Fig. 3.4).

In the upcoming sections we derive the circuit Hamiltonian. We show how to derive an expression for the qubit-resonator coupling coefficient and the relation with the Quantum Rabi Hamiltonian presented in Sec. 1.2.1. Finally, we propose two different diagonalization methods to optimize the simulation of the qubit-resonator spectrum in the USC regime.

3.3.1 Circuit Hamiltonian derivation

We begin the Hamiltonian derivation by defining the node and branch variables of the system [Rip22]. In Fig. 3.5, we show the convention used. We label nodes from A to D starting from the ground in a counter-clockwise fashion.

Following the defined current directions, the flux branch variables of the sys-

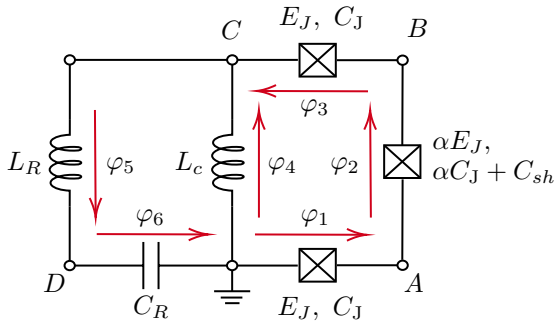

Figure 3.5: Circuit of a 3-junction flux qubit galvanically coupled to an LC oscillator. The letters denote the nodes of the circuit and the arrows the spanning tree.

tem are given by the following relations,

$$\begin{aligned}
\phi_1 &= \phi_A - \phi_{\text{gnd}} = \phi_A, \\
\phi_2 &= \phi_B - \phi_A, \\
\phi_3 &= \phi_C - \phi_B, \\
\phi_4 &= \phi_C - \phi_{\text{gnd}}, \\
\phi_5 &= \phi_D - \phi_C, \\
\phi_6 &= \phi_{gnd} - \phi_D = -\phi_D.
\end{aligned}$$

From Kirchhoff laws, we can derive the equations of motion of the circuit. If we integrate them considering the Euler-Lagrange equation [Lan+82], we are able to derive the Lagrangian in terms of the flux branch variables,

$$\begin{aligned}
\mathcal{L} = &\frac{C_\text{J}}{2}\left(\dot{\phi}_1^2 + \tilde{\alpha}(\dot{\phi}_4 - \dot{\phi}_1 - \dot{\phi}_3)^2 + \gamma\dot{\phi}_3^2 + \frac{C_\text{R}}{C_\text{J}}\dot{\phi}_6^2\right) + E_\text{J}\cos\left(\frac{2\pi}{\Phi_0}\phi_1\right) + \\
&+ \gamma E_\text{J}\cos\left(\frac{2\pi}{\Phi_0}\phi_3\right) + \alpha E_\text{J}\cos\left(\left(\frac{2\pi}{\Phi_0}\right)(\phi_4 - \phi_3 - \phi_1 + \phi_{ext})\right) + \\
&- \frac{1}{2}\left(\frac{\phi_4^2}{L_\text{c}} + \frac{(\phi_4 + \phi_6)^2}{L_\text{R}}\right),
\end{aligned} \tag{3.6}$$

where we have used the fluxoid quantization condition $\phi_2 = 2\pi f - \phi_1 - \phi_3 + \phi_4$. L_c denotes the coupling inductance, L_R and C_R are the resonator inductance and capacitance, respectively, and C_J is the capacitance of the junction. The prefactor γ is added to consider any size mismatch between the two big qubit junctions. In

order to make the notation more compact, we define the term $\tilde{\alpha} = \alpha + C_{sh}/C_{\mathrm{J}}$ which takes into account the shunt capacitor of the small junction.

Introducing $\phi_i \frac{2\pi}{\Phi_0} = \varphi_i$ and $\phi_{\mathrm{ext}} \frac{2\pi}{\Phi_0} = 2\pi f$ into the previous Lagrangian we obtain

$$\begin{aligned}\mathcal{L} = &\frac{C_{\mathrm{J}}}{2}\left(\frac{\Phi_0}{2\pi}\right)^2\left(\dot{\varphi}_1^2 + \tilde{\alpha}(\dot{\varphi}_4 - \dot{\varphi}_1 - \dot{\varphi}_3)^2 + \gamma\dot{\varphi}_3^3 + \frac{C_{\mathrm{R}}}{C_{\mathrm{J}}}\dot{\varphi}_6^2\right) + \\ &+ E_{\mathrm{J}}\cos\varphi_1 + \gamma E_{\mathrm{J}}\cos\varphi_3 + \alpha E_{\mathrm{J}}\cos(\varphi_4 - \varphi_3 - \varphi_1 + 2\pi f) + \\ &- \frac{1}{2}\left(\frac{\Phi_0}{2\pi}\right)^2\left(\frac{\varphi_4^2}{L_{\mathrm{c}}} + \frac{(\varphi_4 + \varphi_6)^2}{L_{\mathrm{R}}}\right).\end{aligned} \tag{3.7}$$

We can use the conjugate variables of the system, $p_i = \partial\mathcal{L}/\partial\dot{\varphi}_i$ and the Legendre transformation to obtain an expression for the Hamiltonian,

$$\begin{aligned}\mathcal{H} = &\left(\frac{2\pi}{\Phi_0}\right)^2\frac{1}{2C_{\mathrm{J}}}\left((p_1 + p_4)^2 + \frac{1}{\gamma}(p_3 + p_4)^2 + \frac{p_4^2}{\tilde{\alpha}} + \frac{C_{\mathrm{J}}}{C_{\mathrm{R}}}p_6^2\right) + \\ &- E_{\mathrm{J}}\cos\varphi_1 - \gamma E_{\mathrm{J}}\cos\varphi_3 - E_{\mathrm{J}}\cos(\varphi_4 - \varphi_1 - \varphi_3 + 2\pi f) + \\ &+ \frac{1}{2L_{\mathrm{c}}}\left(\frac{\Phi_0}{2\pi}\right)^2\varphi_4^2 + \frac{1}{2L_{\mathrm{R}}}\left(\frac{\Phi_0}{2\pi}\right)(\varphi_6 + \varphi_4)^2.\end{aligned} \tag{3.8}$$

Finally, promoting the variables to quantum mechanical operators and introducing the charge operator $\hat{n}_i = -\frac{2\pi}{\Phi_0}\frac{\hat{p}_i}{2e}$, we obtain the Hamiltonian in terms of $\hat{n}_i$ and $\hat{\varphi}_i$,

$$\begin{aligned}\hat{\mathcal{H}} = &\frac{(2e)^2}{2C_{\mathrm{J}}}\left((\hat{n}_1 + \hat{n}_4)^2 + \frac{1}{\gamma}(\hat{n}_3 + \hat{n}_4)^2 + \frac{\hat{n}_4^2}{\tilde{\alpha}} + \frac{C_{\mathrm{J}}}{C_{\mathrm{R}}}\hat{n}_6^2\right) + \\ &+ \frac{1}{2}\left(\frac{\Phi_0}{2\pi}\right)^2\left(\frac{\hat{\varphi}_4^2}{L_{\mathrm{c}}} + \frac{(\hat{\varphi}_4 + \hat{\varphi}_6)^2}{L_{\mathrm{R}}}\right) - E_{\mathrm{J}}\cos\hat{\varphi}_1 + \\ &- \gamma E_{\mathrm{J}}\cos\hat{\varphi}_3 - \alpha E_{\mathrm{J}}\cos(\hat{\varphi}_4 - \hat{\varphi}_1 - \hat{\varphi}_3 + 2\pi f).\end{aligned} \tag{3.9}$$

Note that this Hamiltonian contains the 3-junction flux qubit with a non-negligible inductance renormalized by L_{R} and L_{c} and the Hamiltonian for a harmonic oscillator with L_{R} and C_{R}. There is one last term given by $\hat{\varphi}_6\hat{\varphi}_4/L_{\mathrm{R}}$ that couples variables coming from the qubit and the resonator. In the following section we will show how to derive the qubit-resonator coupling coefficient from the circuit Hamiltonian.

3.3.2 Coupling estimate

Obtaining a proper estimate of the qubit-resonator coupling coefficient g is key to designing a system in the USC regime. In this subsection, we will consider two limit cases to treat the derivation of the Quantum Rabi Hamiltonian often disregarded in the literature. In particular, we will show that proper treatment of the linear oscillator terms provides a solution to the inconsistency of resonator frequencies obtained in recent experiments [Tom+21; Tom+25]. In the following, we consider the two limit cases given by: $L_\mathrm{c} \sim L_\mathrm{R}$, $L_\mathrm{c} \ll L_\mathrm{J}$ and $L_\mathrm{c} \ll L_\mathrm{R}$, $L_\mathrm{c} \sim L_\mathrm{J}$.

Case: $L_\mathrm{c} \ll L_\mathrm{R}$, $L_\mathrm{c} \lesssim L_\mathrm{J}$

We start by considering the Hamiltonian in Eq. (3.9). For $L_R \gg L_c$ and $L_\mathrm{J} \lesssim L_c$, the shared inductor contributes mainly to the qubit circuit and the linear oscillator mode will be described by the bare resonator with frequency $\omega_R = \frac{1}{\sqrt{L_R C_R}}$. The derivation of g is equivalent to others shown in experimental works with similar qubit-resonator systems [Tom+21]. Therefore, the following terms can be identified in the total Hamiltonian: one describing the qubit, another describing the resonator, and an interaction term, which are shown below,

$$\begin{aligned}\hat{\mathcal{H}}_\mathrm{q} = &\frac{(2e)^2}{2C_\mathrm{J}}\left((\hat{n}_1+\hat{n}_4)^2+(\hat{n}_3+\hat{n}_4)^2+\frac{\hat{n}_4^2}{\tilde{\alpha}}\right)+\\ &+\frac{\hat{\varphi}_4^2}{2}\left(\frac{\Phi_0}{2\pi}\right)^2\left(\frac{1}{L_\mathrm{c}}+\frac{1}{L_\mathrm{R}}\right)+\\ &-E_\mathrm{J}(\cos\hat{\varphi}_1+\cos\hat{\varphi}_3+\alpha\cos\left(\hat{\varphi}_4-\hat{\varphi}_1-\hat{\varphi}_3+2\pi f\right)),\end{aligned} \tag{3.10}$$

$$\hat{\mathcal{H}}_\mathrm{r} = \frac{(2e)^2}{2C_\mathrm{R}}\hat{n}_6^2+\frac{1}{2}\left(\frac{\Phi_0}{2\pi}\right)^2\frac{\hat{\varphi}_6^2}{L_\mathrm{R}} \tag{3.11}$$

$$\hat{\mathcal{H}}_\mathrm{int} = \left(\frac{\Phi_0}{2\pi}\right)^2\frac{\hat{\varphi}_4\hat{\varphi}_6}{L_\mathrm{R}}. \tag{3.12}$$

However, the Quantum Rabi model considers the interaction of a two-level atom with an electromagnetic field mode. In order to obtain an equivalent expression, we have to diagonalize the qubit Hamiltonian in Eq. (3.10) and project it on the basis of the two lowest qubit energy states $\{|0\rangle, |1\rangle\}$. These two states define the qubit basis. This is generally true for flux qubits due to their large anharmonicity ($\mathcal{A}$), with typical values of $\mathcal{A}/\Delta_\mathrm{q}$ between 0.3 and 2 [Yan+16], where Δ_q is the qubit gap. Now let's consider the resonator Hamiltonian. It is essentially a harmonic LC oscillator. We can rewrite it in the Fock state basis to provide the final expression in terms of the creation and annihilation operators ($\hat{a}^\dagger$, $\hat{a}$).

Considering these changes, the interaction Hamiltonian can be rewritten as,

$$\begin{aligned}\hat{\mathcal{H}}_{int} &= \frac{E_{\mathrm{J}}}{\beta_{L,R}}\hat{\varphi}_4\hat{\varphi}_R = \frac{E_{\mathrm{J}}}{\beta_{L,R}}\sqrt{\frac{\hbar}{2m_R\omega_{\mathrm{R}}}}(\hat{a}^\dagger+\hat{a})\sum_{k,k'=0,1}\langle k|\hat{\varphi}_4|k'\rangle|k\rangle\langle k'| = \\ &= \hbar(g_z\hat{\sigma}_z + g_x\hat{\sigma}_x)(\hat{a}^\dagger+\hat{a}),\end{aligned} \tag{3.13}$$

where we have used the definitions for the Josephson energy $E_{\mathrm{J}} = \Phi_0 I_c/2\pi$, the inductance ratio $\beta_{L,i} = 2\pi L_i I_c/\Phi_0$ and $m_{\mathrm{R}} \equiv C_{\mathrm{R}}\left(\Phi_0/2\pi\right)^2$. In the last expression, we use the Pauli operators $\hat{\sigma}_i$. We define g_i as the coupling coefficient contribution from the z, x components,

$$\hbar g_z = \frac{E_{\mathrm{J}}}{\beta_{L,R}}\sqrt{\frac{\hbar}{2m_R\omega_{\mathrm{R}}}}\left(\langle 0|\hat{\varphi}_4|0\rangle - \langle 1|\hat{\varphi}_4|1\rangle\right), \tag{3.14}$$

$$\hbar g_x = \frac{E_{\mathrm{J}}}{\beta_{L,R}}\sqrt{\frac{\hbar}{2m_R\omega_{\mathrm{R}}}}\left(\langle 0|\hat{\varphi}_4|1\rangle + \langle 1|\hat{\varphi}_4|0\rangle\right). \tag{3.15}$$

Using these results and considering the frequency difference from the qubit levels 0 and 1, $\Omega_q \equiv \omega_1 - \omega_0$, we can rewrite the Hamiltonian of the system in the Quantum Rabi model form,

$$\hat{\mathcal{H}}_{\mathrm{QRM}} = \hbar\Omega_q\hat{\sigma}_z + \hbar\omega_{\mathrm{R}}\left(\hat{a}^\dagger\hat{a} + \frac{1}{2}\right) + \hbar\left(g_z\hat{\sigma}_z + g_x\hat{\sigma}_x\right)\left(\hat{a}^\dagger + \hat{a}\right), \tag{3.16}$$

where Ω_q and ω_{R} are the qubit and resonator frequencies, respectively. In the two-state model, $g_x = g\Delta_{\mathrm{q}}/\omega_q$ and $g_z = g\epsilon/\omega_q$ where Δ_{q} is the qubit gap, $\epsilon = 2I_{\mathrm{p}}\left(\Phi_{\mathrm{ext}} - \frac{\Phi_0}{2}\right)$ is the magnetic energy of the qubit with I_{p} the persistent current, and Φ_{ext} the external flux. When the system is in the sweet spot, the component g_z of the coupling vanishes and we recover the standard form of the Quantum Rabi model presented in Eq. (1.7).

Eq. (3.16) can be rotated to the persistent current basis of the qubit $\{|L\rangle, |R\rangle\}$ using a unitary transformation $U = e^{-i\theta\hat{\sigma}_y}$,

$$U = \begin{pmatrix}\cos\theta/2 & -\sin\theta/2\\ \sin\theta/2 & \cos\theta/2\end{pmatrix}, \tag{3.17}$$

with $\tan\theta = \Delta_{\mathrm{q}}/\epsilon$ [For10]. With this change, the expression for the Quantum

Rabi model reads,

$$U^{\dagger}\hat{\mathcal{H}}_{\mathrm{QRM}}U = \hat{\mathcal{H}}'_{\mathrm{QRM}} = -\frac{1}{2}\left(\epsilon\hat{\sigma}_z + \Delta_{\mathrm{q}}\hat{\sigma}_x\right) + \\ + \hbar\omega_{\mathrm{R}}\left(\hat{a}^{\dagger}\hat{a} + \frac{1}{2}\right) + \hbar g\hat{\sigma}_z\left(\hat{a} + \hat{a}^{\dagger}\right), \tag{3.18}$$

where in the two-state model, $g = \sqrt{g_x^2 + g_z^2}$.

Case: $L_{\mathrm{c}} \sim L_{\mathrm{R}}$, $L_{\mathrm{c}} < L_{\mathrm{J}}$

As we will see in Ch. 4, inductors in the range $L_{\mathrm{c}} \simeq L_{\mathrm{R}}$ might be necessary to reach USC while keeping relatively low I_{p} to yield a high qubit coherence. Treating the resonator term for large coupling inductors $L_c \sim L_R$, implies considering the different linear modes of the system [Tor+; Bou+09]. The qubit-resonator interaction will not be described by a resonator with frequency ω_R, but by a normal mode with frequency ω_A.

Similarly to the previous case, we start from the complete Hamiltonian of the circuit in Eq. (3.9) but we group the terms into linear, non-linear and interaction,

$$\hat{\mathcal{H}}_{LC} = \left(\frac{2\pi}{\Phi_0}\right)^2\left(\frac{\hat{p}_4^2}{2C_{\mathrm{eff}}} + \frac{\hat{p}_6^2}{2C_R}\right) + \left(\frac{\Phi_0}{2\pi}\right)^2\left(\frac{\hat{\varphi}_4^2}{2L_{\mathrm{eff}}} + \frac{\hat{\varphi}_6^2}{2L_R} + \frac{\hat{\varphi}_4\hat{\varphi}_6}{L_R}\right), \tag{3.19}$$

$$\hat{\mathcal{H}}_{nl} = \left(\frac{2\pi}{\Phi_0}\right)^2\left(\frac{\hat{p}_1^2}{2C_J} + \frac{\hat{p}_3^2}{2C_J}\right) - E_J\cos\left(\hat{\varphi}_1\right) - E_J\cos\left(\hat{\varphi}_3\right), \tag{3.20}$$

$$\hat{\mathcal{H}}_{int}^{C} = \left(\frac{2\pi}{\Phi_0}\right)^2\frac{\hat{p}_4}{2C_J}\left(\hat{p}_1 + \hat{p}_3\right), \tag{3.21}$$

$$\hat{\mathcal{H}}_{int}^{L} = -\alpha E_J\cos(\hat{\varphi}_4 - \hat{\varphi}_1 - \hat{\varphi}_3 + 2\pi f), \tag{3.22}$$

where we have defined $L_{\mathrm{eff}}^{-1} = L_R^{-1} + L_c^{-1}$ and $C_{\mathrm{eff}}^{-1} = C_J^{-1} + (2C_J + 2\alpha C_{\mathrm{sh}})^{-1}$. Note that we have an inductive $\hat{\mathcal{H}}_{\mathrm{int}}^{L}$ and a capacitive $\hat{\mathcal{H}}_{\mathrm{int}}^{C}$ interaction terms.

Let us start by considering the LC Hamiltonian in Eq. (3.19). Each of the oscillator terms has an associated resonance frequency,

$$\omega_R^2 = \frac{1}{L_R C_R},\ \omega_4^2 = \frac{1}{L_{\mathrm{eff}}C_{\mathrm{eff}}},, \tag{3.23}$$

These two coupled harmonic oscillators can be decoupled by deriving the normal modes of the system with flux operators denoted by $\hat{\Phi}_{A,B}$ and normal mode frequencies $\omega_{A,B}$ (see Sec. 3.3.3 for an analytical expression). The Hamiltonian

in the normal mode basis reads,

$$\hat{\mathcal{H}}_{LC}^{NM} = \hbar\omega_A \left(\hat{a}_A^\dagger \hat{a}_A + \frac{1}{2}\right) + \hbar\omega_B \left(\hat{a}_B^\dagger \hat{a}_B + \frac{1}{2}\right). \tag{3.24}$$

Before defining a basis for the qubit, we need to treat the non-linear term in Eq. (3.20). We start by transforming $\hat{\varphi}_4$ into the normal mode basis using the transformation matrix U with entries U_{ij},

$$\hat{\mathcal{H}}_{\text{int}}^{L} = -\alpha E_J \cos\left(\left(\frac{2\pi}{\Phi_0}\right)\frac{U_{21}\hat{\Phi}_A + U_{22}\hat{\Phi}_B}{\sqrt{C_{\text{eff}}}} - \hat{\varphi}_1 - \hat{\varphi}_3 + 2\pi f\right). \tag{3.25}$$

Note that this term mixes modes A and B with qubit-like variables. U_{ij} are calculated explicitly in Sec. 3.3.3. For usual design parameters (see for example Ch. 4), $|\langle 0|\hat{\Phi}_{A,B}^2|0\rangle|^{1/2} \ll \Phi_0$ allowing the expansion,

$$\begin{aligned}\hat{\mathcal{H}}_{\text{int}}^{L} \simeq -\alpha E_{\text{J}}\Bigg[&\cos\left(-\hat{\varphi}_1 - \hat{\varphi}_3 + 2\pi f\right) + \\ &- \left(\frac{2\pi}{\Phi_0}\right)\frac{U_{21}\hat{\Phi}_A + U_{22}\hat{\Phi}_B}{\sqrt{C_{\text{eff}}}}\sin\left(-\hat{\varphi}_1 - \hat{\varphi}_3 + 2\pi f\right)\Bigg],\end{aligned} \tag{3.26}$$

where we have a qubit-like term and an interaction potential. This expansion allows to convert the non-linear Hamiltonian $\hat{\mathcal{H}}_{nl}$ into a similar 3JJ qubit Hamiltonian,

$$\begin{aligned}\hat{\mathcal{H}}_{qb} = &\left(\frac{2\pi}{\Phi_0}\right)^2\left(\frac{\hat{p}_1^2}{2C_J} + \frac{\hat{p}_3^2}{2C_J}\right) - E_J\cos\left(\hat{\varphi}_1\right) - E_J\cos\left(\hat{\varphi}_3\right) + \\ &- \alpha E_J\cos\left(-\hat{\varphi}_1 - \hat{\varphi}_3 + 2\pi f\right).\end{aligned} \tag{3.27}$$

We can define the qubit basis considering the two lowest energy eigenstates $\{|0\rangle, |1\rangle\}$ of $\hat{\mathcal{H}}_{qb}$ as usual.

The following steps are equivalent to the previous derivation, with the difference that we have an extra capacitive coupling term. Using the two-level qubit basis and the normal modes, the capacitive interaction reads,

$$\hat{\mathcal{H}}_{\text{int}}^{C} = \left(\frac{2\pi}{\Phi_0}\right)^2 \frac{\hat{p}_4}{2C_J}\left(\hat{p}_1 + \hat{p}_3\right) = \hbar \sum_{j=A,B}\sum_{k,l} g_{C,j}^{kl}(\hat{a}_j^\dagger - \hat{a}_j)|k\rangle\langle l|, \tag{3.28}$$

where $U_A \equiv U_{21}$, $U_B \equiv U_{22}$ and the coupling coefficient $g^{kl}_{C,j}$ is,

$$\hbar g^{kl}_{C,j} = i\left(\frac{2\pi}{\Phi_0}\right)^2 \frac{\sqrt{C_{\text{eff}}}}{C_J} U_j \sqrt{\frac{\hbar\omega_j}{2}} \langle k|(\hat{p}_1 + \hat{p}_3)|l\rangle. \tag{3.29}$$

The same applies for the inductive interaction,

$$\begin{aligned} U^{\text{int}}_{J4} &= \alpha E_J \left(\frac{2\pi}{\Phi_0}\right) \frac{U_{21}\hat{\Phi}_A + U_{22}\hat{\Phi}_B}{\sqrt{C_{\text{eff}}}} \sin\left(-\hat{\varphi}_1 - \hat{\varphi}_3 + 2\pi f\right) = \\ &= \hbar \sum_{j=A,B} \sum_{k,l} g^{kl}_{L,j} (\hat{a}^\dagger_j + \hat{a}_j)|k\rangle\langle l|, \end{aligned} \tag{3.30}$$

with coupling coefficient $g^{kl}_{L,j}$,

$$\hbar g^{kl}_{L,j} = \alpha E_{\text{J}} \left(\frac{2\pi}{\Phi_0}\right) \frac{U_j}{\sqrt{C_{\text{eff}}}} \sqrt{\frac{\hbar}{2\omega_j}} \langle k| \sin(-\hat{\varphi}_1 - \hat{\varphi}_3 + 2\pi f)|l\rangle. \tag{3.31}$$

Typically for flux qubits $\hbar\omega_j \ll E_{\text{J}}$, and the capacitive coupling terms can be neglected. The total Hamiltonian in the qubit and normal mode basis can be written in the Quantum Rabi model form,

$$\begin{aligned} \hat{\mathcal{H}}^{NM}_{QRM} = \hbar\frac{\Omega_q}{2}\hat{\sigma}_z + \hbar\omega_A\left(\hat{a}^\dagger_A\hat{a}_A + \frac{1}{2}\right) + \hbar\omega_B\left(\hat{a}^\dagger_B\hat{a}_B + \frac{1}{2}\right) + \\ + \hbar(g^z_A\hat{\sigma}_z + g^x_A\hat{\sigma}_x)(\hat{a}^\dagger_A + \hat{a}_A) + \hbar(g^z_B\hat{\sigma}_z + g^x_B\hat{\sigma}_x)(\hat{a}^\dagger_B + \hat{a}_B), \end{aligned} \tag{3.32}$$

where the system is described as the interaction of a qubit with two harmonic oscillators.

3.3.3 Approximate expressions for the coupling coefficient

In the previous section we have described the general approach to derive the coupling coefficient for the case of a flux qubit galvanically coupled to a resonator. However, obtaining the value of the coupling coefficient requires simulating the qubit and evaluating the different expressions numerically. To gain some intuition on the scaling of the coupling coefficient with the different circuit components, one can derive analytical approximate expressions valid in specific regimes of interaction. These expressions are particularly useful at the time of designing devices targeting the USC regime.

Approximate expression for the coupling coefficient: case $L_c \ll L_R$

We will start considering the case $L_c \ll L_R$ and a coupling in the perturbative USC regime. We will not provide the full derivation in this text but rather give the idea on how to reach the final result. The detailed derivation can be found in [Tor+25].

For perturbative couplings ($0.1 < g/\omega_R < 0.3$) and $L_c \ll L_R$, we can assume that the phase across the coupling inductor $\hat{\varphi}_4$ in Eq. (3.9) is in a quasi-steady state. This allows us to impose that the potential is in a minimum with respect to $\hat{\varphi}_4$ and obtain the following expression for the coupling strength,

$$g \simeq \frac{L_c L_R}{\hbar(L_c + L_R)} I_{rms} I_p, \tag{3.33}$$

where I_p is the persistent current of the qubit, L_c is the coupling inductance and $I_{rms} = \sqrt{\frac{\hbar\omega_R}{2L_R}} = \frac{1}{Z_R}\sqrt{\frac{\hbar\omega_R}{2C_R}}$ is the root mean square current of the resonator with $Z_R = \sqrt{L_R/C_R}$ its impedance and $\omega_R = 1/\sqrt{L_R C_R}$ its resonance frequency. In this regime, the resonator frequency is renormalized by L_c as $\omega_r = 1/\sqrt{C_R(L_R + L_c)}$.

In the limit $L_c \ll L_R$ the coupling becomes,

$$g \simeq \frac{I_p L_c I_{rms}}{\hbar} = \frac{I_p L_c}{\hbar Z_R}\sqrt{\frac{\hbar\omega_R}{2C_R}}. \tag{3.34}$$

From this result, it is clear that in order to reach ultrastrong couplings, we have to design flux qubits with large persistent currents I_p, use large shared inductances L_c, and low-impedance resonators Z_R.

Approximate expression for the coupling: general case in the coupled oscillators approach

The previous derivation is valid as long as the system is both in the perturbative USC and the coupling inductance is small compared to the resonator inductance, $L_c \ll L_R$. However, as previously mentioned, inductors in the range $L_c \simeq L_R$ might be necessary to reach the non-perturbative USC regime while keeping relatively low I_p to maintain a high qubit coherence. In this subsection, we derive a new approximate expression for the coupling coefficient that considers $L_c \sim L_R$.

The derivation is equivalent to the one shown in Sec. 3.3.2 for the normal mode approach. However, provided that the capacitive interaction is negligible, we will first consider the qubit-resonator circuit depicted in Fig. 3.6 without the influence of the qubit junctions potential. The Hamiltonian in Eq. (3.19) holds

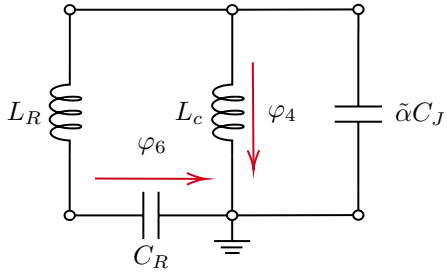

Figure 3.6: Coupled resonator circuit obtained neglecting the influence of qubit junctions. L_R and C_R are the inductance and capacitance of the resonator, respectively. L_c is the coupling inductor and $\tilde{\alpha}C_\mathrm{J} = C_\mathrm{J}+C_\mathrm{sh}$ is the total capacitance of the small qubit junction.

with the change $C_\mathrm{eff} \to \tilde{\alpha}C_J$. For convenience, to derive an explicit formula for the normal modes, we rescale the variables of the circuit such that they preserve the commutation relations,

$$\hat{P}_6 = \left(\frac{2\pi}{\Phi_0}\right)\frac{\hat{p}_6}{\sqrt{C_\mathrm{R}}}, \quad \hat{\Phi}_6 = \sqrt{C_\mathrm{R}}\left(\frac{\Phi_0}{2\pi}\right)\hat{\varphi}_6, \tag{3.35}$$

$$\hat{P}_4 = \left(\frac{2\pi}{\Phi_0}\right)\frac{\hat{p}_4}{\sqrt{\tilde{\alpha}C_\mathrm{J}}}, \quad \hat{\Phi}_4 = \sqrt{\tilde{\alpha}C_\mathrm{J}}\left(\frac{\Phi_0}{2\pi}\right)\hat{\varphi}_4, \tag{3.36}$$

and the Hamiltonian in Eq. (3.19) reads,

$$\hat{\mathcal{H}}_{LC} = \frac{\hat{P}_6^2}{2} + \frac{\hat{P}_4^2}{2} + \frac{1}{2}\begin{pmatrix}\hat{\Phi}_6 & \hat{\Phi}_4\end{pmatrix}\begin{pmatrix}\omega_\mathrm{R}^2 & \tilde{g}^2 \\ \tilde{g}^2 & \omega_4^2\end{pmatrix}\begin{pmatrix}\hat{\Phi}_6 \\ \hat{\Phi}_4\end{pmatrix}, \tag{3.37}$$

with the coupling between modes given by

$$\tilde{g}^2 = \frac{1}{L_\mathrm{R}\sqrt{C_\mathrm{R}\tilde{\alpha}C_\mathrm{J}}}. \tag{3.38}$$

The coupled system can be transformed to the normal mode basis by diagonalizing the matrix given in Eq. (3.37). We obtain the normal mode frequencies from the eigenvalues $\omega_A^2 = \lambda_-$ and $\omega_B^2 = \lambda_+$, where

$$\lambda_\pm = \frac{\omega_\mathrm{R}^2 + \omega_4^2}{2} \pm \sqrt{\left(\frac{\Omega^2}{2}\right)^2 + \tilde{g}^4}, \tag{3.39}$$

with $\Omega^2 = \omega_\mathrm{R}^2 - \omega_4^2$. Therefore, $\omega_A < \omega_B$.

Once the normal modes of the oscillator are known, we reintroduce the effect of the qubit into the Hamiltonian and consider the complete Hamiltonian in Eq. (3.9). The qubit-resonator coupling in this approach is mediated by the term,

$$U_{J4} = -\alpha E_{\rm J} \cos\left(\left(\frac{2\pi}{\Phi_0}\right)\frac{\hat{\Phi}_4}{\sqrt{\tilde{\alpha}C_{\rm J}}} - \hat{\varphi}_1 - \hat{\varphi}_3 + 2\pi f\right), \tag{3.40}$$

which mixes normal modes A and B with the qubit. In order to see this effect more clearly, we can transform $\hat{\Phi}_4$ into the normal mode basis using the transformation matrix obtained from the normal mode eigenvectors

$$U = \begin{pmatrix} \frac{1}{N_-}\left[\frac{\Omega^2}{2} - \sqrt{\left(\frac{\Omega^2}{2}\right)^2 + \tilde{g}^4}\right] & \frac{1}{N_+}\left[\frac{\Omega^2}{2} + \sqrt{\left(\frac{\Omega^2}{2}\right)^2 + \tilde{g}^4}\right] \\ \frac{\tilde{g}^2}{N_-} & \frac{\tilde{g}^2}{N_+} \end{pmatrix}, \tag{3.41}$$

where $N_\pm^2 \equiv 2\left[\left(\frac{\Omega^2}{2}\right)^2 + \tilde{g}^4\right] \pm \Omega^2\sqrt{\left(\frac{\Omega^2}{2}\right)^2 + \tilde{g}^4}$.

The interaction term can be rewritten as,

$$\begin{aligned} U_{J4} \simeq -\alpha E_{\rm J}\Bigg[&\cos\left(-\hat{\varphi}_1 - \hat{\varphi}_3 + 2\pi f\right) + \\ &- \left(\frac{2\pi}{\Phi_0}\right)\frac{U_{21}\hat{\Phi}_A + U_{22}\hat{\Phi}_B}{\sqrt{\tilde{\alpha}C_{\rm J}}}\sin\left(-\hat{\varphi}_1 - \hat{\varphi}_3 + 2\pi f\right)\Bigg], \end{aligned} \tag{3.42}$$

where the interaction between the resonator modes and the qubit is concentrated in the term,

$$U_{J4}^{\rm int} = \frac{U_{21}\hat{\Phi}_A + U_{22}\hat{\Phi}_B}{\sqrt{\tilde{\alpha}C_{\rm J}}}\hat{I}_\alpha, \tag{3.43}$$

with $\hat{I}_\alpha \equiv \alpha I_C \sin\left(-\hat{\varphi}_1 - \hat{\varphi}_3 + 2\pi f\right)$. In general, mode B will be much higher in frequency than mode A, therefore it is safe to consider that it sits in its ground state. One can perform a Born-Oppenheimer-type approximation [Bor27] and remove the mode from the dynamics of the Hamiltonian. In this limit, the coupling with the mode B is linear and can be written as a displaced oscillator and a correction to the current,

$$\hat{\mathcal{H}}_B = \frac{\hat{P}_B^2}{2} + \frac{\omega_B^2}{2}\left(\hat{\Phi}_B + \frac{U_{22}\hat{I}_\alpha}{\sqrt{\tilde{\alpha}C_{\rm J}}\omega_B^2}\right)^2 - \frac{U_{22}^2\hat{I}_\alpha^2}{2\omega_B^2\tilde{\alpha}C_{\rm J}}. \tag{3.44}$$

Omitting the high-frequency oscillator mode and using a two-level approximation

for the qubit, the complete Hamiltonian becomes

$$\hat{\mathcal{H}}_{2L} = \hbar\omega_A \left(\hat{a}^\dagger \hat{a} + \frac{1}{2}\right) - \frac{\hbar\tilde{\Delta}_{\rm q}}{2}\hat{\sigma}_x - \frac{\hbar\tilde{\epsilon}}{2}\hat{\sigma}_z + \hbar g_A(\hat{a}_A + \hat{a}_A^\dagger)\hat{\sigma}_z. \tag{3.45}$$

In this last expression we have introduced the creation and annihilation operators, $\hat{a}_A^\dagger$ and $\hat{a}_A$, for mode A, the renormalized qubit gap $\tilde{\Delta}_{\rm q}$ and magnetic energy $\tilde{\epsilon}$ due to the last term in Eq. (3.44), and we have defined the coupling coefficient g_A that couples the qubit to mode A,

$$\hbar g_A \equiv U_{21} I_{\rm p} \sqrt{\frac{\hbar}{2\omega_A \tilde{\alpha} C_{\rm J}}}. \tag{3.46}$$

Using the explicit form of $U_{21} = \tilde{g}^2/N_-$ and $\tilde{g}^2 = \omega_{\rm R}/\sqrt{L_{\rm R}\tilde{\alpha}C_{\rm J}}$, we can obtain an expression similar to the one in Eq. (3.34),

$$\hbar g_A = \frac{I_{\rm p}}{N_-\tilde{\alpha}C_{\rm J}}\sqrt{\frac{\hbar\omega_{\rm R}^2}{2\omega_A L_{\rm R}}} = \frac{I_{\rm p}}{N_-\tilde{\alpha}C_{\rm J}}\sqrt{\frac{\omega_{\rm R}}{\omega_A}} I_{rms} = \xi_{R,A} I_{\rm p} \tilde{L} I_{rms}, \tag{3.47}$$

where we have defined $\tilde{L} \equiv (N_-\tilde{\alpha}C_{\rm J})^{-1}$, $I_{\rm rms} \equiv \sqrt{\hbar\omega_{\rm R}/(2L_{\rm R})}$ and $\xi_{R,A} \equiv \sqrt{\omega_{\rm R}/\omega_A}$.

To validate our derivation we study two limit cases: $L_{\rm c} \ll L_{\rm R}$, $\tilde{\alpha}C_{\rm J} \ll C_{\rm R}$. Let us start with $L_{\rm c} \ll L_{\rm R}$ to show $\tilde{L} \to L_{\rm c}$. For large values of $L_{\rm R}$, the effective inductance $L_{\rm eff} = L_{\rm c}L_{\rm R}/(L_{\rm c}+L_{\rm R})$ can be approximated as $L_{\rm eff} \simeq L_{\rm c}$. Similarly, we have $\omega_4 \gg \omega_{\rm r}$ and the difference between square frequencies becomes $\Omega^2 \simeq -1/(\tilde{\alpha}L_{\rm c}C_{\rm J})$. Using these results, we evaluate the term in Eq. (3.41)

$$\begin{aligned}\frac{\Omega^4}{4} + \tilde{g}^4 &= \frac{(\omega_{\rm R}^2 - \omega_4^2)^2}{4} + \frac{\omega_{\rm R}^2}{(L_{\rm R}\tilde{\alpha}C_{\rm J})^2} \underset{L_{\rm c}\ll L_{\rm R}}{\simeq} \frac{1}{4}\frac{1}{(\tilde{\alpha}C_{\rm J}L_{\rm c})^2} + \frac{\omega_{\rm R}^2}{(L_{\rm R}\tilde{\alpha}C_{\rm J})^2} \simeq \\ &\simeq \frac{1}{4}\frac{1}{(\tilde{\alpha}C_{\rm J}L_{\rm c})^2},\end{aligned} \tag{3.48}$$

which leads to $N_-^{-1} \simeq \tilde{\alpha}C_{\rm J}L_{\rm c}$, $\tilde{L} \simeq L_{\rm c}$ and $\xi_{R,A} \simeq 1$ for $L_{\rm c} \ll L_{\rm R}$. Therefore,

$$\hbar g_A \underset{L_{\rm c}\ll L_{\rm R}}{\longrightarrow} L_{\rm c} I_{\rm p} I_{\rm rms}. \tag{3.49}$$

The derivation of $\tilde{L}$ in the limit $\tilde{\alpha}C_{\rm J} \ll C_{\rm R}$ is similar to the previous one. For this case, $\Omega^2 \simeq -1/(\tilde{\alpha}L_{\rm eff}C_{\rm J})$ and $N_-^{-1} \simeq \tilde{\alpha}C_{\rm J}L_{\rm eff}$, leading to $\tilde{L} \simeq L_{\rm eff}$.

Therefore,

$$\hbar g_A \underset{\tilde{\alpha} C_\mathrm{J} \ll C_\mathrm{R}}{\longrightarrow} \xi_{R,A} \frac{L_\mathrm{c} L_\mathrm{R}}{L_\mathrm{R} + L_\mathrm{c}} I_\mathrm{p} I_\mathrm{rms}. \tag{3.50}$$

Comparison between coupling coefficient approximations

The validity of the approximations derived in the previous subsections is constrained by the values of L_c and g. In the first case, for $L_\mathrm{c} \simeq L_\mathrm{R}$, the resonator mode is modified by the presence of the coupling inductor and L_c has to be considered in the g derivation. Additionally, for large g, $\hat{\varphi}_4$ acquires dynamics and the Born-Oppenheimer approximation does not hold. In this section, we will compare the different methods for different values of L_c, considering the coupling coefficient calculated as:

- **Method A:** Evaluation of $\hbar g = I_\mathrm{p} I_\mathrm{rms} L_\mathrm{c} L_\mathrm{R} / (L_\mathrm{c} + L_\mathrm{R})$.
- **Method B:** Evaluation of $\hbar g = I_\mathrm{p} I_\mathrm{rms} L_\mathrm{c}$.
- **Method C:** Evaluation of $\hbar g_A = \xi_{R,A} I_\mathrm{p} \tilde{L} I_\mathrm{rms}$.

The approximate expressions have the same dependency on I_p and I_rms but differ in the inductance. To understand the behavior of the different methods, we can plot the respective effective inductance as a function of L_c. Figure 3.7 shows the comparative of L_c, $\tilde{L}$, $\xi_{R,A}\tilde{L}$ and $L_\mathrm{R} L_\mathrm{c}/(L_\mathrm{R} + L_\mathrm{c})$ for two different C_sh values. The difference between $\tilde{L}$ and $L_\mathrm{R} L_\mathrm{c}/(L_\mathrm{R} + L_\mathrm{c})$ is practically negligible, even for qubits with C_sh an order of magnitude larger. Therefore, the difference in behavior between methods comes from the term $\xi_{A,R}$ in Eq. (3.47) which compares the frequency of the bare resonator ω_R with the frequency of the normal mode A ω_A.

Table 3.2: Simulation parameters for a 3-junction flux qubit galvanically coupled to an LC oscillator. The coupling inductance L_c is left as a free parameter in the simulations.

A (μm^2)	α	S_c (fF/μm^2)	C_{sh} (fF)	L_R (nH)	C_R (fF)
0.0784	0.58	50	7.3	0.8976	742.3
0.0784	0.58	50	73.0	0.8976	742.3

3.4 Numerical diagonalization methods

The direct diagonalization of the Hamiltonian in Eq. (3.9) can be numerically costly. For couplings in the USC and DSC regimes ($g/\omega_\mathrm{R} > 0.1$) the qubit

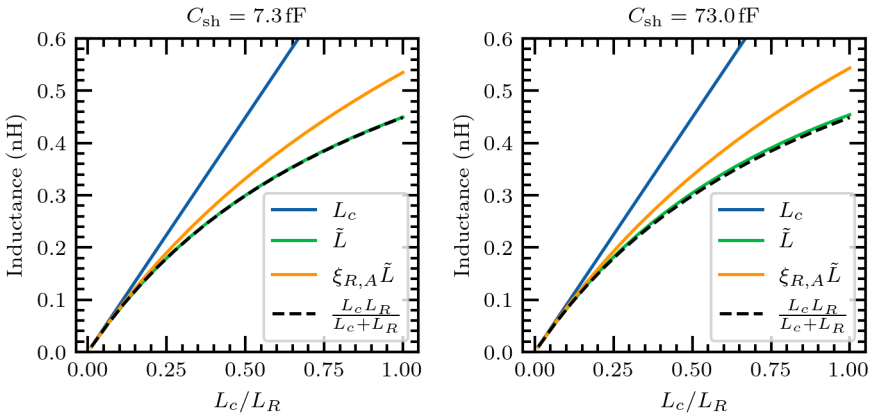

Figure 3.7: Scaling comparison of the effective inductance in the approximate expressions derived for the coupling coefficient. $\tilde{L}$ is calculated using the parameters listed in Table 3.2.

and resonator are highly hybridized and, in general, one needs to consider a significant amount of basis elements to obtain accurate enough solutions. On the other hand, the choice of basis and diagonalization method can directly impact the convergence and computation cost of the solution. In this section, we will present two methods to obtain the spectrum of a flux qubit galvanically coupled to an LC oscillator.

3.4.1 Standard method

The standard diagonalization method consists of writing the different operators of the Hamiltonian in Eq. (3.9) in the charge and harmonic oscillator bases. The choice is based on which elements of the Hamiltonian can be grouped in terms of LC-oscillators. For this particular system, we choose to write $\{\hat{\varphi}_6, \hat{n}_6\}$ and $\{\hat{\varphi}_4, \hat{n}_4\}$ in the harmonic oscillator basis. The rest of the operators will be mapped into the charge basis $\{|n\rangle\}$. The only difficulty of this approach is to express $e^{\pm i\hat{\varphi}_4}$ in the harmonic oscillator basis,

$$\begin{aligned}\langle\Psi_n(\hat{\varphi}_4)|e^{i\hat{\varphi}_4}|\Psi_k(\hat{\varphi}_4)\rangle &= \\ &= \frac{i^{n+k}e^{-\theta^2/4}}{\sqrt{2^{n+k}n!k!}}\left(\sum_{j=0}^{min(n,k)} 2^j j!\binom{n}{j}\binom{k}{j}(-1)^j\theta^{n+k-2j}\right)\end{aligned} \tag{3.51}$$

where $\theta = \sqrt{\frac{\hbar}{m\omega}}$. Except for this last term, all the other matrices will be sparse. Examples of this implementation for qubit and qubit-resonator systems can be found in [Lóp24].

3.4.2 Normal modes

Inspired by the work in [Smi+16] and the multiple usages of normal mode methods in fluxonium qubits, transmon qubit systems, and Josephson junction arrays [Pla20; Fra23; And+17; Nig+12], we developed a modified normal mode approach specific for a flux qubit galvanically coupled to an LC resonator. The method consists of linearizing the system, finding its normal modes, and finally using this basis to rewrite and diagonalize the complete Hamiltonian.

The main difference between the method used in [Smi+16] and approaches generally used in the Josephson junction array community (see for example [Fra23]) is the way in which the system is linearized. In the former, suitable for fluxonium qubits and other highly anharmonic qubits, the non-linear terms are entirely discarded ($E_\mathrm{J} \to 0$). The resulting linearized Lagrangian is used to obtain the normal modes. The second method, on the other hand, Taylor-expands the non-linear terms to second order to obtain the normal mode basis. With these differences in mind, we can now show the main challenges encountered when deriving the normal modes of a flux qubit galvanically coupled to an LC oscillator by any of the former methods.

Fluxonium approach

We start by the method in [Smi+16]. The main difference between our circuit (see Fig. 3.5) and the inductively shunted fluxonium is that in the latter, one can replace the Junction array by a linear inductor. This change introduces a term of the form $\varphi_q^2/2L$, where φ_q is the phase across the small junction. With this difference in mind, we can proceed to the derivation of the normal modes following what we will call from now on as the "fluxonium approach".

Consider Eq. (3.6). If we impose the linearization condition [$E_\mathrm{J} \to 0$], we obtain

$$\begin{aligned}\mathcal{L}_\mathrm{lin} = \frac{C_\mathrm{J}}{2}\left(\dot{\phi}_1^2 + \tilde{\alpha}(\dot{\phi}_4 - \dot{\phi}_1 - \dot{\phi}_3)^2 + \gamma\dot{\phi}_3^3 + \frac{C_\mathrm{R}}{C_\mathrm{J}}\dot{\phi}_6^2\right) + \\ + \frac{1}{2}\left(\frac{\phi_4^2}{L_\mathrm{c}} + \frac{(\phi_4+\phi_6)^2}{L_\mathrm{R}}\right).\end{aligned} \tag{3.52}$$

This system defines a generalized eigenvalue problem of the form,

$$[\mathbf{L}^{-1}]\vec{\varphi}_k = \omega_k^2[\mathbf{C}]\vec{\varphi}_k. \tag{3.53}$$

From the linearized Lagrangian, we can extract the capacitance and inductance matrices defining the problem,

$$[\mathbf{C}] = C_\mathrm{J}\begin{pmatrix} 1+\tilde{\alpha} & \tilde{\alpha} & -\tilde{\alpha} & 0 \\ \tilde{\alpha} & \gamma+\tilde{\alpha} & -\tilde{\alpha} & 0 \\ -\tilde{\alpha} & -\tilde{\alpha} & \tilde{\alpha} & 0 \\ 0 & 0 & 0 & C_\mathrm{R}/C_\mathrm{J} \end{pmatrix}, \tag{3.54}$$

$$[\mathbf{L}^{-1}] = \begin{pmatrix} 0 & 0 & 0 & 0 \\ 0 & 0 & 0 & 0 \\ 0 & 0 & 1/L_\mathrm{R}+1/L_\mathrm{c} & 1/L_\mathrm{R} \\ 0 & 0 & 1/L_\mathrm{R} & 1/L_\mathrm{R} \end{pmatrix}. \tag{3.55}$$

We note that the first entries of the inductance matrix are zero. If we try to solve the eigenvalue problem we will obtain at least two frequencies equal to zero. This result will become an obstacle when using Eq. (3.51) for the non-linear terms written in the normal-mode basis.

Junction array approach

We now consider what we will call the "junction array approach". The linearization of the system consists of expanding to second order the non-linear terms of the Hamiltonian in Eq. (3.9) around $\hat{\varphi}_i = 0$,

$$E_\mathrm{J}\cos\hat{\varphi}_1 \approx E_\mathrm{J} - \frac{E_\mathrm{J}}{2}\hat{\varphi}_1^2, \tag{3.56}$$

$$\gamma E_\mathrm{J}\cos\hat{\varphi}_3 \approx \gamma E_\mathrm{J} - \frac{\gamma E_\mathrm{J}}{2}\hat{\varphi}_3^2, \tag{3.57}$$

$$\begin{aligned} \alpha E_\mathrm{J}\cos(\hat{\varphi}_4 - \hat{\varphi}_1 - \hat{\varphi}_3 + 2\pi f) \approx{}& \alpha E_\mathrm{J}\cos(2\pi f) + \\ &- \alpha E_\mathrm{J}\sin(2\pi f)(\hat{\varphi}_4 - \hat{\varphi}_3 - \hat{\varphi}_1) + \\ &- \alpha E_\mathrm{J}\frac{1}{2}\cos(2\pi f)(\hat{\varphi}_4 - \hat{\varphi}_3 - \hat{\varphi}_1)^2, \end{aligned} \tag{3.58}$$

where we considered an arbitrary value of f in Eq. (3.58). Note that this expansion contains both linear and non-linear elements challenging to include in the Lagrangian formalism. From the first set of expansions, we obtain terms that go as $\hat{\varphi}_i^2$, which is what we missed in the fluxonium method.

Hybrid approach

The previous two approaches introduce some complexity when they are applied to the flux qubit - LC system. We propose the following hybrid method which solves the main obstacles:

1. Calculate the expansion up to second order of the $\cos\hat{\varphi}_i$ terms that do not contain the external flux.
2. Linearization of the system by considering the second order terms and by dropping the teerms containing the flux $\cos(\hat{\varphi}_i + 2\pi f)$.
3. Determination of the normal mode basis from the linearized system.
4. Reintroduce the nonlinearities. Make sure the quadratic terms from the $\cos\hat{\varphi}_i$ are compensated.
5. Solution to the full system in the normal mode basis.

We begin by expanding to second order the terms $\cos\hat{\varphi}_3$ and $\cos\hat{\varphi}_1$ and neglect the non-linear term $\alpha E_{\mathrm{J}}\cos(\hat{\varphi}_4 - \hat{\varphi}_1 - \hat{\varphi}_3 + 2\pi f)$, obtaining the linearized Hamiltonian,

$$\begin{aligned}\hat{\mathcal{H}}_{lin} = \frac{(2e)^2}{2C_{\mathrm{J}}}\left((\hat{n}_1+\hat{n}_4)^2 + \frac{1}{\gamma}(\hat{n}_3+\hat{n}_4)^2 + \frac{\hat{n}_4^2}{\tilde{\alpha}} + \frac{C_{\mathrm{J}}}{C_{\mathrm{R}}}\hat{n}_6^2\right) + \\ + \frac{1}{2}\left(\frac{\Phi_0}{2\pi}\right)^2\left(\frac{\hat{\varphi}_4^2}{L_{\mathrm{c}}} + \frac{(\hat{\varphi}_4+\hat{\varphi}_6)^2}{L_{\mathrm{R}}} + \frac{\hat{\varphi}_1^2}{L_J} + \gamma\frac{\hat{\varphi}_3^2}{L_J}\right).\end{aligned} \tag{3.59}$$

This Hamiltonian has the same structure as the following $\hat{\mathcal{H}}$:

$$\hat{\mathcal{H}} = \frac{(2e)^2}{2}\sum_{i,j=0}^{N}\hat{n}_i[C]^{-1}_{i,j}\hat{n}_j + \frac{\Phi_0^2}{2}\sum_{i,j=0}^{N}\hat{\varphi}_i[L^{-1}]_{i,j}\hat{\varphi}_j, \tag{3.60}$$

where we defined,

$$[\mathbf{C}] = C_{\mathrm{J}}\begin{pmatrix} 1+\tilde{\alpha} & \tilde{\alpha} & -\tilde{\alpha} & 0 \\ \tilde{\alpha} & \gamma+\tilde{\alpha} & -\tilde{\alpha} & 0 \\ -\tilde{\alpha} & -\tilde{\alpha} & \tilde{\alpha} & 0 \\ 0 & 0 & 0 & C_{\mathrm{R}}/C_{\mathrm{J}} \end{pmatrix} \tag{3.61}$$

$$[\mathbf{L}^{-1}] = \frac{1}{4\pi^2}\begin{pmatrix} 1 & 0 & 0 & 0 \\ 0 & 1 & 0 & 0 \\ 0 & 0 & 1/L_{\mathrm{R}}+1/L_{\mathrm{c}} & 1/L_{\mathrm{R}} \\ 0 & 0 & 1/L_{\mathrm{R}} & 1/L_{\mathrm{R}} \end{pmatrix}. \tag{3.62}$$

Note that the inductance matrix has entries different from zero for the first two variables. In principle, we should expect four non-zero eigenfrequencies (ω_k) and their associated eigenvectors as a solution to the generalized eigenvalue problem. These eigenfrequencies and eigenvectors will define the normal modes and normal mode frequencies of the linearized system. For this particular system we expect to have three modes associated to the qubit and one related to the resonator. The number of modes assigned to each element is related to their degrees of freedom. The linearized Hamiltonian can be written in terms of the creation and annihilation operators,

$$\hat{\mathcal{H}}_{lin} = \sum_k \hbar\omega_k \hat{a}_k^\dagger \hat{a}_k, \tag{3.63}$$

where the sum over k runs over the number of modes of the system.

Once the normal modes are known, it is time to write the full system Hamiltonian ($\hat{\mathcal{H}} = \hat{\mathcal{H}}_{lin} + \hat{\mathcal{H}}_{non-lin}$) in terms of this basis. We should be careful at this point and make sure to reintroduce the non-linear terms without duplicating elements (recall that we have expanded to second order two out of the three cos terms). The final Hamiltonian in the normal mode basis reads,

$$\begin{aligned}\hat{\mathcal{H}} = \hbar\sum_i \omega_i \hat{a}_i^\dagger \hat{a}_i - \frac{E_\mathrm{J}}{2}\left(\left(\sum_i s_{1i}\hat{\tilde{\varphi}}_i\right)^2 + \gamma\left(\sum_i s_{3i}\hat{\tilde{\varphi}}_i\right)^2\right) + \\ - E_\mathrm{J}\cos\left(\sum_i s_{1i}\hat{\tilde{\varphi}}_i\right) - E_\mathrm{J}\cos\left(\sum_i s_{2i}\hat{\tilde{\varphi}}_i\right) + \\ - E_\mathrm{J}\cos\left(\sum_i s_{4i}\hat{\tilde{\varphi}}_i - \sum_i s_{1i}\hat{\tilde{\varphi}}_i - \sum_i s_{3i}\hat{\tilde{\varphi}}_i + 2\pi f\right)\end{aligned} \tag{3.64}$$

where the capacitance matrix in the normal mode basis takes the identity form and the diagonal elements of the inductance matrix are given by the eigenvalues of the linearized system. The prefactors s_{ij} are the entries of the change of basis matrix containing the eigenvectors as columns.

3.4.3 Comparison between diagonalization methods

In Figs. 3.8 and 3.9 we compare the third excited state convergence of the system for different points of flux. We take the energy obtained with n basis elements and compare it with the one obtained using $n-1$ basis elements. The difference between energies should tend zero for a large enough number of basis elements. In both cases, we increase all subspaces related to the same basis at the same time. For example, if we set $n_{charge} = 5$, we will use this number of basis elements to

write $\hat{\varphi}_1$ and $\hat{\varphi}_3$. The circuit parameters used for the simulation are listed in Table 3.3.

Table 3.3: Simulation parameters for a 3-junction flux qubit galvanically coupled to an LC oscillator. The resulting energies for these set of parameters are $E_C/h = 4.9\,\text{GHz}$ and $E_J/h = 93.5\,\text{GHz}$.

J_c (μA/μm^2)	A (μm^2)	α	S_c (fF/μm^2)	C_{sh} (fF)	L_c (nH)	β_l	L_R (nH)	C_R (fF)
2.4	0.0784	0.58	50	7.3	0.5	0.29	0.8976	742.3

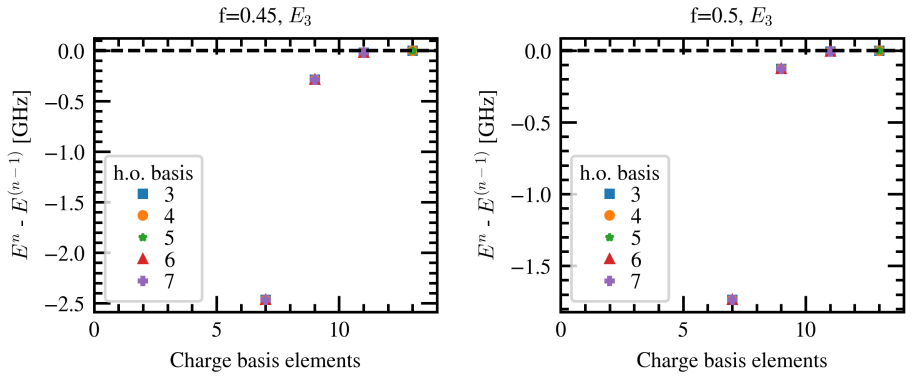

Figure 3.8: Convergence of the third excited state energy obtained using the standard method derived in Sec. 3.4.1 as a function of the number of charge basis elements used in the simulation. The legend indicates the number of harmonic oscillator (h.o.) basis elements used for each color/shape. The left panel shows the convergence at flux $f = 0.45$. The right pannel is calculated at $f = 0.5$.

We note that the normal mode-method needs, in general, more basis elements to converge to the solution. $n_{\text{qubit}} \sim 10$ and $n_{\text{LC}} \sim 5$ seem enough to reach convergence in the simulations shown in Fig. 3.9. This leads to a total matrix dimension of ~ 5000. Following the standard method, it seems enough to use $n_{\text{charge}} \sim 11$ and $n_{\text{ho}} \sim 3$, leading to a total matrix dimension of $d \sim 1089$. Although both results are approximately on the same order of magnitude, the computational cost to solve the system in the normal mode basis is much larger. The matrices used for this approach are not sparse, thus, the memory usage and the computational time is significantly increased. To give an order of magnitude we can compare a normal mode simulation performed with $n_{\text{qubit}} = 10$ and $n_{\text{LC}} = 6$ with a standard simulation performed with $n_{\text{charge}} = 15$ and $n_{\text{ho}} = 5$. The first case takes about $\sim 1\,\text{min}$ per flux point on a laptop with *AMD Ryzen 7 pro*, while the standard simulation is able to return a point in $\sim 20\,\text{s}$.

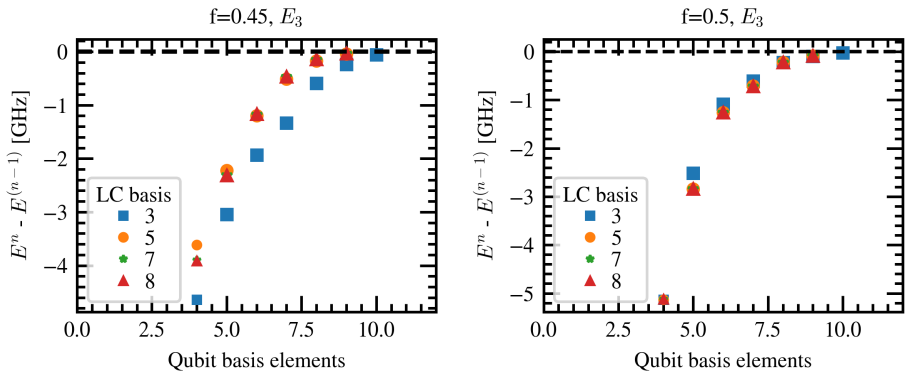

Figure 3.9: Convergence of the third excited state energy obtained using the normal mode method as a function of the number of qubit basis elements used in the simulation. The legend indicates the number of LC oscillator basis elements used for each color/shape. The left panel shows the convergence at flux $f = 0.45$ and the right one at $f = 0.5$.

The difference in the converge of normal modes is more pronounced when the change of basis elements is performed in the qubit basis rather than in the LC resonator basis for the qubit and resonator parameters used for this study. The slow convergence could be explained by the initial truncation of the $\cos\hat{\varphi}_1$ and $\cos\hat{\varphi}_3$ terms. In the standard method, these terms are easily mapped to the charge basis which could explain the faster convergence.

The results presented in Fig. 3.9 are parameter-dependent. Setting a very small capacitance value on one of the capacitance matrix entries may result in a more difficult numerical calculation of the normal modes basis of the system. In fact, it can even lead to numerical errors and the solution might not converge at all. Similarly, systems with significantly larger/smaller values of beta may not allow rewriting the final solution in terms of the normal-mode basis. In the latter, small entries on the change of basis matrix can also lead to numerical errors in the final solution. Therefore, systems where the magnitude of the different parameters are orders of magnitude apart might not be suited for the normal-mode approach.

Even though the convergence in the normal mode method may be slower than direct diagonalization, this method provides a set of tools to understand the coupled system from another perspective. For example, the initial calculation of the normal mode basis already provides an idea of the renormalized frequency of the resonator. This renormalization is not obvious when looking into the complete Hamiltonian of the system (see Eq. (3.9)) given that there are no terms

with $\sim \hat{\varphi}_6^2/L_c$. Knowing beforehand the value of the renormalized resonator frequency is helpful when choosing the number of basis elements used to describe the resonator in the normal mode simulation. In fact, for flux values far from the sweetspot, where the qubit-resonator transverse coupling $\hat{\sigma}_x(\hat{a}+\hat{a}^\dagger)$ goes to zero, the system decouples and we recover the renormalized resonator transitions. We can compare the resulting transitions far from the sweetspot with the renormalized frequency obtained via normal mode analysis. If there is a difference, then it means that more resonator basis elements are needed in the simulation. On the other hand, as proposed in [Smi+16], one can set the interaction to zero by fixing the resonator normal mode variable $\hat{\varphi}_R \to 0$ in the non-linear terms of Eq. (3.64). The diagonalization of the non-interacting Hamiltonian provides an idea of the quantum numbers associated to each transition of the complete system. Identifying the components of each transition is particularly useful at the time of analyzing the experimental spectrum of the qubit-resonator system.

3.5 Electric dipole moment and emission rate of a flux qubit capacitively coupled to an open waveguide

As it will be shown in Ch. 4, one of the key design elements of the experiment is the addition of a second feedline to directly probe the qubit. This feedline couples capacitively to the qubit C_{sh}. However, the capacitance of this coupling cannot be arbitrary. If it is designed too large, the qubit will be strongly coupled and the emission to the line will be the dominant decoherence channel. On the other hand, if the coupling is made too small no signal will reach the qubit. One way to quantify the appropriate coupling is by deriving the emission rate to the feedline, Γ_1.

Following the lines of [Ant+20] one can estimate the photon emission rate of a qubit coupled capacitively to a transmission line using the relationship,

$$\Gamma_1 = \frac{(d_{01}C_c)^2\omega Z_0}{\hbar}, \tag{3.65}$$

where Z_0 is the impedance of the line, C_c is the coupling capacitance to the line and d_{01} is the transition matrix element defined as $d_{ij} \equiv \langle j|\hat{V}_k|i\rangle$. The physical meaning of d_{ij} is the induced potential on island k due to atomic transitions, or in other words, the electric dipole transition matrix element.

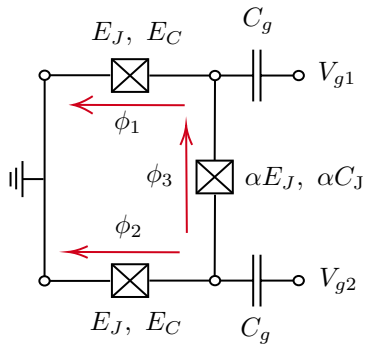

Figure 3.10: Circuit for a 3-junction flux qubit considering an arbitrary gate voltage at nodes 1 and 2.

The voltage operator $\hat{V}_k$ is defined as,

$$\hat{V}_k \equiv \frac{1}{2e}\frac{\partial \hat{\mathcal{H}}}{\partial n_k}, \tag{3.66}$$

with $\hat{\mathcal{H}}$ the Hamiltonian of the system and n_k the k-th charge operator.

The circuit considered for this derivation is shown in Fig. 3.10, consisting of a 3-junction flux qubit with a voltage source on each of the nodes of the circuit. The Hamiltonian for such a system [Orl+99] is given by,

$$\begin{aligned}\hat{\mathcal{H}} =&(\hat{n}_i - \hat{n}_{gi})4(E_c)_{ij}(\hat{n}_j - \hat{n}_{gj}) - E_\mathrm{J}\cos\hat{\varphi}_1 - E_\mathrm{J}\cos\hat{\varphi}_2 + \\ &- \alpha E_\mathrm{J}\cos\left(2\pi f + \hat{\varphi}_1 - \hat{\varphi}_2\right)\end{aligned} \tag{3.67}$$

with $i, j \in \{1, 2\}$ and $(E_c)_{ij}$ the entries of the matrix $E_c = \frac{e^2}{2}C^{-1}$ where C is the capacitance matrix,

$$C = \begin{pmatrix} C_{J1} + C_{g1} + C_{J3} & -C_{J3} \\ -C_{J3} & C_{J2} + C_{g2} + C_{J3} \end{pmatrix}. \tag{3.68}$$

Following again the lines of the Supplementary in [Ant+20], we can express the voltage on the different islands as,

$$\begin{aligned}\begin{pmatrix}\hat{V}_1 \\ \hat{V}_2\end{pmatrix} &= C^{-1}\hat{\vec{q}} = C^{-1}2e\hat{\vec{n}} = \\ &= \frac{2e}{\det C}\begin{pmatrix} C_{J2} + C_{g2} + C_{J3} & C_{J3} \\ C_{J3} & C_{J1} + C_{g1} + C_{J3}\end{pmatrix}\begin{pmatrix}\hat{n}_1 \\ \hat{n}_2\end{pmatrix}.\end{aligned} \tag{3.69}$$

This leads to an expression for V_2 in terms of the $\hat{n}_1$ and $\hat{n}_2$ operators,

$$\hat{V}_2 = \frac{2e\left[C_{J3}\hat{n}_1 + (C_{J1} + C_{g1} + C_{J3})\hat{n}_2\right]}{(C_{J1} + C_{g1} + C_{J3})(C_{J2} + C_{g2} + C_{J3}) - C_{J3}^2}. \tag{3.70}$$

Once we know the expression for $\hat{V}_2$, we can calculate $d_{01} = \langle 0|\hat{V}_2|1\rangle$,

$$d_{01} = \frac{2e[C_{J3}\langle 0|\hat{n}_1 \otimes \mathbf{I}_2|1\rangle + (C_{J1} + C_{g1} + C_{J3})\langle 0|\mathbf{I}_1 \otimes \hat{n}_2|1\rangle]}{(C_{J1} + C_{g1} + C_{J3})(C_{J2} + C_{g2} + C_{J3}) - C_{J3}^2}. \tag{3.71}$$

Note that this result is equivalent to the one obtained by performing the partial derivative with respect to n_2 in Eq. (3.66).

In the following section, we show how to obtain d_{01} using the Python package *Scqubits* [Gro+21; Chi+22].

3.5.1 *Scqubits* to estimate the electric dipole moment

Dipole matrix elements d_{ij} can be easily calculated using the Python package *scqubits* [Gro+21; Chi+22]. The package has a 3-junction flux qubit class which can return the numerical form of the operators $\hat{n}_k$ as well as the eigenstates and eigenvalues of the system. We provide a detailed implementation in the GitHub repository [Tor25].

In the left panel of Fig. 3.11 we show an example of the transition matrix elements as a function of the external flux Φ_{ext} for the set of parameters listed in Table 3.4. Note that d_{02} vanishes at the sweetspot indicating a forbidden transition due to the parity of the wave functions of states 0, 2 in the symmetric potential.

Table 3.4: Design parameters for a 3-junction flux qubit with resulting energies $E_{\text{C}}/h = 4.9\,\text{GHz}$ and $E_{\text{J}}/h = 93.5\,\text{GHz}$ for the big junctions. J_{c} is the Josephson critical current density, S_C the Josephson junction capacitance density, A is the area of the junctions, C_{sh} the shunt capacitor for the small junction, Δ_{q} is the qubit gap and finally, I_{p} is the persistent current of the qubit.

J_{c} (μA/μm^2)	A (μm^2)	α	S_c (fF/μm^2)	C_{sh} (fF)	C_c (fF)	Δ_{q}/h (GHz)	I_{p} (nA)
2.4	0.0784	0.58	50	7.3	0.447	5.57	67.9

We can also study the change in dipole moment when sweeping the charge in island 2 (see Fig. 3.12) while the qubit is at the sweetspot. We observe periodic oscillations for both d_{ij} and the spectrum. Figure 3.12 panels (d), (e) and (f) show a zoom into the different oscillations. We can see that for the transition matrix d_{01} (panel (d)) the amplitude of the oscillations is roughly $\sim 0.02\,\mu\text{V}$. In

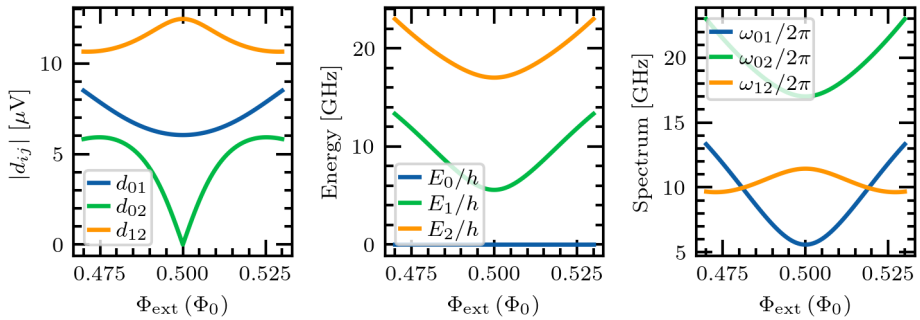

Figure 3.11: Dipole moment and qubit spectrum simulations of a 3JJ flux qubit obtained from the design parameters listed in Table 3.4 as a function of the external flux Φ_{ext}. Left panel: simulated transition matrix elements. Central panel: energy levels of the qubit. Right panel: spectrum of the qubit.

the spectrum case (panel (f)) the amplitude of the oscillations is $\sim 5\,\text{MHz}$. This amplitude gives an idea on how the spectrum of the system will be affected by charge fluctuations. If we increase $C_{\text{sh}} = 36.5\,\text{fF}$ while keeping the rest of the parameters in Table 3.4, the oscillations of the spectrum versus charge decrease by almost two orders of magnitude, with a value of $\sim 60\,\text{kHz}$. This is relevant to minimize the charge noise at the sweetspot.

In Fig. 3.13 we calculate Γ_1 at the qubit sweetspot for several coupling capacitance values while keeping the rest of the parameters from Table 3.4. We observe a rapid decrease of T_1 with increasing coupling capacitance, as expected from Eq (3.65). Generally, we want to maintain a tradeoff between the maximum T_1 and the capacitance to the line. For the set of parameters presented in Table 3.4 (design A) one should target values of C_c between 0.2 fF and 0.45 fF, yielding $T_1 \gtrsim 10\,\mu\text{s}$. Possible ways to engineer higher T_1 in this configuration include increasing C_{sh} and decreasing the qubit gap Δ_{q}. An increase of C_{sh} reduces d_{01} without having to modify the areas of the qubit junctions and decreasing the qubit gap has a direct impact in Γ_1 given by Eq. (3.65). By designing a C_{sh} capacitor with five times more capacitance than the qubit presented in Table 3.4, we can increase the T_1 by almost two orders of magnitude. The change in C_{sh} also implies a reduction in the qubit gap.

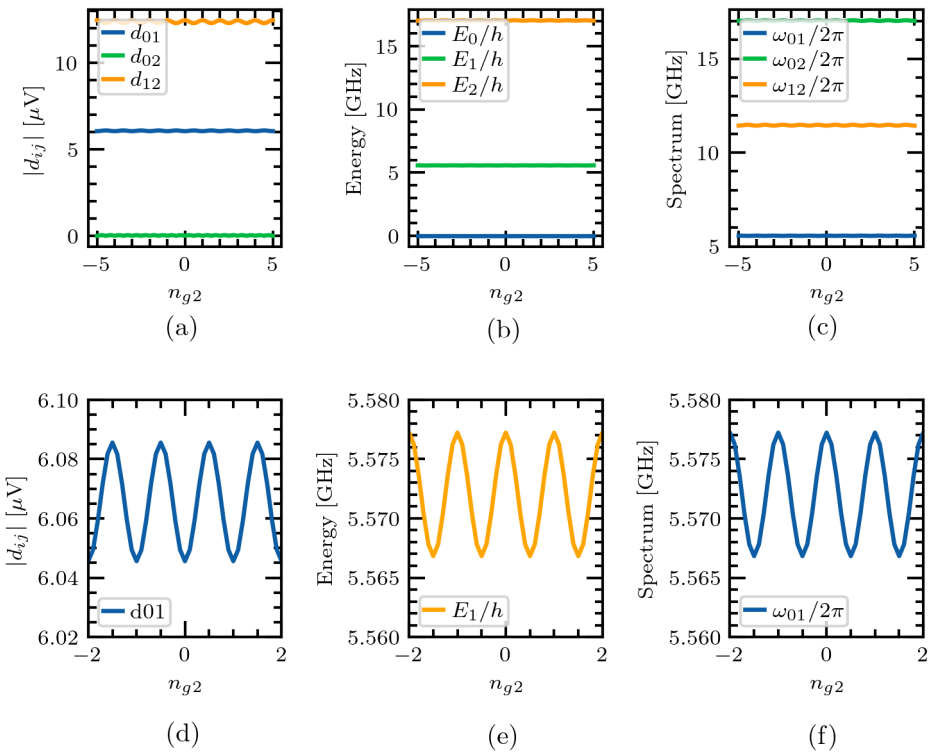

Figure 3.12: Dipole moment and qubit spectrum simulations obtained from the design parameters listed in Table 3.4 at $f = 0.5$ as a function of the charge in island 2 (n_{g2}). Panel (a) shows the simulated transition matrix elements, (b) presents the simulated energies of the system and (c) the resulting spectrum. Panels (d), (e) and (f) are a zoom into the panels (a), (b) and (c) respectively.

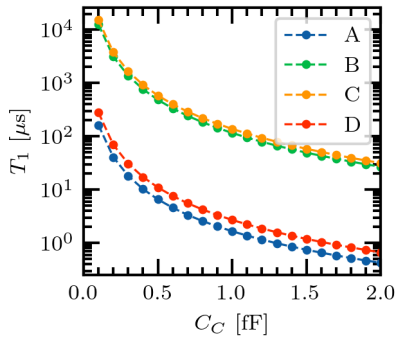

Figure 3.13: Simulated $T_1 = \Gamma^{-1}$ at the sweetspot ($f = 0.5$) obtained using Eq. (3.65) as a function of the coupling capacitance C_c for different qubit designs. The different qubits use the parameters listed in Table 3.4 with variations in C_{sh} and J_{C}. Qubit A is simulated with the parameters listed in Table 3.4, qubit B uses $C_{\mathrm{sh}} = 36.5\,\mathrm{fF}$ and $J_{\mathrm{c}} = 2.4\,\mu\mathrm{A}/\mu\mathrm{m}^2$, qubit C uses $C_{\mathrm{sh}} = 36.5\,\mathrm{fF}$ and $J_{\mathrm{c}} = 1\,\mu\mathrm{A}/\mu\mathrm{m}^2$ and finally qubit D uses $C_{\mathrm{sh}} = 7.3\,\mathrm{fF}$ and $J_{\mathrm{c}} = 1\,\mu\mathrm{A}/\mu\mathrm{m}^2$.

Chapter 4

Superinductive ultrastrong couplings: Experiments

Alba Torras-Coloma, Luca Cozzolino, Ariadna Gómez-del-Pulgar-Martínez, Elia Bertoldo and P. Forn-Díaz

Contents

In this chapter, we present the design and measurements of a 3-junction flux qubit galvanically coupled to an LC oscillator, as introduced in Ch. 3. The circuit design has two distinctive features. First, we use a superinductor material as a shared coupling element between the flux qubit and the resonator and, secondly, we include two feedlines into the design to independently probe the system through either the qubit or the resonator.

The experimental data shown in this chapter corresponds to a sample with significantly off-target parameters, but still, in an interesting regime. In particular, the fits to the Quantum Rabi model reveal that despite the low persistent current of the qubit, the qubit-resonator coupling is in the perturbative USC regime. The results validate the use of superinductors as an approach to reach

ultrastrong galvanic couplings while keeping qubit parameters in a range compatible with long coherences [Tor+25]. In addition, the experiment serves as a proof of concept for studies in the USC regime with multiple probing lines. The incorporation of superinductors in qubit circuits opens the door to new USC designs and studies using low persistent current qubits, hence higher coherence, and large superinductive galvanic couplings.

4.1 Design of a qubit-resonator system in the ultrastrong coupling regime

In Ch. 3, we have presented the electrical circuit and the Hamiltonian to study a flux qubit galvanically coupled to an LC oscillator in the USC regime. In this section, we present the design parameters and design layout used to implement the experiment.

Before diving into the design, we can give some insights on how to reach the USC regime with flux qubits and resonators. Recall the approximate expression for the coupling coefficient derived in Section 3.3.3 in the limit $\tilde{\alpha}C_J \ll C_R$,

$$g \simeq \xi_{R,A}\frac{L_\mathrm{c}L_R}{L_\mathrm{c}+L_R}\frac{I_\mathrm{p}I_\mathrm{rms}}{\hbar} = \xi_{R,A}\frac{L_\mathrm{c}L_R}{L_\mathrm{c}+L_R}\frac{I_\mathrm{p}}{\hbar Z_R}\sqrt{\frac{\hbar\omega_R}{2C_R}}, \tag{4.1}$$

where $\xi_{R,A} = \sqrt{\omega_R/\omega_A}$ with ω_A the lowest normal mode frequency of the coupled harmonic system and $\omega_R = 1/\sqrt{L_\mathrm{R}C_\mathrm{R}}$ the frequency of the bare LC resonator[1].

In order to increase the coupling we should target low-impedance resonators, large persistent current qubits and large coupling inductors. The first two require adjusting the parameters of the resonator and the qubit. However, designing large and linear inductors is not simple. Most of the literature concerning flux qubits galvanically coupled to resonators or waveguides in the USC regime used Josephson junctions as couplers [Nie+10; For+17; Yos+17b; Yos+17a]. Junctions have the advantage that they can provide a large inductance in a small space and they are relatively easy to fabricate and include in qubit designs. Although Josephson junctions are simple to fabricate, errors in the area and critical current can lead to inaccurate inductance values of up to a ±10%. Junctions also present a number of technical complications. They introduce stray nonlinearities which impacts the device functionality, while adding junction losses coming from quasiparticle tunneling [Ris+13] and two-level system defects [Bil+17]. Other studies

[1]Throughout this chapter we will use $\omega_R = 1/\sqrt{L_\mathrm{R}C_\mathrm{R}}$ to refer to the bare LC resonator, ω_A for the renormalized resonator frequency obtained with Eq. (3.39) which includes the effect of L_c and the capacitance of the α junction, and finally, ω_r to describe the resonator mode in the QRM without approximations.

proposed the use of shared thin Al wires to reach ultrastrong couplings [For+10]. However, reaching coupling strengths beyond the perturbative USC regime requires significantly long and narrow Al wires which can be challenging from a fabrication point of view. Alternatively, one would require loop lengths of tens or hundreds of microns, leading to an enhancement of flux noise.

The alternative explored in this thesis are superinductor materials. Superinductor materials are disordered superconductors that can reach characteristic impedances of the order of the resistance quantum $R_Q \sim 6.5\,\mathrm{k\Omega}$ [Man12] which essentially translates in large surface kinetic inductance. The advantage of these materials compared to junctions is their small nonlinearity combined with low microwave losses.

For our design we choose granular Aluminum (grAl) as the desired superinductor material. GrAl allows us to design inductances of the order of nH in relatively small spaces [Grü+18; Zha+19]. Furthermore, it is relatively easy to implement in Al-based fabrication processes [Grü+19]. The second distinctive element of this work consists of two individual feedlines on chip: one coupling to the qubit and the other one to the resonator. Fig. 4.1 presents the final circuit design as a guide for the reader. The top feedline couples to the capacitive part of the lumped element resonator. A flux bias line (FBL) controls the flux qubit. At the the bottom of the image, the qubit feedline couples to the qubit shunt capacitor. In the upcoming subsections we provide the design details for each element on the chip.

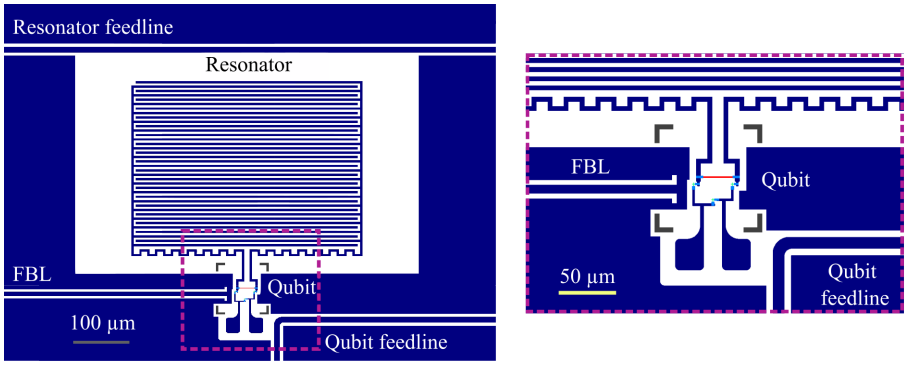

Figure 4.1: Device layout consisting on a three-junction flux qubit galvanically coupled to an LC lumped-element resonator with two feedlines and a flux-bias line (FBL). The panel on the right provides a zoomed in image of the qubit region.

4.1.1 Resonator design

We employ a lumped-element LC resonator for this experiment, which is a circuit smaller in length than the electromagnetic wavelength, where the current and voltage do not significantly vary over the dimensions of the inductor and capacitor, respectively. Therefore, lumped-element resonators display a single resonance mode [Poz21]. This is particularly relevant in our experiment where we want to couple only one electromagnetic mode to the qubit.

To simulate the resonator we use the 3D-planar high-frequency electromagnetic simulation software *Sonnet*[2]. A typical simulation layout of the LC resonator is shown in Fig. 4.2 with the circuit simulation parameters given in Table 4.1. Since our devices will be fabricated with 50 nm of Al we need to consider the kinetic contribution to the inductance by adding a sheet inductance of $L_\mathrm{s} = 0.4\,\mathrm{pH}/\square$ [Lóp+25] into the simulations. The capacitance (C_R) and total inductance ($L_\mathrm{R} = L_\mathrm{geo} + L_\mathrm{kin}$) of the resonator are estimated using the method described in [Doy+08; Lóp24], where a square of metal with sheet inductance L'_s is added into the resonator layout. This sheet inductance modifies the resonance by $\omega'_R = \frac{1}{\sqrt{(L'_\mathrm{s}+L_\mathrm{R})C_\mathrm{R}}}$. The values for L_R and C_R are extracted comparing ω'_R with $\omega_\mathrm{R} = \frac{1}{\sqrt{L_R C_R}}$.

Table 4.1: Sonnet resonator simulation parameters. We consider a general metal model with sheet inductance L_s estimated for 50 nm Al using the data in [Lóp+25]. The substrate is intrinsic silicon with t the thickness, $\tan\delta$ the dielectric loss tangent, σ the conductivity, ϵ_r the relative electric permitivity and μ_r the relative magnetic permeability.

Metal model	L_s (pH/□)	Si t (μm)	ϵ_r	$\tan\delta$	μ_r	σ (S/m)
General (lossless)	0.4	500	11.45	5e-5	1	0

In general, we want the resonances of our complete system to fall in the range 4 GHz and 8 GHz, which is imposed by the microwave components of our setup (see Sec. 2.2). For example, the low-temperature amplifier works best in the $4-8$GHz bandwidth and the low-pass filters have a cutoff frequency of 8 GHz. We target a resonator resonance frequency around 6 GHz which is considerably above 4 GHz. As shown in Sec. 3.3, we have to take into account that the coupling will renormalize the resonance frequency of the resonator to ω_A given by Eq. (3.39). The resulting capacitor geometry consists of 38 fingers of width 4 µm spaced 4 µm. This provides an estimated capacitance of $C_\mathrm{R} \simeq 0.74\,\mathrm{pF}$. The inductor is designed with a total of 28 legs of width 4 µm and length 4 µm. Two central legs are designed longer to accommodate the qubit.

[2] https://www.sonnetsoftware.com/

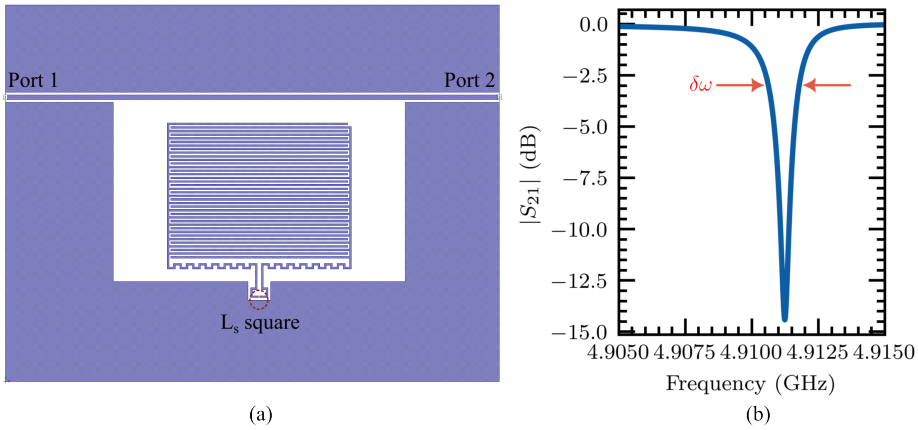

(a) (b)

Figure 4.2: (a) Snapshot of a *Sonnet* simulation layout. The ends of the feedline contain the two different ports of the simulation, and the center of the long leg inductor contains an extra sheet inductance L_s to emulate the coupling inductor to the qubit. (b) Example of a resonance obtained setting $L_s = L_c = 0.5\,\text{nH}$ with $Q_L = 5 \times 10^3$ and $\delta\omega = 1\,\text{MHz}$.

The estimated resonator inductance from simulations is $L_R = 0.90\,\text{nH}$. Note that this value contains the sheet kinetic inductance of the Al [Lóp+25]. Considering the simulated inductance and capacitance, the resonator frequency is estimated to be $\omega_R/2\pi = (2\pi\sqrt{L_R C_R})^{-1} = 6.2\,\text{GHz}$. Note that ω_R is obtained without considering the effect of L_c and the total capacitance of the small qubit junction.

Recall that in the complete circuit design, the resonator will couple to the qubit through a shared inductance L_c. As we show in Sec. 4.1.2, a coupling inductor $L_c = 0.5\,\text{nH}$ is enough to bring the qubit-resonator system in the non-perturbative USC regime. If we take into account $L_c = 0.5\,\text{nH}$ into the resonator, the resonance is modified to $\omega_A/2\pi = 4.9\,\text{GHz}$. The renormalized resonator frequency ω_A is still above 4 GHz as we initially intended.

Coupling to the feedline

Another important parameter to consider is the resonator loaded quality factor, defined as

$$\frac{1}{Q_L} = \frac{1}{Q_{ext}} + \frac{1}{Q_{int}}, \tag{4.2}$$

where Q_{int} is the internal quality factor and Q_{ext} is the external quality factor. Q_L gives an idea of the losses of the system, and whether they are limited by the

coupling to the external circuitry (Q_{ext}) or by internal loss mechanisms (Q_{int}).

The internal quality factor can be estimated from the dielectric loss tangent of silicon at low temperatures, by $1/Q_{\text{int}} \approx \tan\delta$. Using literature values [Kru+06; Che+22] it is safe to assume a value of $Q_{\text{int}} = \frac{1}{\tan\delta} = \frac{1}{5\times10^{-5}} > 2\times10^4$, as used in Table 4.1 for our resonators. On the other hand, the external quality factor will be given by the coupling to the feedline. We estimate Q_{L} using the resulting S_{21} curve from *Sonnet* simulations and the width $\delta\omega$ at $-3\,\text{dB}$ of the resonance. Considering $L_{\text{c}} = 0.5\,\text{nH}$ in the resonator simulation and a distance of $52\,\mu\text{m}$ to the feedline, we obtain $Q_{\text{L}} \approx 5000$ while keeping a narrow enough bandwidth of $\delta\omega_{\text{r}} \simeq 1\,\text{MHz}$, and $Q_{\text{ext}} \approx 6500 \ll Q_{\text{int}}$. We expect the resonator to be overcoupled, as is usual in circuit QED readout resonators, while keeping an expected lifetime of $\tau = Q_L/\omega_A = 0.2\,\mu\text{s}$ compatible with a long enough coherence for this experiment.

4.1.2 Qubit design

We consider a 3-junction flux qubit where one of the junctions is an α factor smaller than the other two. Since the qubit will be coupled to the resonator by a shared inductor, we add L_{c} into the qubit simulations. A set of requirements that need to be fulfilled by the qubit in order to carry out this experiment:

- The flux qubit has to be in the double-well potential regime.
- The qubit gap ($\Delta_{\text{q}}/2\pi\hbar$) has to be close to $4\,\text{GHz}$
- The qubit should have a considerably large persistent current ($I_{\text{p}} > 50\,\text{nA}$). However, flux qubits with large persistent currents are more sensitive to flux noise [Yan+16]. Thus, we want to keep I_{p} on the lower side to maintain a compromise between qubit coherence and qubit-resonator coupling.

Besides these requirements, fabrication imposes a set of limitations. The area of the junctions will be mostly limited by the double-stack resist and evaporation angles presented in Ch. 2. We can fabricate junction areas (A) approximately between $0.03\,\mu\text{m}^2$ and $0.09\,\mu\text{m}^2$. On the other hand, the critical current density (J_{c}) will be limited by the area and the calibration of the junction oxidation. For our designs, we will target values of J_{c} between $2.0\,\mu\text{A}/\mu\text{m}^2$ and $3.0\,\mu\text{A}/\mu\text{m}^2$.

We can use Eq. (4.1) to give us an idea of the qubit parameters needed to reach the USC regime. Using the resonator designed in Sec. 4.1.1, by fixing the coupling inductance to $L_{\text{c}} = 0.5\,\text{nH}$ and the qubit persistent current to $I_{\text{p}} \approx 55 - 65\,\text{nA}$, we reach the non-perturbative USC regime. Performing a parameter sweep in the simulations, we obtain the qubit parameters listed in Table 4.2 fulfilling the set of requirements. The estimated persistent current for this qubit design is $I_{\text{p}} = 72.4\,\text{nA}$, with the calculated energies $E_J/h = 93.5\,\text{GHz}$ and $E_C/h = 4.9\,\text{GHz}$

for the large qubit junctions. The ratio of energies designed $E_J/E_C \gg 1$, ensures a low charge sensitivity. The resulting energies and spectrum for the qubit are shown in Fig. 4.3.

Table 4.2: Qubit design parameters. J_c and S_c are the current density and capacitance density of the junction, A is the area of the big junction, α gives the ratio in areas between the small and big junctions, C_{sh} is the shunt capacitor of the small junction, L_c is the coupling inductance and Δ_q is the qubit gap. S_c is estimated, the other parameters are simulated or directly measured.

J_c (μA/μm^2)	S_C (fF/μm^2)	A (μm^2)	α	C_{sh} (fF)	L_c (nH)	Δ_q/h (GHz)
2.4	50	0.0784	0.58	7.3	0.5	3.6

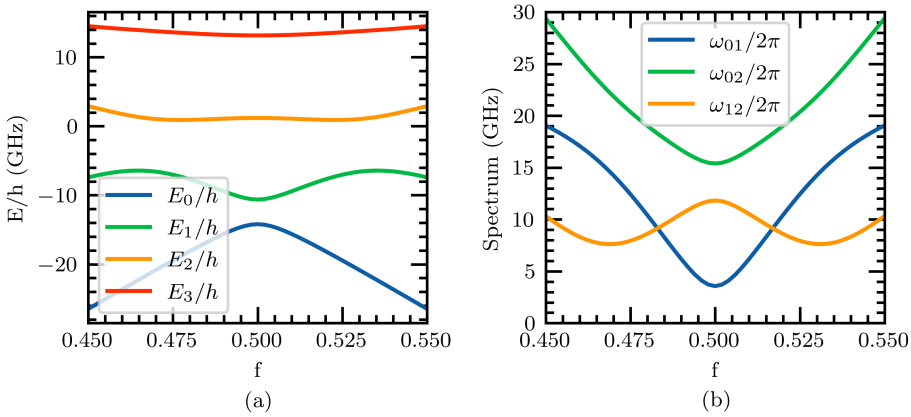

Figure 4.3: (a) Energies and (b) spectrum for the designed 3JJ qubit with L_c as a function of the external flux $f = \Phi_{\text{ext}}/\Phi_0$. The design parameters are listed in Table 4.2. The energies and spectrum are obtained by adapting the standard diagonalization method (see Sec. 3.4.1) to the Hamiltonian in Eq. (3.1).

Capacitance design

In this experiment the circuit contains two transmission lines to probe the qubit or the resonator independently. Since the space around the qubit is limited, we couple the qubit capacitively to the feedline using the shunt capacitor C_{sh} pads (see the bottom line in Fig. 4.1). In order not to limit excessively the coherence of our qubit, and at the same time obtain enough signal, we target a coupling capacitance to the line of $C_c = 0.4\,\text{fF}$. Using the approach derived in Sec. 3.5.1,

we estimate $T_1 \approx 10\,\mu s$ which is significantly low for the standards of flux qubits [Yan+16]. It would be possible increase T_1 by considering larger C_{sh} capacitors or reducing further C_c. However, an increase in C_{sh} normally implies reducing the qubit gap which would bring the qubit away from the resonator frequency. Overall, obtaining the ideal set of qubit parameters leads to a tradeoff between resonance condition, signal amplitude and qubit coherence.

The C_{sh} and the capacitance to the line C_c are estimated using the finite element simulation software *COMSOL Multiphysics*[3]. To extract the final capacitance of the different circuit elements, we perform a similar capacitance network analysis to the one described in [Lóp24]. We iterate this process by changing the dimensions and shapes of the capacitors until the obtained capacitance from *COMSOL* and the network analysis matches the value set on the qubit numerical simulations. For this particular case, the qubit capacitor pads are desigend to be $25\,\mu m \times 27\,\mu m$ spaced $16\,\mu m$. The distance from the edge of the capacitor to the central conductor of the feedline is set to $d_{Qf} = 19.5\,\mu m$ (see the schematics in Fig. 4.4).

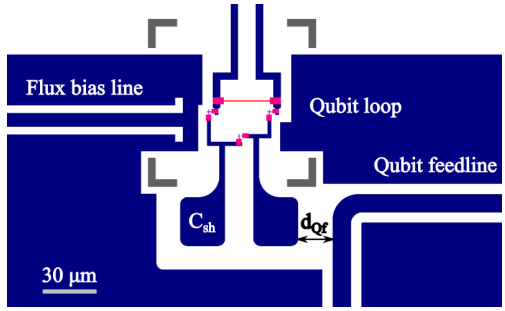

Figure 4.4: Flux qubit-resonator design zoomed around the qubit loop. The distance between the C_{sh} pad and the qubit feedline is given by the black arrow with $d_{Qf} = 19.5\,\mu m$.

Coupling inductor length

As previously discussed, the coupling inductor is fixed at $L_c = 0.5\,nH$. The choice of this inductance value is motivated by two reasons. First, our grAl recipe is calibrated and works best for samples evaporated with 0.6 sccm and 0.2 nm/s, leading to $L_{k,\square} \sim 10\,pH/\square$. Secondly, we cannot make arbitrarily large qubit loops or arbitrarily narrow and long wires. Big qubit loops will introduce flux

[3] https://www.comsol.com/

noise into our system, while designing long and narrow wires will translate into a lower fabrication yield.

If we take $L_c = 0.5\,\text{nH}$ and $L_{k,\square} \sim 10\,\text{pH}/\square$ we need about 50 squares of grAl. If we consider a qubit loop length of $\sim 30\,\mu\text{m}$ the design width of the grAl line will be of approximately $0.6\,\mu\text{m}$. This value gives room to adjust the grAl line to wider/narrower values if we see a drastic change in the calibration of the material.

Flux bias line design

We design the flux bias line (FBL) in *FastHenry*[4] which is a finite-element solver for the London equations at low frequencies. The qubit loop dimensions are given by the coupling inductor ($30\,\mu\text{m}$) and the Manhattan-style junctions ($18-22\,\mu\text{m}$).

The position of the FBL is determined by sweeping the location of the qubit in *FastHenry* as shown in Fig. 4.5. We target a mutual inductance between the line and the qubit of about $M = 0.1 - 0.2\,\text{pH}$ which occurs for $d_y = -0.5\,\mu\text{m}$ and $d_x = 18\,\mu\text{m}$. Note that the vertical and horizontal shifts are taken with respect to the center defined by the two top junctions and the lowest lead of the central junction. The choice of center is arbitrary and depends on the coordinates and geometry defined in the simulation.

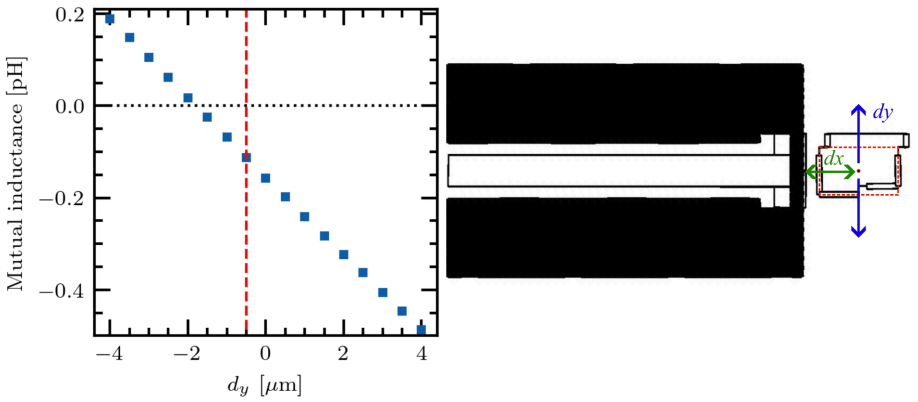

Figure 4.5: Left panel: simulated mutual inductance between the flux bias line and the qubit loop for $d_x = 18\,\mu\text{m}$, the red vertical dashed line indicates the selected design distance $d_y = -0.5\,\mu\text{m}$. Right panel: FastHenry simulation layout. The dashed red lines indicate the rectangle that defines the reference central point of the qubit loop.

[4] https://www.fastfieldsolvers.com/

The flux bias line adds a new loss mechanism into the qubit system since it is coupled to a resistive element such as the attenuator at the MXC plate. Following the lines of [Ith+05], one can estimate the qubit energy relaxation rate $\Gamma_{1,\mathrm{ind}}$ and dephasing rate $\Gamma_{\Phi,\mathrm{ind}}$,

$$\Gamma_{1,\mathrm{ind}} \approx \pi \left(\frac{2I_\mathrm{p}}{\hbar}\frac{\Delta_\mathrm{q}}{\omega_q}\right)^2 \left|\frac{M}{R+i\omega L}\right|^2 2R\hbar\omega \coth\left(\frac{\hbar\omega}{2k_\mathrm{B}T}\right), \tag{4.3}$$

$$\Gamma_{\phi,\mathrm{ind}} \approx 4\pi k_\mathrm{B}T \left(\frac{2I_\mathrm{p}}{\hbar}\frac{\epsilon}{\omega_q}\right)^2 \frac{M^2}{R}, \tag{4.4}$$

where I_p, Δ_q are the persistent current and the gap of the qubit respectively. ω_q refers to the frequency of the qubit at the operational point, M defines the mutual inductance between the flux line and the qubit, R and L are the real impedance and the inductance of the line, respectively, and T is the attenuator's temperature.

Considering $R = 50\,\Omega$, $L = 3\,\mathrm{nH}$, $M = 0.2\,\mathrm{pH}$, $\Delta_\mathrm{q}/h = 3.6\,\mathrm{GHz}$, and $I_\mathrm{p} = 72.4\,\mathrm{nA}$, operated at the sweetspot at $T \simeq 100\,\mathrm{mK}$, we obtain a minimum $T_1 \simeq 1.5\,\mathrm{ms}$, which is well above the limiting value imposed by the coupling to the qubit readout feedline. To estimate $T_{\phi,\mathrm{ind}}$ we choose a point far from the qubit sweetspot such that $\omega_q = \epsilon$. We obtain a value $T_{\phi,\mathrm{ind}} \simeq 40\,\mu\mathrm{s}$. This value looks rather low, but note that it is a point far from the sweetspot, where $I_\mathrm{p} \to \infty$

4.1.3 Coupled system

So far, we have been using the approximation in Eq. (4.1) as a guide to estimate the coupling coefficient from the individual parameters of the system. In order to give a proper estimate of the coupling coefficient we need to perform the complete numerical simulation of the system and calculate g from Eq. (3.31). In Fig. 4.6b, we provide the coupling coefficients as a function of the external flux. At the sweet-spot ($f = 0.5$) the coupling component is entirely transversal with value $g/2\pi = 1.9\,\mathrm{GHz}$. Comparing this result with the renormalized resonator frequency $\omega_A/2\pi = 4.9\,\mathrm{GHz}$ we obtain a coupling fraction of $g/\omega_A \approx 0.39 > 0.3$, which is in the non-perturbative USC regime (see Sec. 1.2).

The design presented here assumes that the coupling inductance and the Josephson junction currents are perfectly on target. However, from a fabrication point of view it is challenging to obtain the exact design values and thus it is advisable to have some tolerance in the area A, current density J_c and coupling inductance L_c. In Fig. 4.7, we show the value obtained for g/ω_A as a function of J_c and L_c. The black lines indicate the region where the system is in the non-perturbative USC regime. For values of J_c and/or L_c significantly above target, we should still be able to reach $g/\omega_A > 0.3$.

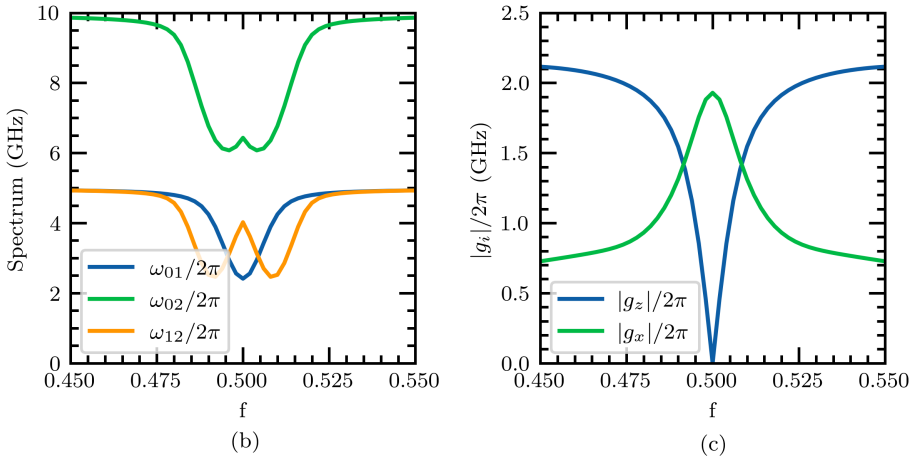

Figure 4.6: Simulated spectrum (a) and coupling coefficient (b) for the qubit-resonator design. The parameters used for the simulation are: $L_{\mathrm{R}} = 0.9\,\mathrm{nH}$, $C_{\mathrm{R}} = 740\,\mathrm{fF}$, and the qubit parameters listed in Table 4.2.

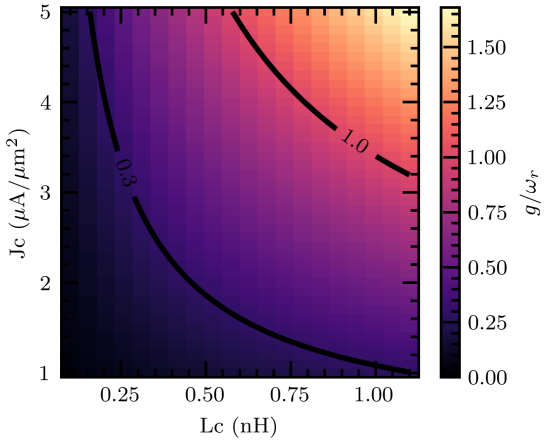

Figure 4.7: Coupling coefficient as a function of the junction current density J_{c} and the coupling inductance L_{c}. The simulation to obtain g uses the design parameters: $L_{\mathrm{R}} = 0.9\,\mathrm{nH}$, $C_{\mathrm{R}} = 742\,\mathrm{fF}$, and the qubit parameters listed in Table 4.2.

4.2 Spectrum characterization

Multiple devices have been fabricated using the recipes described in Ch. 3. Most of them suffered problems on the last fabrication step. It was latter realized that PMGI leaves a significant amount of residues which result in a lower I_c while affecting the quality of the contacts. This is the reason why we opted to replace PMGI by PMMA in the last EBL step. Furthermore, the multi-layer fabrication and the delicate structures turn out to a low fabrication yield. Nonetheless, one of the devices had a combination of off-target values that made it still suitable to validate the design and prove the grAl concept. In this section, we present the initial room-temperature and low-temperature characterization of this working device.

4.2.1 Room temperature and grAl characterization

The design of the chip contains a set of test junctions and grAl test structures that can be probed at room-temperature and low-temperature to estimate J_c and L_c.

The average resistance of junctions at room-temperature after a final bake at 200 °C for 7 min is $R_{JJ} = (5.2 \pm 0.1)\,\mathrm{k\Omega}$. The critical current of the junctions is estimated by the Ambegaokar-Baratoff formula [Amb+63] presented in Sec. 2.1.3, leading to a value of $I_c = (55.3 \pm 0.9)\,\mathrm{nA}$ for the big junctions. On the other hand, the areas of the Josephson junctions were estimated by imaging them using a scanning electron microscope (SEM). The estimated area for the big junctions is $A = (0.084 \pm 0.001)\,\mu\mathrm{m}^2$, while the small ones show $A = (0.045 \pm 0.001)\,\mu\mathrm{m}^2$, leading to $\alpha = 0.54 \pm 0.01$. The resulting Josephson and charging energies for the big junctions are $E_J/h = (27.5 \pm 0.5)\,\mathrm{GHz}$ and $E_C/h = (4.6 \pm 0.1)\,\mathrm{GHz}$, respectively, where in the later case we have used $S_c = 50\,\mathrm{fF}/\mu\mathrm{m}^2$.

The length of the grAl coupler is designed to be 30 µm and use SEM images to extract its width, $(487 \pm 15)\,\mathrm{nm}$. The room temperature resistance of the wire is extracted by measuring one of the test structures, giving $R_{RT} = (0.96 \pm 0.01)\,\mathrm{k\Omega}$. Using the design length of the coupler and the nominal thickness of the film 50 nm, we can extract the room-temperature resistivity of the grAl line, $\rho_{RT} = (78.3 \pm 2.5)\mu\Omega\,\mathrm{cm}$.

The kinetic inductance of grAl is estimated using the limit to the Mattis-Bardeen formula (2.1) introduced in Sec. 2.1.3,

$$L_k = 0.18 \frac{\hbar R_{4K}}{k_B T_c}. \tag{4.5}$$

where R_{4K} is the normal state resistance measured at 4 K and T_c is the critical temperature of grAl. In order to extract T_c and R_{4K}, we wirebond one of the test

structures in a 4-probe configuration and measure current-voltage (IV) curves in temperature. We use the different IV curves to extract the resistance as a function of temperature $R(T)$. These measurements are performed on a dry dilution refrigerator fridge where the temperature is controlled manually below 4 K by adding small amounts of He^3/He^4 mixture while adjusting the heaters. For low temperatures, approaching T_c, we set low enough currents and we adjust the repetition rate of the measurement to avoid excessive heat dissipation when the sample is in the normal state. More details on critical temperature measurements can be found in Ch. 5. The resulting $R(T)$ curve for one of the grAl test structures mimicking the coupler is shown in Fig. 4.8. We define the critical temperature as the point where the resistance has decreased 50% respect to the onset value. The temperature difference between the points where the resistance has decreased a 10% and 90% of the onset value define the width of the transition. Following these definitions, we estimate the critical temperature of the grAl coupler to be $T_c = (1.60 \pm 0.31)$ K.

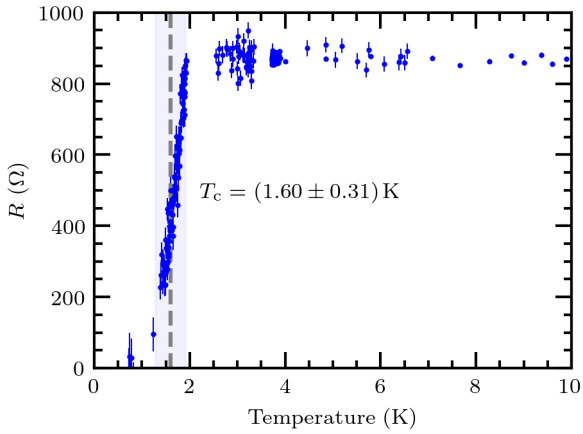

Figure 4.8: Resistance versus temperature curve for the grAl coupler test structure. The dashed vertical line indicates the point where the resistance has dropped 50% of the onset value while the shadowed area indicates the width of the transition.

Using the value of resistance obtained at 4 K, $R_{4K} = (0.86 \pm 0.01)\,\text{k}\Omega$ and the critical temperature $T_c = (1.60 \pm 0.31)$ K, we estimate the inductance of the grAl coupler to be $L_c = (0.74 \pm 0.14)$ nH, which is significantly above the target 0.5 nH of the design, yet still allowing the device to be in the USC regime.

Figure 4.9 shows the resulting estimated qubit-resonator spectrum and energy ladder using $L_c = 0.74$ nH, $A = 0.084\,\mu\text{m}^2$, $\alpha = 0.54$ and $I_c = 55.3$ nA.

The expected coupling coefficient obtained using the estimated parameters is $g/2\pi \approx 0.67\,\mathrm{GHz}$ and $g/\omega_A \approx 0.15$, where we have used the renormalized resonator frequency $\omega_A/2\pi = 4.56\,\mathrm{GHz}$. The coupling is still sufficiently large to enter in the perturbative USC regime. In addition to the qubit-resonator spectrum, we can estimate qubit parameters. Simulating a Csh 3JJ flux qubit with non-negligible loop inductance given by L_c and the parameters given above, we obtain $I_\mathrm{p} = 19.63\,\mathrm{nA}$ and $\Delta_\mathrm{q}/h = 4.71\,\mathrm{GHz}$ for the qubit. Note that the expected qubit persistent current is more than 3 times smaller than the design value. Nevertheless, such a low current indicates a potentially more coherent device.

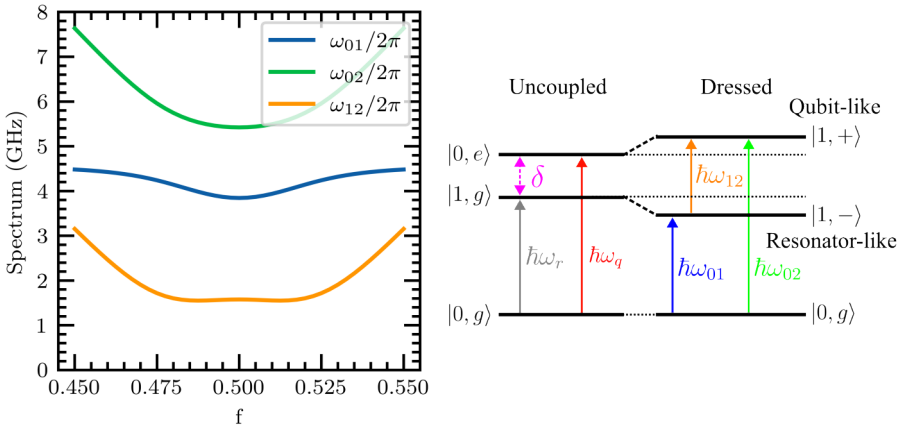

Figure 4.9: Estimated spectrum and energy ladder for the qubit-resonator system. Left: qubit-resonator spectrum obtained using the estimated values at room temperature of the grAl kinetic inductance L_c, junction current density J_c and junction areas A. The resonator parameters used are $L_\mathrm{R} = 0.9\,\mathrm{nH}$ and $C_\mathrm{R} = 0.74\,\mathrm{pF}$. Right: schematics of energy ladder near the sweetspot for the estimated spectrum presented on the left panel. In the perturbative USC regime, the states of the system can be expressed as dressed states $\{|1,+\rangle, |1,-\rangle\}$ of even and odd superpositions of the uncoupled qubit-resonator states $\{|n-1,e\rangle, |n,g\rangle\}$ with a perturbative effect of the counter-rotting terms [For+16]. The term resonator(qubit)-like indicates that the dressed state has a predominant component of the bare resonator (qubit) state.

4.2.2 Low-temperature transmission measurements

Figure 4.10 shows a false-colored image of the completed device. The chip is packaged in a copper sample box with a coil to tune the flux through the qubit

loop. The sample is then mounted on the base-temperature plate of our dilution refrigerator with input/output connections on either one of the feedlines since we have one cold amplifier. The rest of the ports are terminated with a 50 Ω termination.

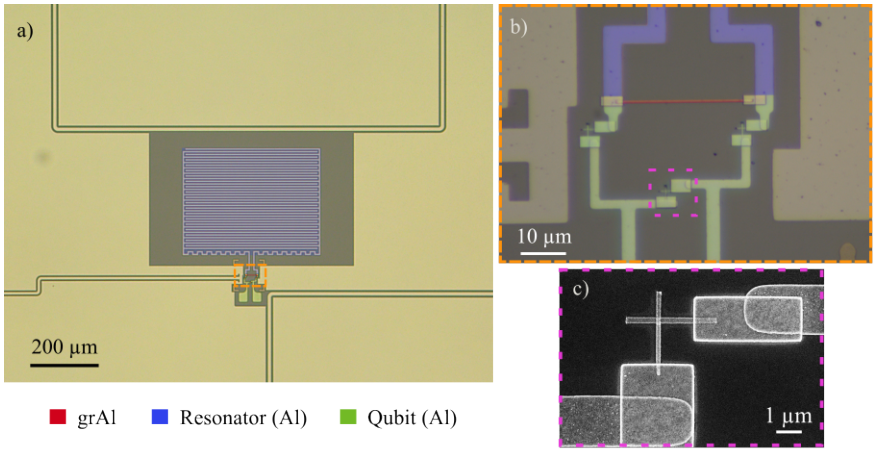

Figure 4.10: False colored images of the device. (a) shows the complete qubit-resonator system with the different feedlines, (b) is a zoom into the qubit loop and (c) is a SEM image of the small junction of the device.

We measure the sample in transmission using a single-tone measurement technique as described in Sec. 2.2. Using a Vector Network Analyzer (VNA), we scan with a tone at frequency f_{sys} while monitoring the transmission. The different resonant frequencies of the system appear as dips in $|S_{21}|$. Thanks to the layout of the device, we can run this measurement independently through the resonator (S_{21}^{R}) or the qubit (S_{21}^{Q}) feedline. In Fig. 4.11, we show the resulting transmission spectrum of the system through (a) resonator and (b) qubit feedline as a function of the external flux. The magnitude of the transmission is normalized as,

$$|S_{21}^{\text{norm}}(f_i, \Phi_{\text{ext}})| = \{|S_{21}(f_i, \Phi_{\text{ext}})| - \min(|S_{21}(f_i, \Phi_{\text{ext}})|)\} / \text{std}(|S_{21}(f_i, \Phi_{\text{ext}})|)$$

where f_i is the frequency at each trace. The signal is normalized to eliminate spurious box modes which offset the vertical range.

In both measurements, we observe two main transitions, one between 4 and 4.5 GHz and another one between 6 and 8 GHz. The lower one (ω_{01}) has more resonator-like component, while the higher transition (ω_{02}) is mostly related to the qubit. This information can be extracted from the mode analysis of the estimated spectra of the circuit (Fig. 4.9). Additional features appear at flux

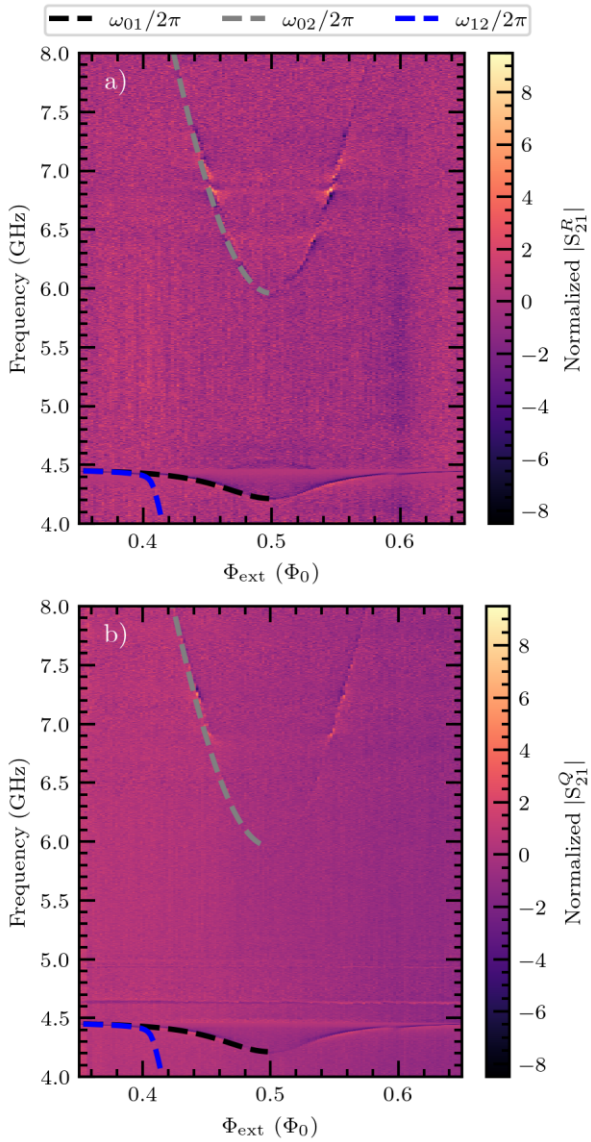

Figure 4.11: Normalized transmission magnitude vs. flux bias (Φ_{ext}) obtained via single-tone spectroscopy. The dashed lines correspond to the fitted Quantum Rabi Model spectrum with fit parameters Δ_q, I_p and g. See the main text for more details. a) Spectrum obtained measuring through the resonator feedline. b) Spectrum obtained measuring through the qubit feedline.

$\Phi_{\text{ext}}/\Phi_0 \sim 0.4$ and 0.6 which come from intermediate transitions such as ω_{12}. The identification of the different transitions will be further investigated with two-tone spectroscopy measurements discussed in following sections.

From the theory derived in [Mag+21], we expect significant differences in the transmission spectra when probing the system through qubit or resonator. In particular, one should expect the resonator-like transition to vanish outside the sweetspot when probing the system through the qubit feedline and, the qubit-like transition to be dimmer when the system is probed through the resonator. Instead, in our experiment, although $|S_{12}^R|$ for ω_{01} is $\sim 5\,\text{dB}$ dimmer than $|S_{21}^Q|$, we do not see the signal disappear for flux $\Phi_{\text{ext}}/\Phi_0 < 0.45$ and $\Phi_{\text{ext}}/\Phi_0 > 0.55$. In Fig. 4.12, we show the raw $|S_{21}|$ data around 4.5 GHz where the signal is comparable in both measurements. Note that one of the spurious box modes at 4.36 GHz is not present in the qubit measurement. We took advantage of the fact that the measurements were performed in different cooldowns, and we included a copper piece inside the sample box to fill in empty space and bring box modes to higher frequencies (see Sec. 2.2 for more details). Similarly to the first transition, the $|S_{21}|$ signal at ω_{02} is comparable for both measurement configurations. In this region of the spectrum, it is very difficult to give a quantitative difference on the transmission magnitude due to the low signal (see Fig. 4.13). The differences between theory and experiment could come from either an over-coupling of the qubit/resonator to the feedline or a stray crosstalk between lines.

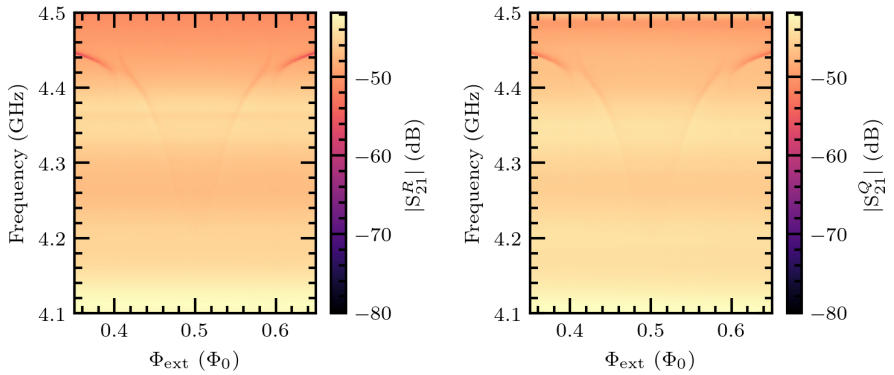

Figure 4.12: Raw $|S_{21}|$ data around 4 GHz obtained by probing the system through (a) resonator and (b) qubit feedline as a function of the external flux.

We simulate in *Sonnet* the qubit-resonator system with both feedlines to understand the small differences between the single-tone spectra presented in

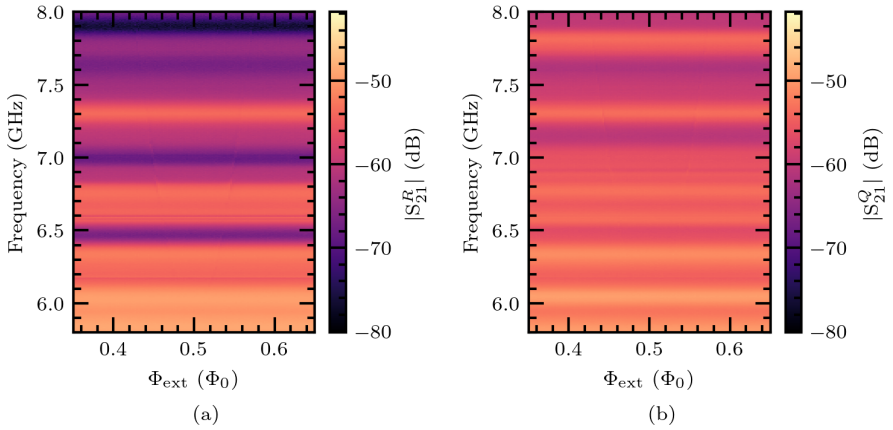

Figure 4.13: Raw $|S_{21}|$ data between 5 GHz and 8 GHz obtained by probing the system through (a) resonator and (b) qubit feedline as a function of the external flux.

Fig. 4.11. The schematics of the simulation is shown in Fig. 4.14. We start by simulating the resonator coupled to the qubit by an ideal inductor with $L_c = 0.74\,\text{nH}$. In order to simulate the qubit, we remove the Josephson junctions of the design, keep the C_{sh} capacitor, and use ideal inductor and capacitor elements to mimic the qubit resonance frequency at the sweetspot. For both feedlines (see left panels in Fig. 4.15) we observe a resonance centered at 4.45 GHz with a magnitude which is $\sim 4\,\text{dB}$ smaller in the qubit feedline case. The crossed signal S_{14} between feedlines is in general below $-10\,\text{dB}$, with a peak around 4.45 GHz which is compatible with the excitation of the resonator. The $\sim 4\,\text{dB}$ difference between $|S_{21}|$ and $|S_{43}|$ in the simulations is consistent with the one observed in the experiments between $|S_{21}^{\text{Q}}|$ and $|S_{21}^{\text{R}}|$ ($\sim 5\,\text{dB}$). On the other hand, given the low crossed signal S_{14}, the direct crosstalk between feedlines is at a level of $-25\,\text{dB}$.

To discard that the coupling between qubit feedline and resonator comes directly from the C_{sh}, we perform a second simulation consisting of removing completely the qubit loop and the C_{sh} capacitor. In addition to focusing on the different resonances, we analyze the currents of the simulation. In the central panels of Fig. 4.15, we observe that even though the qubit parts are not present in the simulation, the resonator resonance is still present when probing the system through the qubit feedline (S_{21}). An analysis of the currents indicates that the open ground plane around the bottom feedline provides a current path through the ground towards the resonator inductor. These stray currents provide a direct

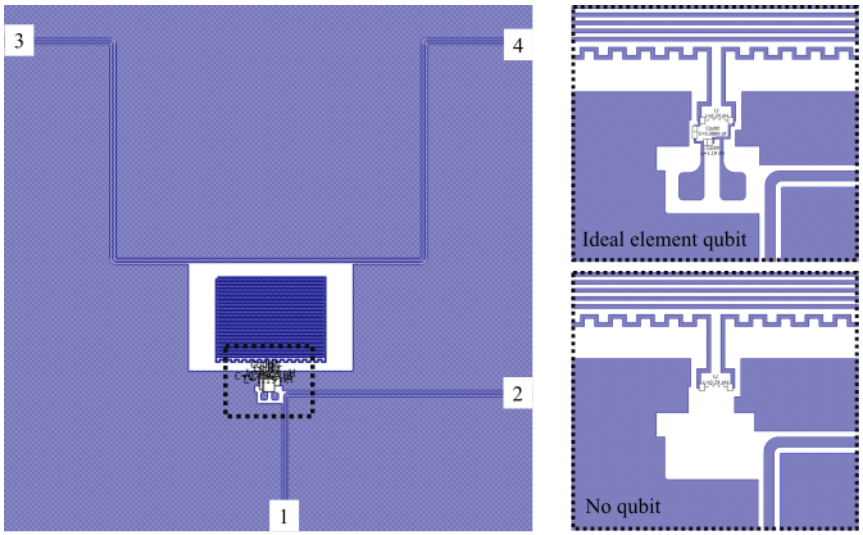

Figure 4.14: *Sonnet* simulation layout. The left panel provides the port labels for both feedlines. The right panels are an enlarged view around the qubit loop for a qubit simulated out of ideal elements (top), and a simulation without qubit loop (bottom).

coupling between the qubit feedline and the resonator which could explain the similar transmission in Figs. 4.11 a), b).

The coupling of the resonator to the qubit feedline may be minimized by closing the ground plane surrounding it. There are two possibilities; the first is to modify the lithography design and connect the two sections with an Al line, and the second one consists of including an air bridge. We test both solutions in *Sonnet* and simulate the resonator without qubit. In both cases, the currents through the ground edges are significantly reduced and $|S_{21}|$ is now practically unmodified around the resonance frequency of the resonator. Therefore, by connecting both ground planes, the stray coupling of the resonator to the qubit feedline is canceled. This will be considered in future device designs.

Coupling estimate

Using the data obtained via single-tone spectroscopy, we extract the frequency values corresponding to the lowest transition labeled ω_{01}. We use these values to perform a two-tone spectroscopy measurement. We send a tone at ω_{01} while scanning in frequency with another tone at f_{sys}. When f_{sys} excites one of the

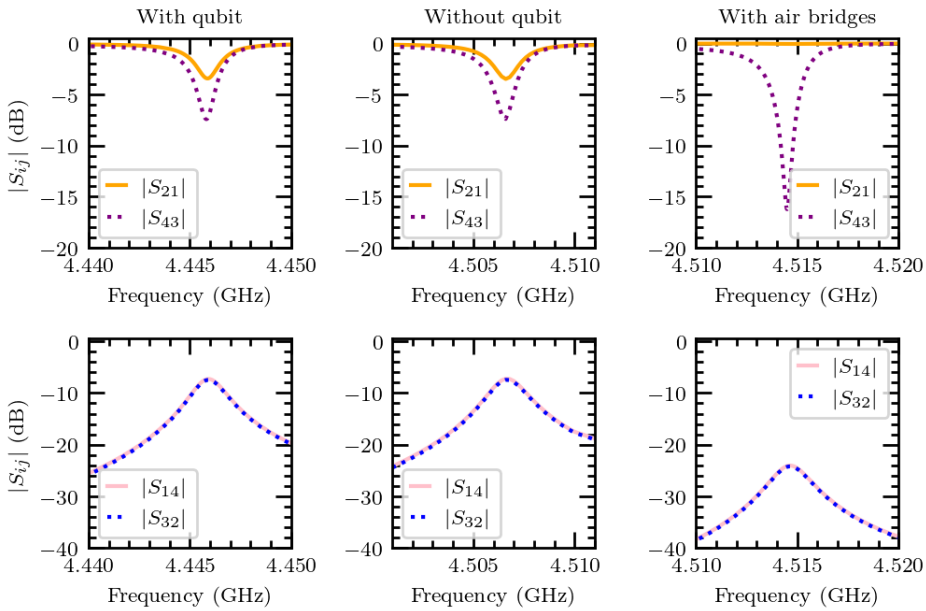

Figure 4.15: $|S_{ij}|$ for different *Sonnet* simulations with two feedlines. $|S_{21}| = |S_{21}^{Q}|$, $|S_{43}| = |S_{21}^{R}|$, and $|S_{14}|$ and $|S_{32}|$ are the crossed signals between resonator and qubit feedlines. Left panel: simulation with ideal element qubit. Central panel: simulation without qubit and C_{sh} capacitor. Right panel: simulation without qubit and C_{sh} capacitor where the ground planes are connected by air bridges.

transitions of the system, it produces a shift in ω_{01} and we observe a change in transmission. This process is repeated for different external flux values. The resulting normalized spectrum is shown in Fig. 4.16.

We identify four out of the five transitions visible in the spectrum. ω_{01} is mostly related to the resonator and it is the transition used to measure in the two-tone configuration, while ω_{02} has more qubit component. The intermediate transition ω_{12}, which is also visible using single-tone spectroscopy, and a two-photon transition to ω_{03}. One spectral line, indicated with a black arrow in Fig. 4.16 around 5 GHz and $\Phi_{\mathrm{ext}}/\Phi_0 = 0.36$, seems to match a type of three-photon blue-sideband transition with $\hbar(\omega_{01} + \omega_{03})/3$.

In order to extract the system parameters, we fit the visible transitions in single-tone and two-tone spectroscopy to the Quantum Rabi Model (3.18) pre-

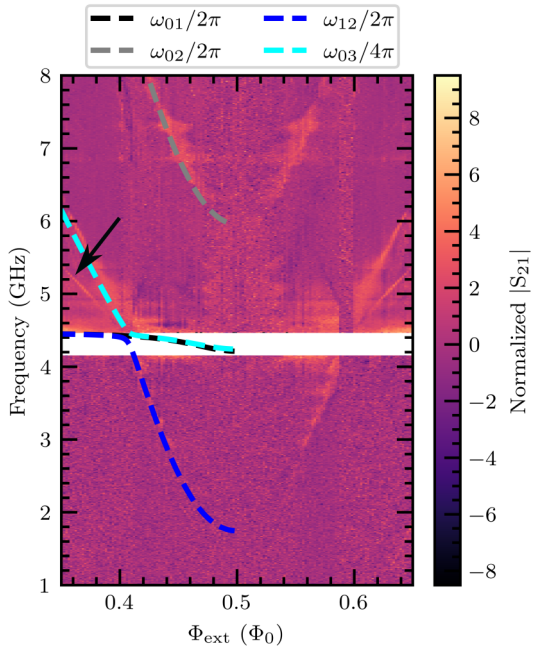

Figure 4.16: Normalized transmission magnitude vs. flux bias (Φ_{ext}) obtained via two-tone spectroscopy using the qubit feedline. The resonator tone is fixed at the frequencies defined by the ω_{01} transition measured using single-tone spectroscopy. The dashed lines correspond to the fitted Quanutm Rabi Model spectrum with fit parameters Δ_{q}, I_{p} and g. The arrow indicates the three photon process described in the main text.

sented in Ch. 3,

$$\hat{\mathcal{H}}_{\text{QRM}} = -\frac{1}{2}\left(\epsilon\hat{\sigma}_z + \Delta_{\text{q}}\hat{\sigma}_x\right) + \hbar\omega_r\left(\hat{a}^\dagger\hat{a} + \frac{1}{2}\right) + \hbar g\hat{\sigma}_z\left(\hat{a} + \hat{a}^\dagger\right), \tag{4.6}$$

where $\epsilon = 2I_{\text{p}}\left(\Phi_{ext} - \frac{\Phi_0}{2}\right)$. We implement a *least-squares fitting* with the package *iminuit*[5] that fits ω_{01}, ω_{02}, part of ω_{12} and $\omega_{03}/2$ simultaneously. The resulting values of the fit read $I_{\text{p}} = (11.619 \pm 0.004)\,\text{nA}$, $\Delta_{\text{q}}/h = (5.707 \pm 0.002)\,\text{GHz}$, $g/2\pi = (0.578 \pm 0.001)\,\text{GHz}$ and $\omega_r/2\pi = (4.463 \pm 0.001)\,\text{GHz}$. The frequency of the resonator mode is also independently obtained by measuring in transmission at high powers. For high enough power, the qubit saturates (similarly to a

[5]https://scikit-hep.org/iminuit

punch-out measurement [Ree+10]) and ω_{01} does not change in flux. This saturated transition corresponds to the renormalized LC resonator frequency ω_r. The measured frequency using this procedure is $\omega_r/2\pi = 4.465\,\mathrm{GHz}$, which is compatible with the fitted parameter.

From the resulting fitted parameters we estimate the strength of the interaction, $g/\omega_r \simeq 0.13 > 0.1$. The coupling still falls in the perturbative USC regime despite the small persistent current of the qubit. The result is consistent with the repulsion between levels observed near the qubit sweet-spot as well as the multiple spectral lines observed by single-tone spectroscopy. The coupling of the system could easily be increased by designing larger coupling inductors. This result opens the door to studying flux qubits with low persistent currents in the USC regime using superinductor materials as couplers, potentially leading to a highly coherent system in the USC regime.

4.2.3 USC spectrum discussion

In this section, we present the main spectral features of the measured qubit-resonator system and we discuss some visible USC features.

Comparison with the Jaynes-Cummings model

In the previous section, we have concluded that the qubit-resonator coupling satisfies the condition $g/\omega_r > 0.1$. This implies that the system is in the ultrastrong coupling regime and the effect of counter-rotating terms is non-negligible. This effect can be quantified by the Bloch-Siegert shift (ω_{BS}) which is given by the difference between the Jaynes-Cummings (JC) spectrum and the Quantum Rabi model spectrum [For+10]. As seen in Fig. 4.17, the resonator experiences a downward shift respect to the JC spectrum. The shift is maximal at the sweetspot, corresponding to the region of maximal qubit-resonator coupling.

Figure 4.18 shows the data corresponding to the ω_{01} transition together with the QRM fit and the resulting JC spectrum using the QRM fitting parameters. The orange data points are extracted by fitting S_{21}^{R} to the resonator model from [Pro+15] (see Sec. 5.4.2 for more details on resonator fitting). The error-bars are given by the extracted linewidth of the transition. The signal at the sweetspot is very low and the resonator fitting fails. For this region (blue points) we extract the data as the minima of the normalized $|S_{21}^{R}|$. The error bars are an estimate of the linewidth based on the normalized spectra. As expected, the JC model predicts a higher resonance frequency at the sweetspot. The right panel of Fig. 4.18 allows us to quantify the Bloch-Siegert shift. We show the difference between the QRM and the JC model $\omega_{01}^{\mathrm{QRM}} - \omega_{01}^{\mathrm{JC}}$, and the difference between the dataset and the JC model $\omega_{01} - \omega_{01}^{\mathrm{JC}}$. As previously anticipated, the difference between the QRM and the JC is maximum at the sweetspot with a value of $\sim 23\,\mathrm{MHz}$

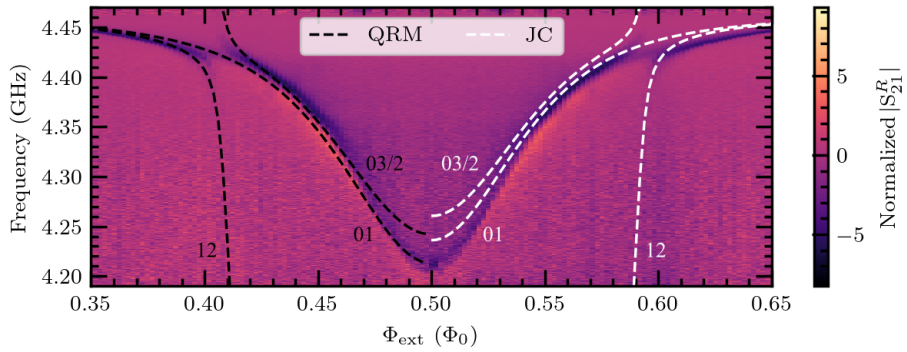

Figure 4.17: Zoom around the ω_{01} transition. In black we show the fitted QRM spectrum and in white the calculated JC spectrum using the QRM fitting parameters.

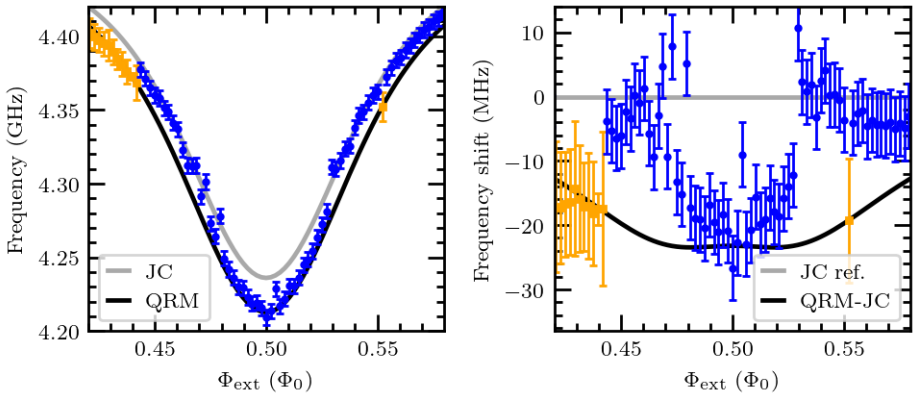

Figure 4.18: Comparison between the QRM fit and the JC model near the sweetspot for the lowest transition, ω_{01}. Left panel: comparison between QRM and JC models, in orange data points extracted via resonator fit on S_{21}^R, in blue data points extracted as the minima of $|S_{21}^R|$ normalized. In black we show the fit to the QRM and in gray the calculated JC spectrum using the fitting QRM parameters. Right panel: extraction of the resonator shift by subtracting the JC spectra to the data points and QRM spectra shown in the left panel. The difference is the Bloch-Siegert shift, with a maximum at the sweetspot of $\omega_{BS}/2\pi = 23\,\text{MHz}$.

for the ω_{01} transition. This difference corresponds to the Bloch-Siegert shift $\omega_{BS} = g^2/(\omega_r+\omega_q)$. We can use this shift to estimate the coupling coefficient. At the sweetspot, $\omega_{BS}/2\pi = 23\,\mathrm{MHz}$, $\omega_r/2\pi = 4.463\,\mathrm{GHz}$ and $\Delta_\mathrm{q}/h = 5.707\,\mathrm{GHz}$, we obtain a coupling coefficient $g \simeq 0.48\,\mathrm{GHz}$ and a fraction $g/\omega_r \simeq 0.11$, which is consistent with the QRM fitted parameters.

Comparison with the expected spectrum

In Sec. 4.2.1, we have presented the estimated spectrum of the system obtained using the parameters derived from resistance measurements both at room-temperature and at low-temperature. The initial coupling strength estimate was $g/\omega_r \simeq 0.15$ which is not far from what we obtained in the experiment, $g/\omega_r \simeq 0.13$. Still, there are significant differences in the spectra. Figure 4.19 shows the expected (solid) and fitted QRM (dashed) spectrum.

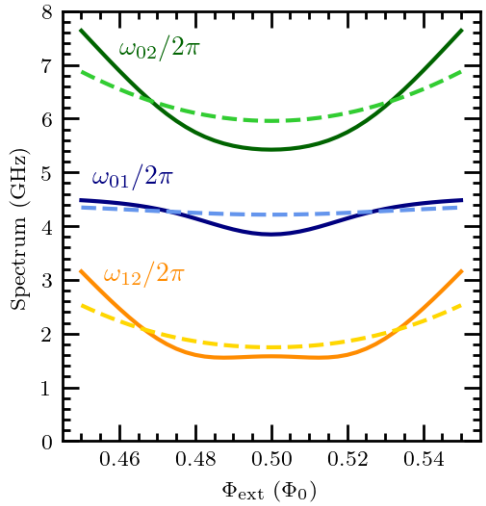

Figure 4.19: Comparison between the expected (solid) and fitted QRM (dashed) qubit-resonator spectrum obtained using the parameters listed in Table 4.3.

There is a considerable difference in the curvature of ω_{02} between expected and fitted spectra, which indicates a difference in qubit persistent current. In fact, there is almost a factor two difference (see Table 4.3 for a summary of the expected and fitted parameters). Similarly, the difference in qubit gap is $\sim 1\,\mathrm{GHz}$ which explains the bigger change in ω_{01} around the sweetspot for the expected spectrum.

Table 4.3: Summary of expected and fitted spectrum parameters. The expected parameters are extracted from room-temperature measurements and low-temperature resistance measurements, while the fitting parameters are obtained fitting the qubit-resonator spectrum to the QRM.

	I_p (nA)	Δ/h (GHz)	$\omega_r/2\pi$ (GHz)	$g/2\pi$ (GHz)
Expected	19.63	4.72	4.56	0.67
Fitted	11.619 ± 0.004	5.707 ± 0.002	4.463 ± 0.001	0.578 ± 0.001

The differences between expected and fitted spectra can be explained by deviations in the estimated qubit parameters. For example, we used the area of junctions fabricated in neighboring chips, but this does not warrantee that the junctions of the measured qubit are the same. Similarly, we used the resistance at room-temperature to estimate the critical current of the junction. However, the room-temperature resistance of the junction can be significantly different from its the normal state resistance. Finally, we set the design parameters for the different qubit capacitances which might differ from the actual value. Recall that C_J is calculated from $S_\mathrm{c} = 50\,\mathrm{fF}/\mu\mathrm{m}^2$, which is an estimated parameter. Additionally, small deviations in the dimensions of the shunted capacitor pads may also lead to differences between the designed and real value of C_sh

Even though the expected qubit parameters were off-target, the resonance frequency of the resonator was quite similar to the one of the measured device. This tells us that the coupling inductor estimate was close to the actual value. The 100 MHz difference to the measured value could be due to the use of design parameters L_R and C_R, or to inhomogeneities of grAl across the chip. Finally, we can compare the designed loaded quality factor of the resonator with the extracted one by fitting S_{21}^R far from the sweetspot. For $f = 0.28$ we extract $Q_\mathrm{L} \simeq 1000$ which is 5 times lower than the design value. The difference may come from the stray couplings to the qubit feedline, as discussed in Sec. 4.2.2.

4.3 Outlook

Although the results presented in the previous section are promising, several improvements can be made in the design to yield a mode robust experiment:

- Verify the absence of cross-talk between feedlines by measuring variations of the device presented in previous sections. One copy should contain only one feedline coupling either to qubit or resonator.

- Characterize the limitations imposed by the qubit feedline. The goal is to determine a minimal coupling to the feedline such that the qubit coherence

is not limited by this loss channel. This can be addressed by designing a qubit coupled to a modified resonator with very high frequency. The L_R is kept identical to the original design to consider for the renormalization of the qubit spectrum.

With this in mind, we propose variations of the device presented in Sec. 4.1. The goal of this new generation of devices is to discard crosstalk between feedlines and understand better the readout of the system through the qubit. The three proposed devices are shown in Fig. 4.20. The first copy represents a control for the complete experiment. The second copy does not contain the qubit feedline, and the third one only contains the qubit feedline and the capacitance of the resonator is modified to yield a resonator with a resonance frequency well above 8 GHz. This third configuration will be used to study single qubit scattering.

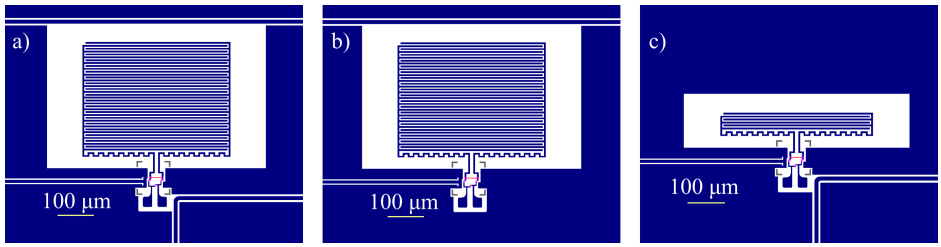

Figure 4.20: Desing variations for the new generation of devices. (a) old design containing two feedlines; (b) design with only the resonator feedline (c) design with the modified resonator capacitance and a single feedline coupling to the qubit to study single qubit scattering.

In these new devices we include test structures to probe the grAl and Josephson junctions in intermediate steps of fabrication. In Fig. 4.21 we show the different test structures designed for the new generation. Structures (a) and (b) were already present in the old design and they mimic the final structures in the chip. Structures (c) and (d) are an adapted single-layer version of the previous two. These new structures will allow us to adjust the parameters after each fabrication step to ensure that the final chip is in the non-perturbative USC regime.

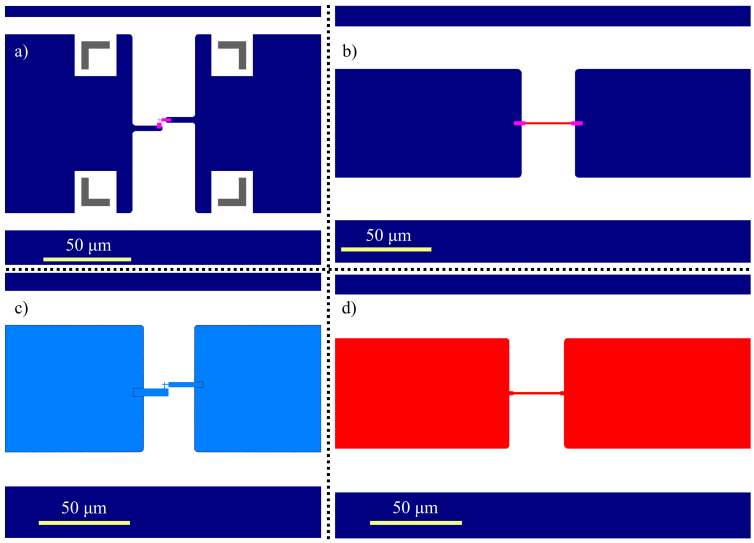

Figure 4.21: On-chip test structures: (a) test junctions with contacts (old); (b) grAl test line with contacts (old); (c) test junctions to be fabricated on a single EBL step (new); (d) grAl line to be fabricated on a single EBL step (new).

Chapter 5

Superconducting Nitridized-Aluminum thin films

Alba Torras-Coloma, Leyre Martínez de Olcoz, Eva Céspedes, Elia Bertoldo, David López-Núñez, Sagar Paul, Wolfgang Wernsdorfer, Gemma Rius, and P. Forn-Díaz

Contents

Chapters 3 and 4 have focused on the design and measurement of superconducting quantum circuits which benefited from the properties of superinductor materials to reach the USC regime. We chose granular Aluminum for our device given its relative ease to combine with Al-based fabrication [Grü+19]. However, there is a wide span of superinductor materials suited for research in superconducting qubits. In particular, new efforts are currently being invested in the development of nitride-based superconductors, which may result in higher-quality devices than the oxygen-based ones such as grAl.

In this chapter, we explore the superconducting properties of nitridized Aluminum (NitrAl) thin films. As we will show along the chapter, the superconducting properties of NitrAl can be tuned by modifying the film deposition parameters. The enhanced critical temperatures, reaching up to $3.38 \pm 0.01\,\mathrm{K}$, combined with the resilience to magnetic fields in resistive samples, and the significantly large kinetic inductance, make NitrAl a promising material for superconducting qubit applications. The samples studied in this chapter were provided by the Centro Nacional de Microelectrónica (CNM) and the magnetic field measurements were performed by S. Paul at Karlsruhe Institute of Technology (KIT). The room-temperature and low-temperature characterizations together with the analysis of the data was performed at the Institute of High Energy Physics (IFAE).

5.1 Introduction

Material research and engineering is gaining interest in the superconducting qubit community. Currently, one of the limitations in qubit coherence and resonator quality comes from imperfections in the metal layers, unwanted oxides growing in interface layers, and lossy dielectrics from fabrication residues [Sid21]. It has been shown that an appropriate choice of superconducting material can help reduce losses in the form of two-level system (TLS) defects arising in metal-surface and metal-air interfaces. Nitride-based superconductors have high quality interfaces and surfaces that are stable against oxidation, which helps reducing the presence of TLSs compared to Al or Nb films [Bar+08]. In particular, superconductors such as NbTiN, TiN, NbN, have shown to provide improved coherence times in qubits [Cha+13; Kim+21; Den+23] and resonator internal quality factors above 10^5 at low powers [Vis+10; Fra+23]. Besides being good candidates from the low-loss point of view, thin nitride-based disordered superconductors generally display a large kinetic inductance (L_{kin}) [Cou+12; Nie+19]. This property is of key importance for building high-impedance superconducting circuits while keeping relatively low losses. The applications of these materials are not limited to superconducting quantum qubits. Devices such as parametric amplifiers [Ho +12], single photon detectors [Gao+12; Dor+08], or kinetic inductor detectors [Doy+08] might also benefit from large L_{kin} materials.

In this chapter, we take the ideas from grAl fabrication and the properties of nitride-based superconductors to present a new superconducting material based on Al nitridization with potential for superconducting qubit circuit applications. As reviewed in Ch. 2, grAl can be fabricated by evaporating Al in an oxygen atmosphere [Grü19]. This process results in a material consisting on an $\mathrm{Al} - \mathrm{AlO_x}$ matrix of grains with properties differing from Al, namely higher T_c [Des+25; Lev+19], higher resilience to magnetic fields [Bor+20] and a large kinetic inductance [Grü+18; Zha+19]. Intuitively, one should be able to obtain a nitridized

Aluminum film by replacing the oxygen by nitrogen in the Al deposition process. However, N_2 does not naturally react with Al, thus, evaporating it in a nitrogen atmosphere is not a viable option. The alternative is to use reactive sputtering deposition, in which a reactive gas (in our case N_2) is introduced along with Ar to create a plasma [Lic98]. Reactive DC-magnetron sputtering is usually used to fabricate crystalline Aluminum nitride (AlN), a material widely used in the microelectronics community and well-known for its piezoelectric properties [Kar+09; Cle+01]. From the point of view of superconducting qubits, using AlN with non-zero piezoelectricity can represent a major source of loss in the form of phonon dissipation, impacting directly the coherence of qubits [Bia+06]. Works in all-nitride Josephson junctions have shown that the growth of the film is key to avoid piezoelectricity in AlN. Examples are the works by *Y. Nakamura et al.* and *Sunmi Kim et al.* where a cubic crystal phase of AlN is used as the insulator layer in NbN/AlN/NbN Josephson junctions. Due to the cubic symmetry of the AlN phase, no piezoelectricity is expected in the insulator layer of the junction with incident perpendicular electric fields [Nak+11; Kim+21].

However, the interest of this work does not lie in insulating AlN but in regimes where the material behaves as a superconductor. In order to grow nitridized Aluminum films with metallic behavior, one can sputter Al in non-stoichiometric conditions and adjust the N_2/Ar ratio to tune the properties of the resulting material. Since the material will not grow in a cristalline form, in principle, we should be able to avoid piezoelectricity in nitridized Aluminum films. Using DC-magnetron sputtering with N_2 as the reactive gas, we prepare a set of nitridized Aluminum samples sputtered in different N_2/Ar process flows. We name the resulting material NitrAl, a short name for nitridized Aluminum. To our knowledge, the superconducting properties of NitrAl have not been studied prior to our work [Tor+24], and only minimal signs of superconductivity were gathered in studies in the 70's and 90's [Har74; Mor90].

In the following sections, we present the study of the superconducting properties of NitrAl. We focus on the differences in temperature-resistance behavior, critical temperatures, and magnetic field dependence for films sputtered in different N_2/Ar process flows. The results presented in this chapter and in [Tor+24] have been recently validated and extended by other works. In [Lee+24], the authors reproduce the critical temperature and critical magnetic field study of the films, while providing new insights on the material morphology. Similarly, the work by [Góm24] provides an extensive study on the superconducting and room-temperature properties of NitrAl films at different thicknesses.

5.2 Room-temperature properties

NitrAl samples were fabricated by DC-magnetron sputtering on a Si substrate with an insulating SiO_2 layer. The thickness of the samples was targeted at 100 nm and the sputtering process was performed at a 4-inch wafer sale. Different nitridization levels were studied by changing the fraction of nitrogen (N_2/Ar) during deposition. The details of the fabrication are listed in Appendix C. The samples were diced into squares of $\sim 7\,\text{mm} \times 7\,\text{mm}$ and mounted on commercial ceramic chip carriers. We wirebonded the corners of the chip into a Van der Pauw 4-probe configuration. The sheet resistance is extracted from fitting current-voltage (IV) curves and accounting for the factor $\pi/\ln 2$ [Pau58].

In Fig. 5.1 (a), we show the resulting resistivity at room temperature for different N_2/Ar process flows. In blue, we show the data obtained performing in-line 4-probe measurements at wafer scale prior to dicing. In red and black, we show the resistivity of $7\,\text{mm} \times 7\,\text{mm}$ samples fabricated in two different runs. We observe a general increase of resistivity at room temperature with increasing fraction of N_2 in the sputtering process. In particular, there is a rapid increase between 0% and 5% of N_2/Ar. The curve then flattens between 5% and 6.67% and above 8.33% starts to increase again. Samples sputtered with flows of 15% or above show an insulator behavior and high resistance of the order of MΩ. The IV's are no longer linear with charging effects displayed as a change in voltage offset. On the other hand, a change in surface film color is observed in insulating samples. While conducting films have silver-colored surfaces resembling Al, insulating samples become green, indicating a change in optical properties. Samples prepared in different fabrication runs but with the same ratio of N_2/Ar show significant reproducibility. The differences in resistivity between runs and between wafer-scale and chip-scale films might come from inhomogeneities in the N_2 incorporation. However, further studies on the film composition are needed in order to properly assess this point.

5.3 Low-temperature properties

Samples were mounted either on the mixing chamber or the still plates of a dry dilution refrigerator. The low-temperature properties of the samples were studied by measuring IV-curves continuously in temperature. The maximum current applied and the measurement repetition rate were adjusted depending on the resistance of the sample and the temperature.

In Fig 5.1 (b), we show the residual resistivity ratio ($RRR = \rho_{\text{RT}}/\rho_{\text{4K}}$) as a function of the N_2/Ar flow used during sample fabrication. We observe that samples sputtered with $N_2/\text{Ar} < 10\%$ have an RRR above 1. Thus, the resistivity

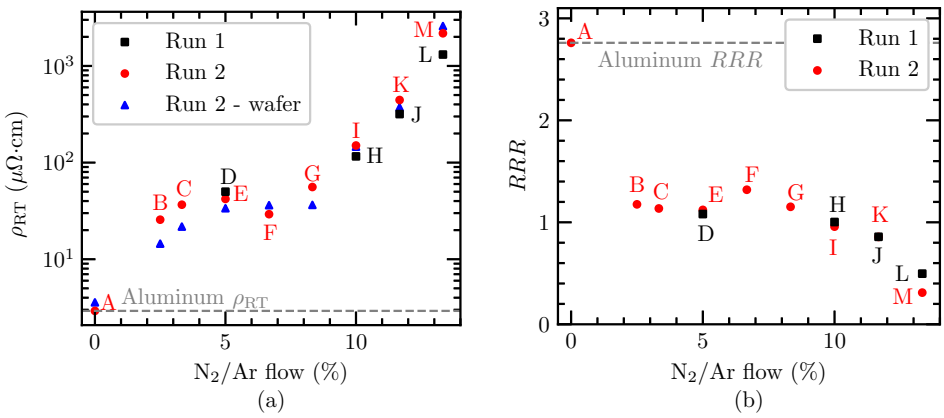

Figure 5.1: (a) Room-temperature resistivity (ρ_{RT}) as a function of the fraction of N_2/Ar flow used in the fabrication process. The blue triangles correspond to the wafer scale data while the black (red) squares (circles) show the resistivity at chip-scale for the first (second) run of samples fabricated. (b) Residual resistance ratio, $RRR \equiv \rho_{RT}/\rho_{4K}$ as a function of the N_2/Ar flow for samples prepared in the first and second run of fabrication.

of the samples decreases as the temperature decreases. In contrast, for samples sputtered with gas fractions above 10%, the $RRR < 1$ showcasing the opposite trend. The change from $RRR > 1$ to $RRR < 1$ is compatible with an increase of the incorporated impurities which can produce an increase in disorder and/or a change in grain size [Fic71]. Similar behavior has been observed in grAl films [Bac+13; Lev+19].

5.3.1 Temperature-resistance curves

In the process of cooling down/warming up the dilution refrigerator, we measure the samples continuously. In Fig. 5.2, we present a selection of temperature versus sheet resistance $R_s(T)$ curves obtained for samples prepared with different N_2/Ar flows. The data is normalized with respect to the room-temperature sheet resistance to visualize the different behavior. Similarly to what we mentioned for the RRR study, we distinguish three different regimes:

- *Metallic-like*: in this range, the $R_s(T)$ curve decreases monotonically with temperature ($dR_s/dT > 0$). Samples sputtered with flows between 0% and 8.33% show $R_s(T)$ with positive slope. In terms of resistivity this range of flows corresponds to samples with $\rho_{RT} \lesssim 76\,\mu\Omega\,\text{cm}$.

- *Intermediate regime or transition point*: the change of resistance in temperature is very small or negligible ($\mathrm{d}R_\mathrm{s}/\mathrm{d}T \sim 0$). We observe this behavior for the 10% samples prepared in both runs of fabrication with resistivities between $\rho_{RT} \sim 115 - 151\,\mu\Omega\,\mathrm{cm}$.

- *Insulator-like*: the samples show an increase of resistance with decreasing temperature ($\mathrm{d}R_\mathrm{s}/\mathrm{d}T < 0$). In this regime, we distinguish two distinct behaviors. For samples sputtered with 11.67% of N_2/Ar the increase in resistance is monotonic or quasi-linear. On the other hand, samples fabricated with 13.3% of N_2/Ar have a non-monotonic or exponential-like increase of resistance with decreasing temperature.

The $R_\mathrm{s}(T)$ behavior observed for NitrAl films is consistent with the different regimes previously reported in granular superconductors [Deu06] and with a superconductor-insulator transition (SIT). For granular superconductors, the change from metallic behavior to insulator behavior is explained by the dominant process at each resistivity level. For low resistivity samples, $\rho \lesssim 100\,\mu\Omega\,\mathrm{cm}$, the mean free path is similar to the grain size and the scattering is dominated by grain boundaries. For high resistivity samples, the exponential-like increase of resistivity with decreasing temperature is explained by an increase in the Coulomb repulsion energy, which gives the energy needed to transfer an electron from one grain to another [Lev+19]. In the following section, we provide more details on the different mechanisms that shape the $R_\mathrm{s}(T)$ curves and critical temperatures of granular films.

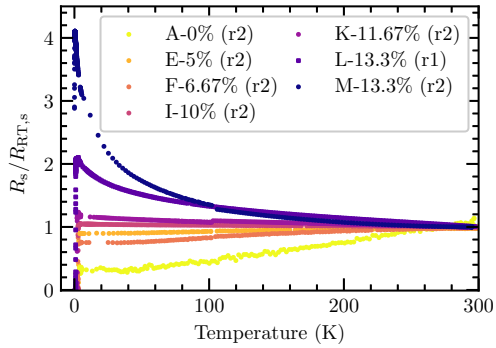

Figure 5.2: Sheet resistance as a function of temperature for different NitrAl samples fabricated at different N_2/Ar % and different runs (r1, r2). The sheet resistance is normalized respect to the room-temperature sheet resistance of the samples.

5.3.2 Critical temperature of NitrAl

We measure the superconducting transition and critical temperatures for all the samples reported in Table 5.1, except for the one sputtered in the second run of fabrication (r2) with 13.3% of N_2/Ar fractional flow and $\rho_{\mathrm{RT}} = 2177.01 \pm 0.03\,\mu\Omega\,\mathrm{cm}$. With the latter, we observe a drop in resistance below 0.5 K, but the sample does not reach the superconducting state above 19 mK. This result is probably an indication that the SIT sits close to the 13.3% N_2/Ar process flow. In Fig. 5.3 (a), we show a close-up for a selection of superconducting transition curves grouped according to their critical temperatures and resistivities. In all three panels, the transitions are sharp and span up to tens of mK. This is in contrast with grAl, where the superconducting transition significantly broadens with increasing film resistivity, but at low resistivity the transition is also sharp, corresponding to the left of the dome [Lev+19].

From the $R_{\mathrm{s}}(T)$ curves, we obtain the critical temperatures of all samples. We define T_{c} as the point in which the resistance drops to 50% of its onset value. Since our datasets are noisy, we follow two different approaches to determine T_{c} and use the difference between them to evaluate the error. The first one is what we call the *linear method*. We take the slope of the curve before the transition and we calculate the temperature point where the resistance is half the value given by the linear fit. The second method consists of fitting the transition to a modified hyperbolic curve. As a last check, we compare the results with the *derivative method*. We calculate $\mathrm{d}R_{\mathrm{s}}/\mathrm{d}T$ and we determine T_{c} as the inflection point [Poo+14].

Fig. 5.3 shows the critical temperatures measured for different NitrAl samples as a function of (b) the fractional N_2 flow and (c) room-temperature resistivity. We observe an initial increase in T_{c} with increasing N_2 flow with a maximum value of 3.38 ± 0.01 K for the 5% sample prepared in the first run of fabrication. Similar values of enhanced critical temperature have been observed in grAl films deposited on cold substrates [Des+25]. Where samples grow significantly smaller grains (~ 2 nm) resulting in maximum $T_{\mathrm{c}} \sim 3.2$ K. For fractional flows beyond 5%, the critical temperatures start to decrease. Samples sputtered with flow fractions beyond 11.67% the critical temperature falls below the one measured for Al (1.25 ± 0.01 K). The overall T_{c} curve has a dome shape-like distribution both in flow and resistivity, except for samples *F* and *G*. These samples display a relatively low T_{c} and room-temperature resistivity ρ_{RT} compared to the overall trend. The differences could come from a different nitrogen incorporation in this regime. However, a more in depth characterization of the microscopic structure of the material is required to properly assess this point.

The different areas of the T_{c} plot described above are in agreement with the *metallic*, *intermediate* or *transition point*, and *insulator* regimes proposed in the previous section. Indeed, from Fig. 5.3 we can determine that the insulator-like

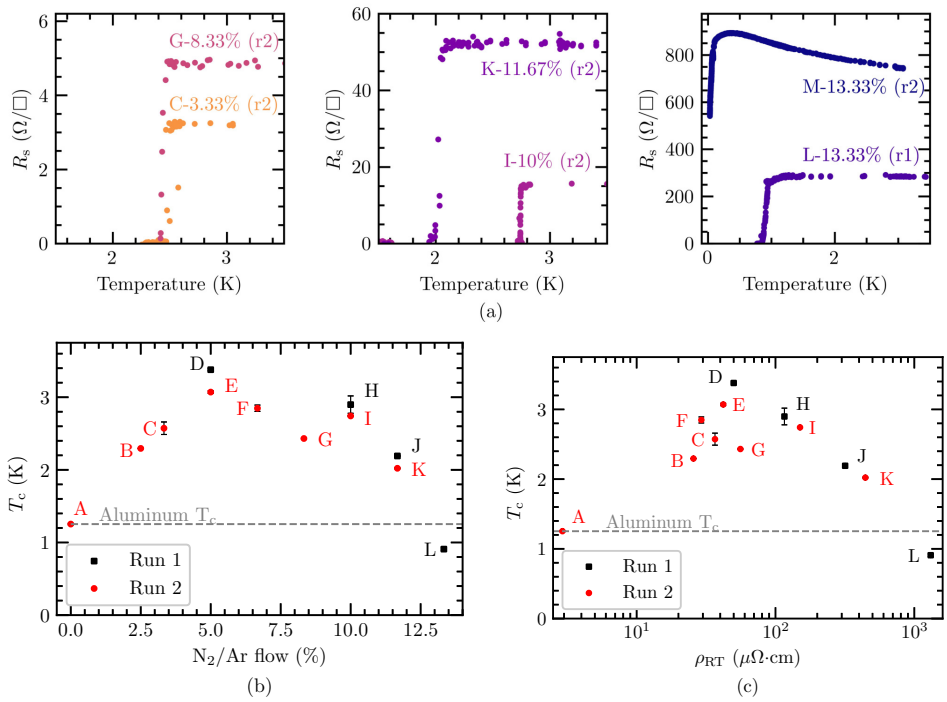

Figure 5.3: (a) Sheet resistance as a function of the temperature $R_s(T)$ near the metal-to-superconductor transition for a selection of samples. The samples are grouped according to the region in the T_c plot. Critical temperatures of NitrAl as a function of (b) N_2 fractional flow and (c) resistivity of the sample. The gray dashed line indicates the critical temperature of Al as a reference.

regime starts at the 10% sample. Likely, mechanisms such as the disorder or localization of the wavefunction are responsible for the connection between T_c and ρ_{RT} in NitrAl [Gan+10].

The dome-shape critical temperature curve and the different regimes of $R_s(T)$ have also been observed and studied in grAl films [Bac+13]. According to [Lev+19], the behavior of grAl in the different regimes is a result of a competition between three different energy scales: the phase stiffness (J), the Coulomb repulsion E_C and the superconducting gap (Δ). For low resistivity samples, ($\rho_{RT} < 100\,\mu\Omega\,\mathrm{cm}$), where the grains are well-coupled, the condensate forms in one waveform with a unique phase. In this regime, the phase stiffness is orders of magnitude above E_C and Δ. As the resistivity increases and we reach the maximum of the superconducting dome, the dominant energy is the Coulomb

repulsion ($J < E_C$). Beyond this point, phase fluctuations develop on the material and T_c decreases until the superconductor-insulator transition is reached for $J \sim \Delta$. Although the microscopic structure of NitrAl is yet unknown, we can draw a parallelism with the description given for grAl. In the case of 100 nm thick NitrAl, the different regimes are characterized by room-temperature resistivity of $\rho_{RT} \lesssim 40\,\mu\Omega\,\text{cm}$ for the well-coupled grains, $\rho_{RT} \sim 50\,\mu\Omega\,\text{cm}$ at the maximum of the superconducting dome and $\rho_{RT} > 1000\,\mu\Omega\,\text{cm}$ at the superconductor-to-insulator transition.

From theoretical predictions [Gan+10], one expects the superconductor-to-insulator transition to occur for resistance per square near the so-called resistance quantum $R_Q = h/(2e)^2 \sim 6.4\text{k}\Omega$ [Jae+89; Gan+10; Lev+19]. Unlike other granular materials, in NitrAl we identify the suppression of superconductivity for samples with $R_{4K,s} = 700.8 \pm 0.9\ \Omega/\square$ which is almost an order of magnitude below R_Q. More samples prepared in different conditions and thicknesses are needed to properly assess this boundary.

In some $R_s(T)$ measurements, we observe an anomalous resistance peak appearing before the superconducting transition. In Fig. 5.4, we present the resistance as a function of the temperature for different four-probe configurations. The samples are wirebonded following a standard Van der Pauw four-probe configuration (A and B) and we repeat the $R_s(T)$ measurement rotating the voltage/current probing. Another measurement is performed with an in-line four-probe configuration. We observe an increase in resistance of $20 - 30\%$ before the superconducting transition for the most resistive configuration (in both cases labeled as A). We can attribute the origin of the peak to local variations of the critical temperature T_c and current redistribution inside the sample. In fact, in our measurements, we observe differences in T_c of approximately 0.01 K depending on the configuration used to probe the sample. Similar observations have been reported for disordered and homogeneous thin film superconductors measured by the four-probe technique [Pol+23; Vag+93].

Kinetic inductance estimate

Kinetic inductance is widely exploited in the field of superconducting quantum devices. In the past decades, it has gained interest for applications in quantum sensing, quantum computing or amplification devices. Well known examples of the use of materials with high kinetic inductance include microwave kinetic inductor detectors (MKIDs) [Doy+08; Ulb+21; Maz05] or fluxonium qubits [Grü+19; Rie+23; Haz+19]. In view of the possible interest in using NitrAl for superinductive applications, we give an initial estimate of the kinetic inductance of the flims fabricated in this work.

Similarly to grAl, we can estimate the sheet kinetic inductance ($L_{k,s}$) of the different films by using the normal-state resistivity (ρ_{4K}) and the critical temper-

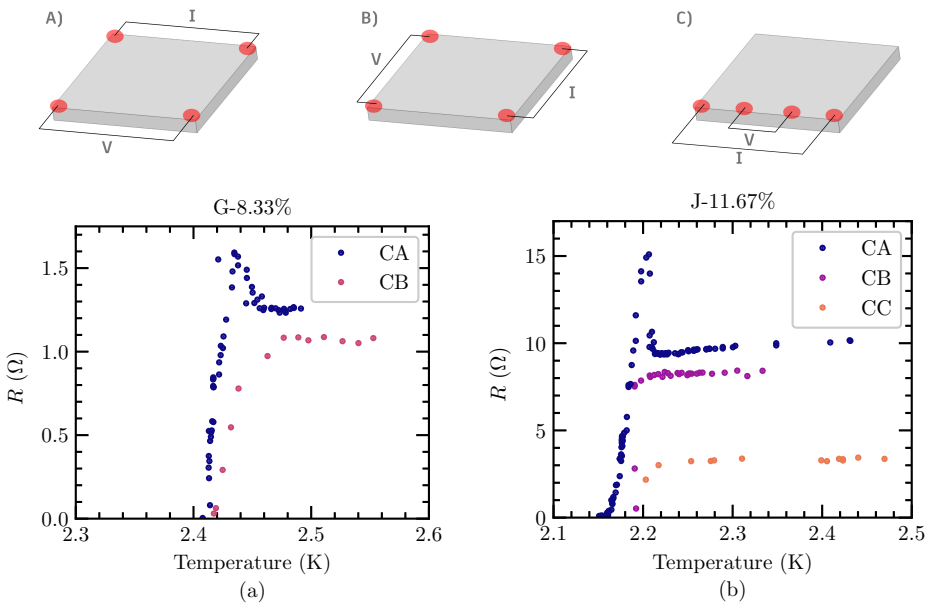

Figure 5.4: Top: schematics displaying the different contact configurations (A, B and C) used to test the anomalous peak. Bottom: resistance versus temperature for NitrAl (a) 8.33% in two different 4-probe configurations and (b) 11.67% in three different 4-probe configurations.

ature (T_c). $L_{k,s}$ can be estimated by the Mattis-Bardeen formula for the complex conductivity in the local, dirty limit at low frequency ($hf \ll k_B T$) and in the low-temperature limit ($T \ll T_c$) [Rot+16]. The resulting expression (2.1) has been already introduced in Ch. 2 to estimate the kinetic inductance of grAl,

$$L_{k,s} = 0.18 \frac{\hbar R_{4K,s}}{k_B T_c}, \tag{5.1}$$

where $R_{4K,s}$ is the normal-state sheet resistance measured at 4 K, T_c is the critical temperature of the film and k_B is the Boltzmann constant.

In Fig. 5.5, we provide the estimated kinetic inductance as a function of the process flow (a) and resistivity (b), and in Table 5.1 we provide the complete list of parameters measured for the different NitrAl samples studied in this work. The estimated sheet kinetic inductance for NitrAl films ranges between 1.31 ± 0.01 pH/□ (0% N_2) and 422.48 ± 8.22 pH/□ (13.3% N_2). The resulting values postulate the most resistive samples of NitrAl as possible candidates for superinductive

Table 5.1: Summary of NitrAl properties measured for the samples prepared in this work: sample label, N_2/Ar fractional flow (%), fabrication run number, nominal thickness t, critical temperature T_c, resistivity at room temperature ρ_{RT}, and at 4 K ρ_{4K}, estimated sheet kinetic inductance $L_{k,s}$ using Eq. (2.1).

Sample	N_2/Ar (%)	Run	t (nm)	T_c(K)	ρ_{RT} ($\mu\Omega$ cm)	ρ_{4K} ($\mu\Omega$ cm)	$L_{k,s}$ (pH/□)
A	0 - Al ref.	2	100.0	1.25 ± 0.01	2.92 ± 0.04	1.05 ± 0.05	0.12 ± 0.01
B	2.50	2	100.0	2.30 ± 0.01	25.66 ± 0.03	21.82 ± 0.03	1.31 ± 0.01
C	3.33	2	100.0	2.57 ± 0.08	36.67 ± 0.03	32.28 ± 0.11	1.72 ± 0.06
D	5.00	1	100.0	3.38 ± 0.01	50.01 ± 0.03	46.27 ± 0.03	1.88 ± 0.01
E	5.00	2	100.0	3.07 ± 0.02	42.07 ± 0.13	37.50 ± 0.04	1.68 ± 0.01
F	6.67	2	100.0	2.85 ± 0.04	29.25 ± 0.03	22.17 ± 0.03	1.07 ± 0.02
G	8.33	2	100.0	2.43 ± 0.01	55.88 ± 0.03	48.50 ± 0.03	2.74 ± 0.01
H	10.0	1	83.0	2.89 ± 0.12	115.97 ± 0.16	115.63 ± 0.03	6.61 ± 0.27
I	10.0	2	100.0	2.74 ± 0.01	150.26 ± 0.03	156.91 ± 0.03	7.88 ± 0.01
J	11.67	1	97.1	2.19 ± 0.01	317.52 ± 0.03	370.11 ± 0.03	23.91 ± 0.08
K	11.67	2	100.0	2.02 ± 0.01	444.13 ± 0.03	458.59 ± 0.03	35.30 ± 0.10
L	13.33	1	94.6	0.91 ± 0.02	1312.25 ± 0.03	2641.66 ± 0.05	422.48 ± 8.22
M	13.33	2	100.0	-	2177.01 ± 0.03	7008.47 ± 0.03	-

applications in superconducting quantum circuits. Nonetheless, the sheet kinetic inductance obtained for NitrAl films is still below the highest ones achieved in grAl $\gtrsim 1$ nH/□ [Grü+18; Zha+19; Gle+20]. NitrAl films of different thicknesses and prepared under different deposition conditions must be studied to give a proper comparison of L_k against other superinductors.

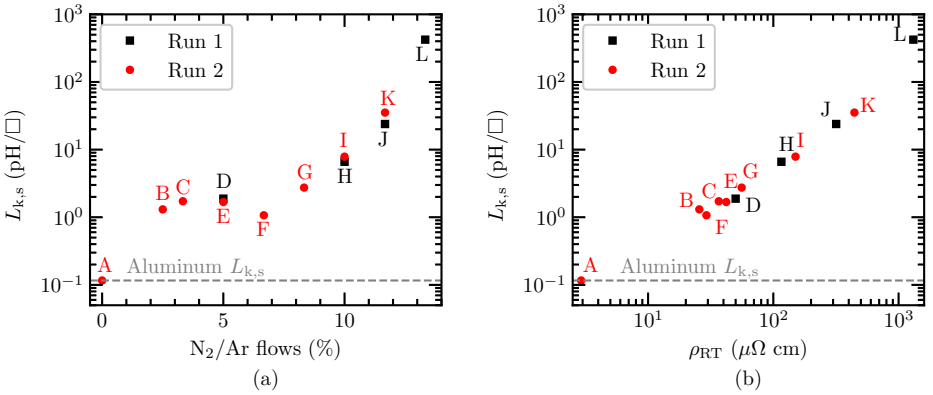

Figure 5.5: Estimated sheet kinetic inductance using Eq (5.1) for different N_2/Ar fractional flows (a), and as function of room-temperature resistivity ρ_{RT} (b).

5.3.3 Current and magnetic field response

We conclude the characterization of the low-temperature properties of NitrAl thin films with measurements of the critical current (I_c) and magnetic field response (B_c). Note that the measurements are performed on thin films without device pattern; thus the results shown below provide a qualitative understanding of I_c in NitrAl films.

The critical currents are measured at base temperature by slowly increasing the current applied to the sample. We take I_c as the current for which the sample switches to the normal state. In Fig. 5.6, we show the measured critical currents as a function of (a) the nitrogen partial flow and (b) the resistivity of the samples. We observe an initial increase in I_c with increasing flow (resistivity) with a maximum $\sim 90\,\mathrm{mA}$ for the sample 5% fabricated in the second run (r2). For increasing flow (resistivity) we observe a quasi-monotonic decrease of I_c reaching values below the Al for samples in the range of 8.33%-13.33%. Lower critical currents might be an indication that the superconducting state is weakening due to an increase in disorder or localization.

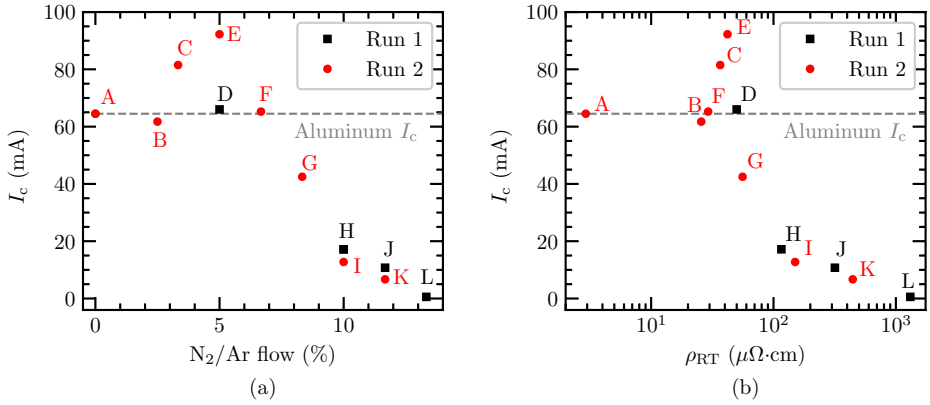

Figure 5.6: Critical currents measured for NitrAl thin films at base temperature ($T \simeq 25\,\mathrm{mK}$) as a function of nitrogen partial flow (a), and room-temperature resistivity (b).

The magnetic field response of the samples is measured in a micro-SQUID setup [Wer+95] where the field is limited in each direction to $B_z = 0.1\,\mathrm{T}$, $B_y = 0.7\,\mathrm{T}$ and $B_x = 1.4\,\mathrm{T}$. The resistance of the sample is extracted via direct I-V measurements or in a lock-in configuration.

Figure 5.7 shows the out-of-plane $B_{z,c}$ (a) and in-plane $B_{x,c}$ (b) fields for which the superconducting state of NitrAl is broken as a function of the tem-

perature (see the schematic inset for a representation of the field direction). For the Al film (0%) out-of-plane fields of 0.01 T and in-plane fields of 0.06 T are enough to break superconductivity at base temperature. The reported values are consistent with the literature on Al thin films [Tin04; Cap+65]. For the subset of NitrAl samples, the B_z field applied is not enough to break superconductivity at base temperature and an increase of temperature is needed to observe the effects of the field. In the three cases presented the resilience to the field is much larger than the one of Al. NitrAl samples show an increasing resilience to in-plane magnetic field with increasing percentage of N_2 (see Fig. 5.7 (b)). If we compare the results with Al, the 3.33% sample shows an increase of almost a factor 7 in $B_{x,c}$. For the other two NitrAl samples studied (6.67% and 10%), the range of the magnet in B_x is not enough to break superconductivity and an increase in temperature is needed to observe the effects of the field. These results are consistent with studies performed on other granular and disordered superconductors [Bac+15; Abe+67]. An increase of room-temperature resistivity and disorder is generally accompanied by an increase in critical magnetic field. In Fig. 5.8, we show a set of IV curves corresponding to sample 10% r2 obtained

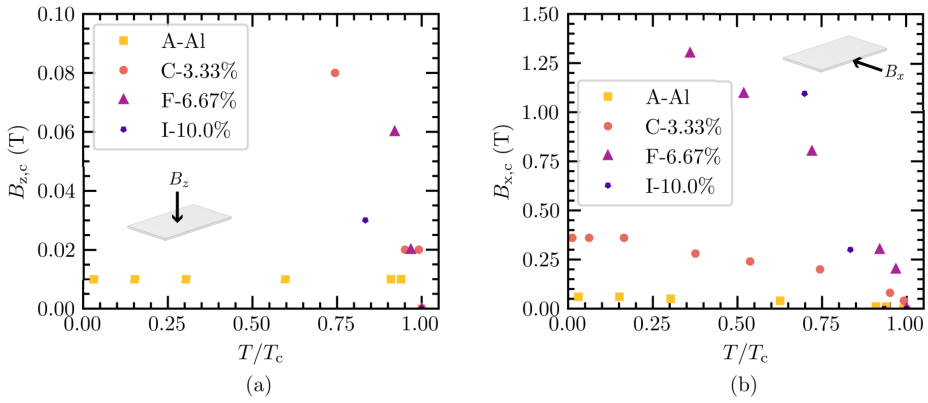

Figure 5.7: Magnetic field dependence with the superconducting state for a selectrion of NitrAl samples as a function of the temperature. (a) Out-of-plane (perpendicular to the sample) magnetic field $B_{z,c}$ for which the superconductivity of the sample is broken. (b) In-plane (parallel to the chip) magnetic field $B_{x,c}$ for which the superconducting state of the sample is broken. The temperatures have been normalized respect to the critical temperature of each NitrAl sample.

at different temperatures and at different in-plane magnetic fields B_x. We observe a non-linear gradual increase in resistance near the switching current (see

shadowed region). This effect is more pronounced in the third panel, were the change in the IV trend is significantly smoother for $B_x = 0.2\,\mathrm{T}$. We can relate this characteristic behavior happening for resistive NitrAl samples with type-II superconductors. In type-II superconductors, when a magnetic field above the first critical field H_{c1} and below the second critical field H_{c2} is applied, flux lines can penetrate the superconducting regions. In these regions, superconducting currents are generated in the form of cortices carrying a quantum of flux that prevent flux lines to fully destroy superconductivity [Por15]. In this context, for large enough applied fields, a vortex flow is induced by the applied currents producing the gradual increase in resistance observed near the switching current. Given that the description of NitrAl films under magnetic fields seems to match type-II superconductor properties, we can identify the field $B_\mathrm{c} = \mu_0 H_{c2}$ as the observed field where superconductivity is destroyed. The newest observations in the work from [Lee+24] on the IV characteristics of NitrAl films under magnetic fields reveal the typical vortex dissipation in a wider range of samples confirming the classification of NitrAl samples as type-II superconductors.

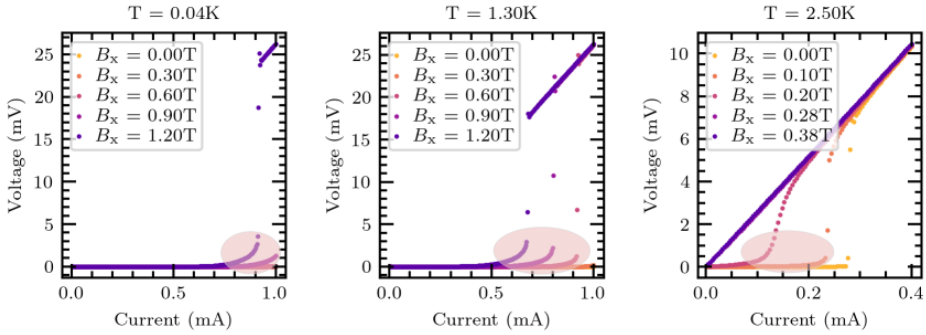

Figure 5.8: IV characteristics obtained at different temperatures and at different magnetic fields for the 10% NitrAl sample. An increasing value of magnetic field is indicated with a darker color. The shadowed areas indicate the vortex flow region.

5.4 Resonator characterization

So far, we have presented the electrical and magnetic properties of NitrAl at room temperature and at low temperature. We have seen that the high T_c, relatively high $L_{\mathrm{k,s}}$ and resilience to magnetic fields can be of interest for applications in superconducting quantum circuits. However, these are not sufficient characteris-

tics to make a material suitable to fabricate superconducting quantum circuits. First of all, we need to be able to integrate this material into the qubit fabrication processes. In other words, NitrAl should be compatible with standard lithography procedures and, specially, with Josephson junction fabrication. Another key element of NitrAl are the losses. A lossy material will have a direct impact on qubit decoherence and resonator quality. One way to quantify and determine the origin of the losses of NitrAl is by fabricating resonators. By measuring them under different powers, temperatures and frequencies, it is possible to determine (up to a certain degree) the origin and type of losses that dominate [McR+20].

In this section, we present the first steps towards the characterization of patterned devices in NitrAl. As we will show below, the designs are not optimized for loss characterization, thus only a qualitative comparison with Al can be established.

5.4.1 Sample preparation

Samples were prepared on intrinsic Si substrates. We choose NitrAl 5% and 0% with 100 nm nominal thickness, where 0% is used as a control sample. The sputtering process is performed on substrates previously cleaned in acetone and isopropanol (IPA). Note that for this initial test, no HF dip is performed prior to deposition to remove the surface oxides from Si [Wis+10; Ear+18]. The devices are patterned using optical lithography and NitrAl is etched with reactive ion etching (RIE)[1].

We use the optical mask designed at IFAE, initially intended for studies of the Al penetration depth [Lóp+25]. The 2 cm × 2 cm cell contains four copies of the same device. Each device consists on three feedlines with three different types of resonators that we label as 'M' (medium), 'L' (large) and 'DE' (distributed element). 'M' and 'L' are lumped-element resonators where the main design difference is the width of the meander and fingers of the interdigitate capacitor. The number of meanders in the inductor is kept equal for both designs and the capacitance is adjusted so that resonances lie around 7 GHz for Al. Figure 5.9 shows the device design (left) and a zoomed-in image of the different resonator designs present on the chip.

Due to fabrication problems with "M" and "DE" resonators, we only use "L" lumped element resonator designs for our study. The etching recipe used was the same as the one for bare Al, but for distributed resonators and "M" resonators, which have smaller dimensional features, it requires some tuning up. These designs are not optimized to test the quality of the material, but serve as an initial characterization of devices fabricated in NitrAl. In the following

[1] The etching rate characterization was carried out by cleanroom technicians at CNM.

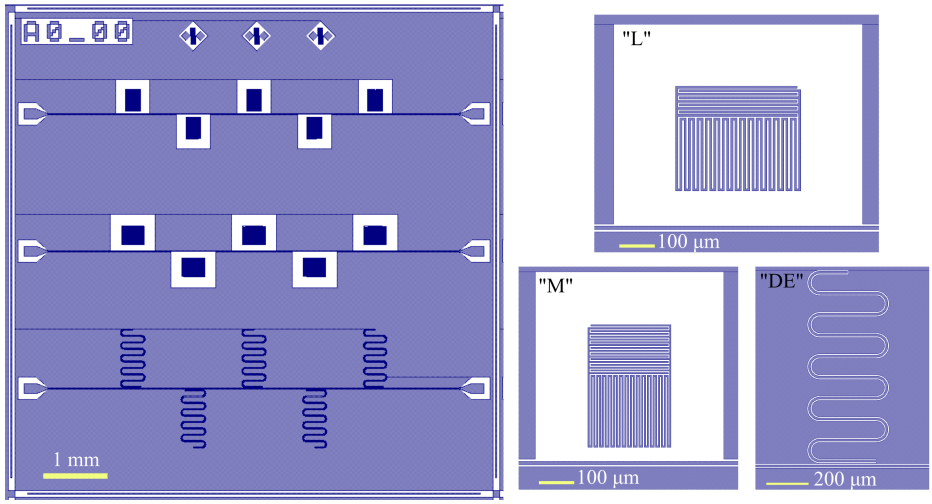

Figure 5.9: Resonator device design presented in [Lóp+25]. The three different feedlines contain the resonators presented on the right panels. L stands for large, M for medium and DE for distributed element.

sections, we provide the measurements of "L" resonators fabricated in Al and NitrAl 5%.

5.4.2 Resonator measurements

The NitrAl and Al resonators are packaged and mounted on the base temperature plate of a dilution refrigerator. Measurements are performed in transmission for varying input powers. Figure 5.10 shows the transmission measurement $|S_{21}|$ for the two higher frequency resonators fabricated in Al (a) and NitrAl (b). There is a slight difference in the magnitude of the dip in $|S_{21}|$, being smaller for NitrAl. The second distinctive element is the difference in resonance frequency. Resonators fabricated in NitrAl have resonance frequencies $\sim 1.5\,\mathrm{GHz}$ lower than those made with Al. This is a result of the larger kinetic inductance of NitrAl films. We can use the difference in resonance frequency to give an estimate of the $L_{\mathrm{k,s}}$ for NitrAl 5%. Using the simulated geometric inductance of the resonator $L_g \simeq 1.9\,\mathrm{nH}$ and the total kinetic inductance $L_{\mathrm{k}} \simeq 0.127\,\mathrm{nH}$ estimated using $L_{\mathrm{k,s}}$ for Al in Table 5.1, we can calculate an estimate for the kinetic inductance of NitrAl 5%,

$$L_{\mathrm{k}}^{\mathrm{NitrAl}} = (L_{\mathrm{g}} + L_{\mathrm{k}}^{\mathrm{Al}}) \left(\frac{f_r^{\mathrm{Al}}}{f_r^{\mathrm{NitrAl}}} \right)^2 - L_{\mathrm{g}}, \tag{5.2}$$

where f_r^{Al} and f_r^{NitrAl} are the measured resonance frequencies of Al and NitrAl resonators, respectively. Using $f_r^{\mathrm{Al}} = 7.64\,\mathrm{GHz}$ and $f_r^{\mathrm{NitrAl}} = 6.11\,\mathrm{GHz}$, we obtain $L_{\mathrm{k}}^{\mathrm{NitrAl}} \simeq 1.3\,\mathrm{nH}$ and $L_{\mathrm{k,s}}^{\mathrm{NitrAl}} \simeq 1.21\,\mathrm{pH}/\square$, which is close to the value given in Table 5.1 for the 5% sample. The difference comes mainly from the fact that we have used the nominal design values and nominal number of squares to estimate $L_{\mathrm{g}} \simeq 1.8\,\mathrm{nH}$ and intrinsic Si as a substrate. A proper estimate of the real device dimensions and the corresponding adjusted simulation is needed to obtain more accurate results.

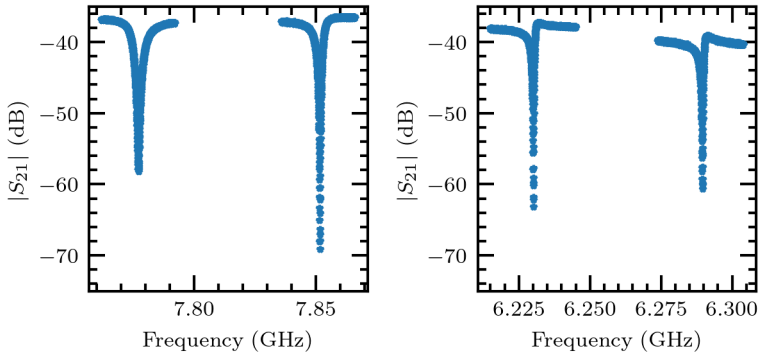

Figure 5.10: Transmission magnitude $|S_{21}|$ for the two resonators at higher frequency out of the five present in the chip measured at $P_{in} \simeq -110\,\mathrm{dBm}$. Panel (a) shows the resonances for Al resonators and (b) NitrAl resonators.

In order to evaluate the quality of NitrAl films, we extract the internal quality factor of the resonators and its dependence with respect to driving power. The internal quality factor gives a performance metric of the resonator, and it can be extracted by fitting the resonator response to the equation proposed in [Pro+15],

$$S_{21} = ae^{i\alpha}e^{-2\pi i f\tau}\left[1 - \frac{(Q_l/|Q_c|)e^{i\phi}}{1 + 2iQ_l(f/f_r - 1)}\right], \tag{5.3}$$

where the first factor describes the environment and the second the ideal resonator response. In this expression, f_r refers to the resonator resonance frequency, f is the probe frequency, Q_l denotes the loaded quality factor, $|Q_c|$ is the absolute value of the coupling quality factor and ϕ is used to quantify any impedance mismatch in the line. The variables related to the environment are a an amplitude, α an extra phase shift and the electronic delay τ. We use the modified fitting routine developed in [Lóp+25; Lóp24], which uses the same circle-fit idea but it

is based on the package *minuit*[2].

In Fig. 5.11, we show the extracted internal quality factors as a function of the input power. The input power is estimated from the total attenuation in the setup considering that inside the fridge we had $\sim 50\,\mathrm{dB}$. We show a selection of all five resonators present in the chip. The resonators are designed to be over-coupled to the line which makes the extraction of Q_i unreliable. Consequently, we discard the resonators that have an error comparable to the estimated value of Q_i. The resonators fabricated in Al have Q_i values at low powers ranging

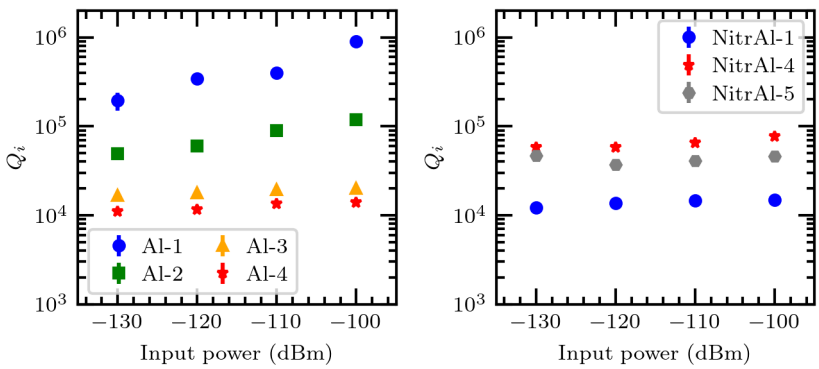

Figure 5.11: Internal quality factors Q_i extracted by fitting to Eq. (5.3) as a function of the input power for (a) Al and (b) NitrAl resonators. The labels in the legend indicate the resonator fitted. 1 corresponds to the lowest frequency resonator and 5 to the highest frequency resonator.

from $Q_i^{\mathrm{Al}} = 1.1\mathrm{e}4$ to $Q_i^{\mathrm{Al}} = 2\mathrm{e}5$. In the case of NitrAl, the values range between $Q_i^{\mathrm{NitrAl}} = 1.2\mathrm{e}4$ and $Q_i^{\mathrm{NitrAl}} = 5.8\mathrm{e}4$. Although in both resonator types the internal quality factors at low powers are on a similar level, the values are significantly lower for Al resonators fabricated on intrinsic Silicon [Ear+18]. The low internal quality factors and the large spread of values is probably a consequence of the design and fabrication process. On the one hand, resonators are over-coupled to the line, which complicates the reliable extraction of Q_i and can explain the spread of values. On the other hand, it is well-known that one of the limitations of resonators at low temperatures are two-level systems (TLS) defects arising in oxides growing between substrate-metal and metal-air interfaces. The fabrication did not include a step to remove substrate surface oxides prior to deposition, which could explain the low internal quality factors measured in this

[2]https://scikit-hep.org/iminuit/

work. Besides the spread of Q_i values, both Al and NitrAl resonators display a slow increase of Q_i in power with the exception of resonators 1 and 2 fabricated in Al. The increase of Q_i with increasing power is consistent with a saturation of TLS in the material and the presence of oxides in metal interfaces. For high enough powers, one expects a drop in Q_i [Sag+11], which we did not observe in our samples due to the relatively low power range used. In order to see the latter effect, we should target input powers of the order of $\sim -50\,\mathrm{dBm}$.

This results correspond to the first batch of resonators fabricated in NitrAl. Considering that the fabrication is yet to be improved, it is already a good sign that NitrAl and Al resonators display comparable internal quality factors. Future studies could consider improved resonator designs (preferably distributed-type element) with lower coupling to the feedline. Furthermore, a proper substrate cleaning procedure must be introduced into the fabrication process to remove surface oxides and reduce the impact of TLSs in substrate-metal interfaces. For example, including an HF dip prior to deposition is known to improve significantly the performance of qubits and resonators [Wis+10; Ear+18]. New studies have started in this direction with the aim of quantifying systematically the losses in NitrAl films [Góm24].

5.5 Final remarks

In this chapter, we showed that nitridized Aluminum thin films can display superconductivity when fabricated under non-stoichiometric conditions. By increasing the concentration of nitrogen during the fabrication process, one can tune the room-temperature resistivity and the superconducting properties of the films.

Similarly to grAl, we observed an enhanced critical temperature for increasing nitrogen flows with a maximum displayed at $T_\mathrm{c} = 3.38 \pm 0.01\,\mathrm{K}$ for a sample prepared with 5% of N_2/Ar fractional flow. Besides an enhanced critical temperature, NitrAl films display different resistance versus temperature behaviors distinguishing between a metallic, intermediate, and insulator regime. Even though the microscopic nature of the material is yet to be studied, we could find parallelisms between the mechanism that explains the changes in $R(T)$ behavior in grAl and NitrAl films. This also led to the identification that the SIT in NitrAl films is probably close to the samples prepared with 13.3% of nitrogen flow and $4\,\mathrm{K}$ resistivity close to $\rho_{4\mathrm{K}} \sim 7000\,\mu\Omega\,\mathrm{cm}$. Finally, the initial characterization of the films under magnetic fields showed that NitrAl can be resilient to in-plane magnetic fields above $1\,\mathrm{T}$.

In addition to the study of the superconducting properties, we demonstrated the possibility of fabricating superconducting quantum devices out of NitrAl. A first batch of NitrAl resonators was compared to Al showing comparable quality factors and a shift in resonance frequency explained by the large kinetic induc-

tance. Still, the quality factors shown are below the state-of-the-art for Al. The results could be improved by designing new resonators, improving the etching process of NitrAl, and including substrate cleaning steps in the fabrication of films.

In summary, the superconducting properties reported in this work, together with the possibility of fabricating devices, make NitrAl an interesting material for quantum circuits and quantum technology applications. Future research directions include the study of superconducting properties versus NitrAl film thickness, investigation of the microstructure of the material, or elucidation of wether possible remanent AlN piezoelectricity can be a limiting factor for NitrAl resonators.

Chapter 6

Conclusions and perspectives

6.1 Conclusions

In this thesis, we have presented the study of a flux qubit-resonator system in the ultrastrong coupling (USC) regime. The main particularity of the studied device is the use of granular Aluminum (grAl), a superinductor material able to provide a large shared coupling inductance in a reduced volume. The last part of the thesis was devoted to superinductors, where we provided the characterization of a novel superconducting and superinductor material developed in IFAE consisting of Aluminum nitridization.

The study of USC in flux qubit-resonator systems has traditionally used Josephson junctions as coupling elements [Nie+10; Yos+17b; For+17]. In this work, we used grAl to provide a large and linear shared inductance between qubit and resonator. The system was designed to have a qubit with a reasonable persistent current and close to resonance with a low impedance resonator to boost the coupling into the non-perturbative USC regime. The second novelty of the design consisted of using two feedlines for independent probing of the qubit and the resonator. A development of numerical methods as well as the derivation of the different Hamiltonians was needed to provide estimates of the coupling coefficient, the spectrum of the system and the qubit emission rate.

Despite the unexpectedly low qubit persistent current, the qubit-resonator coupling was enough to enter the perturbative USC regime with $g/\omega_r \sim 0.13$. The transmission spectra of the system displayed USC features, namely a 23 MHz Bloch-Siegert shift produced by the counter-rotating terms. No significant differences were observed when probing the device either through qubit or resonator, which could be attributed to a stray coupling between qubit feedline and resonator. This preliminary results show the possibility of reaching the USC regime with low persistent current flux qubits and large shared inductors and opens the door towards new studies with coherent systems in the USC regime.

The study of nitridized Aluminum (NitrAl) films led to producing thin films displaying a large kinetic inductance, reaching in some cases hundreds of pH/□ for

a 100 nm thickness. The superconducting properties of NitrAl revealed two important characteristics: an enhanced critical temperature and a higher resilience to magnetic fields respect to Al thin films. Regarding the critical temperatures, we measured a maximum $T_c = (3.38 \pm 0.01)$ K for a sample prepared with 5% of N_2/Ar flow, which is higher than grAl prepared at similar temperature conditions. We also observed a dome shape-like distribution of the critical temperatures as a function of resistivity and process flow. The different areas of the dome distribution correlated with the temperature-resistance curves showing metallic-like, intermediate and insulator-like behavior. Measurements of the properties of NitrAl films under magnetic fields showed an enhanced resilience to in-plane magnetic fields above 1 T. Finally, first insights on the losses of NitrAl films were obtained by resonator measurements. Although this initial set of devices was not prepared to study material losses, the resonators displayed similar internal quality factors for Al and NitrAl. The enhanced critical temperature and high resilience to magnetic fields, together with the possibility of obtaining large kinetic inductance films, make NitrAl a promising material for future superconducting qubit applications.

6.2 Perspectives

6.2.1 USC experiments

The measurement of the flux qubit-resonator spectrum in the USC regime is the first step in studying coherence in USC systems. Even though the presented qubit-resonator device had a number of problems, it could still be used to test the coherence properties of the system. For instance, one could try to run standard T_1 and T_2 qubit measurements, or protocols such as the one presented in [Ree+10] to readout the state of the qubit.

The results in this thesis show the need of redesigning the qubit feedline and qubit-feedline coupling. The best approach would be to divide the design in two separate experiments to minimize stray couplings. One design could consists on a standard qubit-resonator USC experiment with a single line probing the resonator. The second device should contain one feedline coupling only to the qubit. This would allow for more flexible designs while reducing spurious crosstalk in the experiments.

Lower qubit frequencies obtained by setting larger C-shunt capacitors would significantly improve the coherence time of the designed qubit. However, this implies adapting the electronics of the set-up to be able to operate at frequencies below 4 GHz. Once the new devices are available, the next step would be to measure the spectrum and see if the spectral differences probing the resonator and the qubit are comparable to those predicted by theory [Mag+21]. With the

proposed improved design, the next step would consist on studying the coherence properties of the non-perturbative USC regime.

Similar designs with larger inductance, and thus, larger couplings, could be used to study the effects of the two-level truncation used in superconducting quantum circuits [Man+17]. The Quantum Rabi model considers a two-level atom, however, superconducting circuits have a multilevel structure. Even if they are highly anharmonic, higher energy levels can influence the spectrum for large couplings.

6.2.2 NitrAl experiments

The NitrAl study can take three different, but complimentary directions. The first one is to extend the analysis of superconducting properties to thinner films and higher magnetic fields. Thinner films might reveal even higher kinetic inductance and can provide more insights on the morphology of NitrAl. On the other hand, the study of the superconducting properties under higher magnetic fields is needed to complete the characterization of the material. Additionally, different deposition parameters can be studied, for example cold substrate deposition or different sputtering rates. If NitrAl displays a granular structure (which is yet to be analyzed), by changing the substrate temperature one can tune the growth and size of metallic grains. Similarly, the deposition rate will modify the grain and the insulating barriers.

The second direction of study should focus on the morphology and structure of the material. It is still unknown if the level of disorder in NitrAl is at the atomic or at the nm scale. A better understanding of the film structure can help explain some of the superconducting properties already observed in NitrAl films. Techniques used in granular aluminum films such as Dark Field Electron microscopy [Deu+73b], could serve to determine the grain size and distribution across the film.

Finally, since NitrAl was initially developed to be used in the context of superconducting quantum circuits, an important effort has to be devoted to the study of the losses of the material. This implies preparing new resonator designs critically coupled to the line and improve the cleaning steps used during fabrication. This includes removing oxides and possible organic residues present on the substrate. If the material is good enough, the following step would be to use it in qubit designs.

Appendix A

Fabrication recipes

Contents

This appendix contains the different recipes used to fabricate qubit devices in the QCT laboratory. The recipes are described in the same order followed to fabricate one of our superconducting qubit devices.

A.1 Substrate cleaning

The substrate is cleaned before proceeding with any lithography process. The standard procedure followed consists of rinsing the Si in Acetone and IPA respectively. To remove residual organics we perform an O_2 plasma descumming in a TePlA Gigabatch system with a recipe consisting of 5 min with 600 sccm of O_2 flow and 500 W of power.

A.2 Optical lithography

Two different optical lithography processes are used depending on the device fabricated. For qubit designs, we use a mask-less aligner with a resolution that

can go down to approximately 1 µm. On the other hand, we use a mask aligner for markers and samples dedicated to test resistance of films. In either case, the procedure is quite similar.

A.2.1 Positive photoresist - Mask aligner

For markers and DC test structures we use dedicated masks with positive photoresist. We are not allowed to reproduce the complete recipe, thus the following steps describe the key elements of the photolithography process for a double-stack resist. The double-stack provides a an undercut which is normally not present when using only positive resist. The undercut in the resist profile helps through the liftoff process since Al will not stick to the side walls during vertical evaporation. We assume that we start from a clean intrinsic Si wafer or chip:

- Dehydrate the substrate on a hotplate at 120 °C.
- Spin a first layer of LOR3A of thickness 0.6 µm and bake the resist.
- Spin a layer of HIPR 6512 of thickness of 1.4 µm and bake the resist.
- Proceed with the exposure on a Karl SUSS mask aligner.
- Postexposure bake.
- Develop the sample in OPD 4262.

A.2.2 Negative photoresist - Maskless aligner

The following procedure is used to pattern resonators, control lines and ground planes in qubit devices such as the one presented in Ch. 4. We start from a 2 cm × 2 cm intrinsic Si chip with Pd markers. We start by cleaning the surface:

- Rinse the Si chip in acetone and IPA.
- perform a plasma ashing to ensure that no organic residue is left on the surface. The recipe consists of 5 min O_2 plasma with 500 W and 600 sccm.

The following points describe the photolithography process:

- We start by depositing a Ti Prime adhesion layer. The spinning parameters are 2000 rpm for 30 s.
- Bake 2 min on a hotplate at 120 °C
- Spin coat the photoresist layer of AZ nLOF 2020 at 4000 rpm for 1 min.

- Preexposure bake on a hotplate at 110 °C for 1 min.
- Exposure on a Heidelberg Maskless aligner 150, dose 840 mJ/cm^2 and defocuss −2.
- Postexposure bake on a hotplate at 110 °C for 1 min.
- Develop for 1 min in AZ 726 MIF developer and rinse in DI water for 10 s. Blow dry with N_2 gas.

At this point, the sample is ready to be evaporated.

A.3 Vertical Al evaporation and lift-off

Chips patterned using photolithography techniques are usually metalized with a vertical Al evaporation. In our laboratory we have access to an Al dedicated e-beam evaporator from Plassys. It is customized with the machinery to perform ion argon milling and O_2 microwave plasma. The following points describe a standard Al evaporation of an *optical layer* of one of our devices:

- Load the sample in the load-lock of the Plassys and pump-down for at least 2 h. The load-lock pressure should be below 3×10^{-7}mbar and the process chamber below 5×10^{-8}mbar before proceeding with the next steps.
- Open the gate valve, close the substrate shutter and keep the sample in the loading position.
- Choose the Ti crucible and perform an evaporation at 0.2 nm/s of ~ 30 nm. This metal does not deposit on the substrate and it is only used to reduce further the pressures in the chambers.
- Let the crucible cool-down for 5 min. Then select the Al target used for vertical Al evaporation. Rotate the sample holder to the evaporation position (0° angle) and keep the substrate shutter closed.
- Ramp up the current in the metal target in increases of 100 mA every 6 min until the evaporation rate reads 0.2 nm/s. Typical current values are in the $250 - 270$ mA range for 0.2 nm/s rate. Open the substrate shutter and evaporate the desired Al thickness. Generally, for our devices we use 50 nm.
- Close the substrate shutter and slowly ramp down the current on the Al target.
- Rotate the sample holder to the loading position and unload the metalized substrate.

At this point, the sample is ready to proceed with the lift-off:

- Fill a beaker with N-Methyl-2-pyrrolidone (NMP) with a stirring magnet at the bottom. Set it on a hotplate at 75 °C[1] with a rotation of 300 rpm.
- Load the sample vertically with a Teflon holder and let it in NMP for 2 h.
- Use a pipette to remove the residual metal by gently spraying NMP on the surface of the chip.
- Remove the chip from NMP and rinse it in IPA. Afterwards, blow dry with N_2 gas.

A.4 Electron beam lithography: Josephson junction and contact fabrication

In this section, we describe the process to pattern Josephson junctions and contacts by electron beam lithography (EBL). We use two similar 30 kV Raith EBL machines, one located at CNM and the other one at ICN2. In the following lines, we provide the detailed process and parameters for each machine.

We start by cleaning the substrate:

- Clean the substrate in acetone for about 1 min and rinse it in IPA.
- perform a plasma ashing to ensure that no organic residue is left on the surface. The recipe consists of 5 min plasma with 500 W and 600 sccm. If the substrate contains Josephson junctions or other delicate structures we skip the plasma step.

A.4.1 Josephson junction fabrication

Spin coating CSAR+PMGI

After cleaning, the sample is ready to spin coat the double stack resist. We use PMGI SF7 and CSAR62. The first ensures a sufficiently large undercut for Manhattan-style junctions, while CSAR62 will determine the dimensions of the junction leads. The recipe presented below is targeted for junctions of widths below 300 nm. The following points describe the step-by-step spinning process to obtain a total resist thickness of about 870 nm:

- Spin coat PMGI at 1000 rpm for 1 min for a target thickness of 630 nm.

[1] Some research groups prefer to use 80 °C, we choose 75 °C because the available hotplate overshoots the temperature at the beginning of the process.

- Bake the sample on a hot plate for 5 min at 190 °C.
- Spin coat CSAR62 at 3000 rpm for 1 min for a target thickness of 240 nm.
- Bake the sample on a hot plate for 1 min at 150 °C.

The sample is ready to be loaded into the EBL machine. We generally make a small scratch or mark on one of the edges to help with the EBL focusing process.

EBL Patterning

At both CNM and ICN2 we have access to a 30 kV Raith EBL machine. In the former, it is a Raith 150 (TWO) and, in the latter, a Raith eLine Plus. In both we use 20 kV, an aperture of 20 µm and a 100 µm write field to pattern the Josephson junctions. For bigger structures such as pads, we use 120 µm aperture combined with a 200 µm write field. The parameters calibrated differ slightly from one machine to the other. In Table A.1 we provide a summary of the values used. Note that for bigger structures ($\gtrsim 50$ µm) patterned with 120 µm aperture we do not apply a correction in the gds design. For precise structures this should be properly calibrated.

Table A.1: Parameters for different Raith EBL machines used to pattern Josephson junctions. WF stands for write field, w is the target Josephson junction width and 1st and 2nd corr. refer to the correction in width applied on design on each junction lead.

Machine	Aperture (um)	WF (um)	Dose (μC/μm^2)	Dose factor	1st corr.	2nd corr.
Raith 150	20	100	65	1.5	$w/1.2$	$(w + 30\,\text{nm})/1.09$
Raith 150	120	200	65	2	-	-
Raith eLine	20	100	100	1.8	$w/1.2$	$w/1.3$
Raith eLine	120	200	100	1.5	-	-

Development

The sample is developed in two steps:

- Dip the sample for 60 s in CSAR developer (AR 600-546), then 30 s in CSAR stopper (AR 600-60) and finally rinse for 30 s in water and 30 s in IPA.
- Dip the sample for 55 s in a solution of 1:3 MP-351:H2O which serves to develop the PMGI layer, then rinse for 30 s in water and 30 s in IPA.

Deposition and liftoff

Before proceeding with the junction evaporation, we clean the resist residues on the areas that need to be metalized. We can perform the cleaning step either in a Tepla GIGABatch plasma asher or in situ in our Plassys evaporator. We provide the recipe details for both machines:

- Tepla GIGABatch plasma asher: O_2 flow set to 50 sccm, power 200 W, CF_4 flow set to 0 sccm for 1 min[2].
- Plassys:
  - Pump down the system below 1.5×10^{-6}mbar.
  - Tilt the sample to microwave etching position and set a planetary rotation at 5 rpm.
  - Set Ar gas, 10 sccm for 1 min.
  - Pump down the chamber for 1 min.
  - Set 10 sccm of O_2 gas with a 30 s ramp.
  - Wait 1 min and turn on the microwave source with 50 W and 2400 MHz.
  - Open the etch shutter and run the O_2 plasma for 30 s.
  - Close the shutter, set O_2 flow to zero, stop the microwave source and pump down the load-lock.

For junctions, we perform a double-angle shadow evaporation. The alignment of the substrate in the machine is quite important to obtain good yields. We use a set of custom clamps designed at IFAE to ensure a proper alignment of the chips with the sample holder. In Fig. A.1 we show an example of a sample prepared in the sample holder with the custom clamps.

The Manhattan-style Josephson junction shadow-angle evaporation consists of the following steps:

- Load the sample in the Plassys evaporator for an overnight pump. The pressure in the load-lock chamber should reach below 1.7×10^{-7} mbar. The process chamber pressure should be below 5.0×10^{-8} mbar before proceeding to the next steps.
- Perform a Ti evaporation of 30 nm to decrease the pressure in both chambers. For this step the sample is kept in the loading position and the shutter is closed.

[2] Although we have been using 1 min for the devices presented in Ch. 4, 30 s should also be enough.

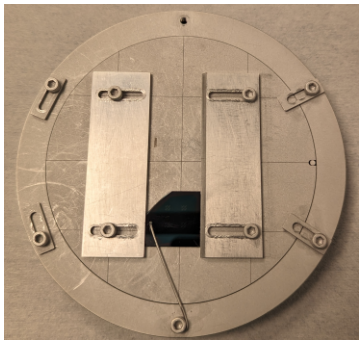

Figure A.1: Chip with test junctions prepared in the sample holder of the Plassys evaporator. The longitudinal clamps are used to align the sample to ensure a successful shadow angle evaporation.

- Set the sample holder to the evaporation position with a tilt of 55° angle while keeping the substrate shutter closed.
- Slowly ramp up the current ($\sim 100\,\mathrm{mA}$ every 6 min) in the Al crucible until the evaporation rate reaches 0.3 nm/s. Typically, we reach 0.3 nm/s for currents between $300 - 340\,\mathrm{mA}$ depending on the Al level in the pocket.
- Evaporate 36 nm of Al at 0.3 nm/s at a 55° angle. The expected thickness of this layer is 20 nm. Close the shutter and ramp down the current in the Al target.
- Bring back the stage to the loading position.
- Perform a static oxidation at 0.5 mbar, the time will depend on the desired critical current density. For $J_c \simeq 2.4\mu\mathrm{A}/\mu\mathrm{m}^2$ one should set between 10 min to 15 min.
- Rotate the sample holder 90° and tilt 55°.
- Slowly ramp up the current in the Al crucible until the evaporation rate reaches 0.3 nm/s.
- Open the substrate shutter and evaporate 69 nm of Al at 0.3 nm/s. The expected real thickness of this layer is 40 nm.
- Close the substrate shutter, bring the substrate to the loading position and ramp down the current in the Al target.

- Perform a final static oxidation at 0.5 mbar for 5 min. This step is used to saturate the oxidation of the exposed Al.

Once the sample is evaporated, we perform the lift-off. The IFAE cleanroom is equipped with a small fume-hood with an antistatic enclosure and an ion fan. To avoid electrostatic discharges on chips, we manipulate the samples on an antistatic mat while wearing antistatic bracelets. The lift-off steps are:

- Soak the sample in NMP at 75 °C for 2 h. We place a stirring magnet at the bottom of the beaker with a rotation speed set to 150 rpm for junctions.

- Use a pipette to gently squirt NMP on the sides of the chip to help the remaining pieces of Al come off.

- Rinse the sample in IPA and blow dry it with N_2

A.4.2 Fabrication of contacts

For contacts we use a different stack of resist for two main reasons. Firstly, PMGI has show to leave significant resist residues which can affect the contact between layers. Secondly, the new stack resist (MMA-PMMA) can be patterned at lower voltages (10 kV). Decreasing the voltage and dose near the Josephson junctions can decrease significantly the impact on the final resistance due to stray back-scattered electrons [Bal+24].

Spin coating MMA-PMMA

This process assumes that we start from a clean intrinsic Si chip. The following the recipe provides the details for the spin coating of a double stack resist of MMA EL6 and PMMA 950 A4:

- Deposit MMA EL6 and set a spinning rotation of 5000 rpm for 50 s.

- Bake the chip on a hot plate at 180 °C for 90 s.

- Spin coat a second layer of PMMA 950 A4 at 5000 rpm for 50 s.

- Bake the chip on a hot plate at 180 °C for 5 min.

The total resulting resist stack thickness is about 300 nm.

Patterning parameters and development

To define the patches we use a 30 kV Raith eLine Plus operated at 10 kV with an aperture of 20 µm and a 100 µm write-field. We use a base dose of 100 $\mu C/\mu m^2$ with a dose factor of 1.

The development of the sample takes only one step. We dip the sample in a solution of MIBK:IPA 1:3 for 30 s and afterwards we rinse it in IPA for 30 s. We finish the process by drying the surface with N_2 gas.

Evaporation of contacts

Before proceeding with the evaporation of the patches, we perform two cleaning steps. The first one consist of an O_2 plasma descumming. We use the same recipe as in Sec. A.4. Once the resist residues of the sample have been cleaned, we load it into the Plassys evaporator to proceed with the ion Ar ion milling. The Ar-milling is key to ensure that no oxide layer is present between the Josephson junctions, resonators and patches. We follow the steps listed below:

- Load the sample in the Plassys evaporator and pump down the load-lock below 1×10^{-6}mbar [3].
- Tilt the substrate to the etch position and set 1 rpm planetary rotation.
- Inject a flow of Ar at 6 sccm.
- Set the IBG discharge to ON with a voltage of 40 V
- Slowly ramp up the values of the IBG Beam to 400 V, 22 mA and 80 V.
- Open the EBG shutter and etch for 4 min
- Close the shutter, ramp dawn the EBG values and set the gas flow to 0 sccm.
- Pump the load-lock down to 1×10^{-7} mbar
- Evaporate 100 nm of Al with no sample tilt at a rate of 0.2 nm/s.

A.5 Granular Aluminum

In order to fabricate granular Aluminum (grAl) thin films, one should introduce an O_2 gas flow inside the chamber during the Al deposition. Note that both the

[3] We have found that flushing the chamber with O_2 gas for 2 s before proceeding with the process helps obtaining a more stable plasma. Afterwards, one should pump the chamber down to the set pressure and run an Ar flush before starting the Ar milling.

deposition rate and the O_2 gas flow will have an impact on the final properties of the film. The following points describe the steps followed in this thesis to fabricate grAl:

- Load the sample inside the Plassys evaporator and pump it down for about 2.5 h. The pressure in the load-lock should reach 2.5×10^{-7} mbar - 2.8×10^{-7} mbar.
- Perform a Ti evaporation (30 nm) to decrease the pressure in both chambers. The sample is kept in the loading position and the sample shutter is closed.
- Set an O_2 flow between 0 sccm and 0.8 sccm.
- Rotate the sample holder to the evaporation position.
- Ramp up the current until the rate is 0.2 nm/s. In our system we typically need currents between $300 - 360$ mA.
- Open the sample shutter and deposit the desired thickness of material. Close the sample shutter and stop the O_2 gas flow.
- Ramp down the current.
- Keep a current of 20 mA in the Al crucible for 1 min before reaching 0 mA.
- Unload the sample and proceed with the lift-off (if needed).

The flows of the process are chosen such that the pressure in the process chamber does not go above 5×10^{-5} mbar. Higher pressures could damage the beam filament. On the other hand, the Al pocket does not contain a liner in our evaporator[4]. This means that reaching higher evaporation above 0.2 nm/s requires currents above ~ 360 mA.

[4]Most of the reinfiltrated graphite liners tested for Al evaporation broke after few uses. Given that the broken liner is susceptible to contaminate evaporated Al, we opted to remove them.

Appendix B

Hamiltonian derivation of a three junction flux qubit galvanically coupled to an LC oscillator

In this appendix we provide the detailed derivation of the Hamiltonian for a 3-Josephson junction flux qubit galvanically coupled to an LC oscillator. We consider the coupling inductance L_c to be of the order of the resonator inductance L_R.

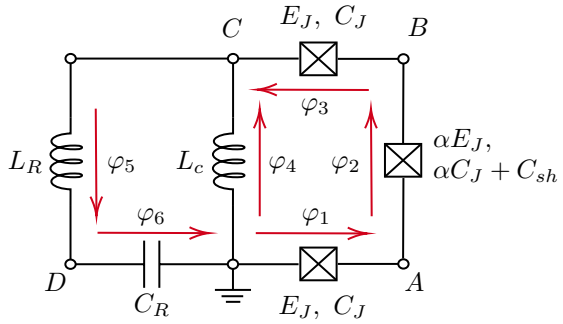

Figure B.1: Circuit of a 3-junction flux qubit galvanically coupled to an LC oscillator. The letters denote the nodes of the circuit and the arrows the spanning tree.

The equations of motion derived using the Kirchhof laws and the circuit in Figure B.1 read,

Node A:

$$\begin{aligned} &C_J\ddot{\phi}_A + \tilde{\alpha}C_J(\ddot{\phi}_A - \ddot{\phi}_B) = \\ &\quad = -I_c \sin\left(\frac{2\pi}{\Phi_0}\phi_A\right) - \alpha \sin\left(\frac{2\pi}{\Phi_0}(\phi_A - \phi_0)\right), \end{aligned} \tag{B.1}$$

Node B:

$$\begin{aligned} &\tilde{\alpha}C_J(\ddot{\phi}_B - \ddot{\phi}_A) + \gamma C_J(\ddot{\phi}_B - \ddot{\phi}_C) = \\ &\quad = -\alpha I_c \sin\left(\frac{2\pi}{\Phi_0}(\phi_B - \phi_A)\right) - \gamma I_c \sin\left(\frac{2\pi}{\Phi_0}(\phi_B - \phi_C)\right), \end{aligned} \tag{B.2}$$

Node C:

$$\begin{aligned} &\gamma C_J(\ddot{\phi}_C - \ddot{\phi}_B) = \\ &\quad - \frac{1}{L_c}\phi_C - \frac{1}{L_R}(\phi_C - \phi_D) - \gamma I_C \sin\left(\frac{2\pi}{\Phi_0}(\phi_C - \phi_B)\right), \end{aligned} \tag{B.3}$$

Node D:

$$C_R\ddot{\phi}_D = -\frac{1}{L_R}(\phi_D - \phi_C), \tag{B.4}$$

where L_c denotes the coupling inductance, L_R the resonator inductance, C_R the resonator capacitance and C_J the capacitance of the junction. The middle junction is a factor α smaller than the other two and γ is kept to consider any size mismatch between the two big junctions. We have introduced the prefactor $\tilde{\alpha} = \alpha + C_{sh}/C_J$ to account for the C_{sh} capacitor of the small junction. Using the Euler-Lagrange equation [Lan+82] and integrating the equations of motion, we can obtain the Lagrangian of the system,

$$\begin{aligned} \mathcal{L} = &\frac{C_J}{2}\left(\dot{\phi}_1^2 + \tilde{\alpha}(\dot{\phi}_4 - \dot{\phi}_1 - \dot{\phi}_3)^2 + \gamma\dot{\phi}_3^3 + \frac{C_R}{C_J}\dot{\phi}_6^2\right) + E_J\cos\left(\frac{2\pi}{\Phi_0}\phi_1\right) + \\ &+ \gamma E_J\cos\left(\frac{2\pi}{\Phi_0}\phi_3\right) + \alpha E_J\cos\left(\left(\frac{2\pi}{\Phi_0}\right)(\phi_4 - \phi_3 - \phi_1 + \phi_{ext})\right) - \\ &+ \frac{1}{2}\left(\frac{\phi_4^2}{L_c} + \frac{(\phi_4 + \phi_6)^2}{L_R}\right), \end{aligned} \tag{B.5}$$

where we have transformed to branch variables using the following relations,

$$\phi_1 = \phi_A - \phi_{gnd} = \phi_A \tag{B.6}$$
$$\phi_2 = \phi_B - \phi_A \tag{B.7}$$
$$\phi_3 = \phi_C - \phi_B \tag{B.8}$$
$$\phi_4 = \phi_C - \phi_{gnd} \tag{B.9}$$
$$\phi_5 = \phi_D - \phi_C \tag{B.10}$$
$$\phi_6 = \phi_{gnd} - \phi_D = -\phi_D \tag{B.11}$$

and applied the condition of the fluxoid quantization for the junction loop: $\phi_2 = 2\pi f - \phi_1 - \phi_3 + \phi_4$. Introducing the changes $2\pi\phi_i/\Phi_0 = \varphi_i$ and $\phi_{ext}2\pi/\Phi_0 = 2\pi f$ the Lagrangian of the system reads,

$$\begin{aligned}\mathcal{L} = &\frac{C_J}{2}\left(\frac{\Phi_0}{2\pi}\right)^2\left(\dot{\varphi}_1^2 + \tilde{\alpha}(\dot{\varphi}_4 - \dot{\varphi}_1 - \dot{\varphi}_3)^2 + \gamma\dot{\varphi}_3^3 + \frac{C_R}{C_J}\dot{\varphi}_6^2\right) + \\ &+ E_J\cos\varphi_1 + \gamma E_J\cos\varphi_3 + \alpha E_J\cos\left(\varphi_4 - \varphi_3 - \varphi_1 + 2\pi f\right) - \\ &+ \frac{1}{2}\left(\frac{\Phi_0}{2\pi}\right)^2\left(\frac{\varphi_4^2}{L_c} + \frac{(\varphi_4+\varphi_6)^2}{L_R}\right).\end{aligned} \tag{B.12}$$

Once the Lagrangian of the system is known, it is time to derive the Hamiltonian. The first step consists of obtaining the conjugate variables,

$$\begin{pmatrix} p_1 \\ p_3 \\ p_4 \\ p_6 \end{pmatrix} = \frac{\partial\mathcal{L}}{\partial\dot{\vec{\varphi}}} = \left(\frac{\Phi_0}{2\pi}\right)^2 \begin{pmatrix} C_J + \tilde{\alpha}C_J & \tilde{\alpha}C_J & -\tilde{\alpha}C_J & 0 \\ \tilde{\alpha}C_J & \gamma C_J + \tilde{\alpha}C_J & -\tilde{\alpha}C_J & 0 \\ -\tilde{\alpha}C_J & -\tilde{\alpha}C_J & \tilde{\alpha}C_J & 0 \\ 0 & 0 & 0 & C_R \end{pmatrix} \begin{pmatrix} \dot{\varphi}_1 \\ \dot{\varphi}_3 \\ \dot{\varphi}_4 \\ \dot{\varphi}_6 \end{pmatrix} \tag{B.13}$$

From the Lagrangian in equation (B.12), the conjugate variables derived in the previous step and the Legendre transformation $\mathcal{H} = \sum_i p_i\dot{\varphi}_i - \mathcal{L}$ we can obtain the Hamiltonian of the system,

$$\begin{aligned}\mathcal{H} = &\left(\frac{2\pi}{\Phi_0}\right)^2\frac{1}{2C_J}\left((p_1+p_4)^2 + \frac{1}{\gamma}(p_3+p_4)^2 + \frac{p_4^2}{\tilde{\alpha}} + \frac{C_J}{C_R}p_6^2\right) - \\ &+ E_J\cos\varphi_1 - \gamma E_J\cos\varphi_3 - E_J\cos\left(\varphi_4 - \varphi_1 - \varphi_3 + 2\pi f\right) + \\ &+ \frac{1}{2L_c}\left(\frac{\Phi_0}{2\pi}\right)^2\varphi_4^2 + \frac{1}{2L_R}\left(\frac{\Phi_0}{2\pi}\right)(\varphi_6+\varphi_4)^2.\end{aligned} \tag{B.14}$$

We can quantize the Hamiltonian by promoting the variables to quantum

mechanical operators,

$$\begin{aligned}\hat{\mathcal{H}} = &\left(\frac{2\pi}{\Phi_0}\right)^2 \frac{1}{2C_J}\left((\hat{p}_1+\hat{p}_4)^2 + \frac{1}{\gamma}(\hat{p}_3+\hat{p}_4)^2 + \frac{\hat{p}_4^2}{\tilde{\alpha}} + \frac{C_J}{C_R}\hat{p}_6^2\right) - \\ &+ E_J\cos\hat{\varphi}_1 - \gamma E_J\cos\hat{\varphi}_3 - E_J\cos\left(\hat{\varphi}_4-\hat{\varphi}_1-\hat{\varphi}_3+2\pi f\right)+ \\ &+ \frac{1}{2L_c}\left(\frac{\Phi_0}{2\pi}\right)^2\hat{\varphi}_4^2 + \frac{1}{2L_R}\left(\frac{\Phi_0}{2\pi}\right)^2(\hat{\varphi}_6+\hat{\varphi}_4)^2.\end{aligned} \tag{B.15}$$

With a simple change $\hat{n}_i = -\frac{2\pi}{\Phi_0}\frac{\hat{p}_i}{2e}$, we can give the Hamiltonian in terms of $\hat{n}_i$ and $\hat{\varphi}_i$,

$$\begin{aligned}\hat{\mathcal{H}} = &\frac{(2e)^2}{2C_J}\left((\hat{n}_1+\hat{n}_4)^2 + \frac{1}{\gamma}(\hat{n}_3+\hat{n}_4)^2 + \frac{\hat{n}_4^2}{\tilde{\alpha}} + \frac{C_J}{C_R}\hat{n}_6^2\right) + \\ &+ \frac{1}{2}\left(\frac{\Phi_0}{2\pi}\right)^2\left(\frac{\hat{\varphi}_4^2}{L_c} + \frac{(\hat{\varphi}_4+\hat{\varphi}_6)^2}{L_R}\right) - E_J\cos\hat{\varphi}_1 - \\ &+ \gamma E_J\cos\hat{\varphi}_3 - \alpha E_J\cos\left(\hat{\varphi}_4-\hat{\varphi}_1-\hat{\varphi}_3+2\pi f\right).\end{aligned} \tag{B.16}$$

Note that the crossed term containing $\hat{\varphi}_4\hat{\varphi}_6$ is the one giving the coupling between qubit and resonator.

Appendix C

NitrAl fabrication

In Table C.1, we present the fabrication parameters for NitrAl thin films presented in Ch. 5. Figure C.1 presents two NitrAl films sputtered with 15% (green surface

Table C.1: N_2 flow values and parameters used in the fabrication of NitrAl samples reported in Ch. 5. The following parameters are set constant for all samples: Ar flow = 60 sccm, power set to the target P_t = 1000 W, nominal thickness deposition t = 100 nm, Ar working pressure $P_w = 5 \times 10^{-3}$ mbar, sputtering chamber base pressure $P_b = 2 \times 10^{-7}$ mbar.

N_2(sccm)	N_2/Ar(%)	Rate(nm/s)
0.0	0.00	1.91
1.5	2.50	1.78
2.0	3.33	1.73
3.0	5.00	1.64
4.0	6.67	1.55
5.0	8.33	1.46
6.0	10.00	1.37
7.0	11.67	1.28
8.0	13.33	1.19
9.0	15.00	1.10

color) and 11.67% (silver surface color) of N_2/Ar process flow.

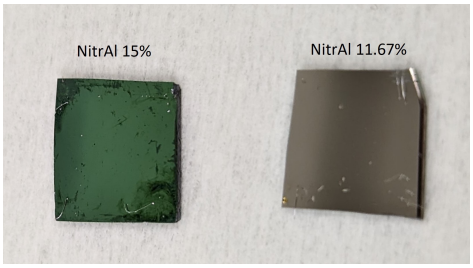

Figure C.1: Difference in color between the insulating sample (15%), and the conductive one (11.67%).

Bibliography

[Abe+66] B Abeles, Roger W Cohen, and GW Cullen. "Enhancement of superconductivity in metal films". In: *Physical Review Letters* 17.12 (1966), p. 632.

[Abe+67] B Abeles, Roger W Cohen, and WR Stowell. "Critical magnetic fields of granular superconductors". In: *Physical Review Letters* 18.21 (1967), p. 902.

[Amb+63] Vinay Ambegaokar and Alexis Baratoff. "Tunneling between superconductors". In: *Physical review letters* 10.11 (1963), p. 486.

[Ami+22] Kazi Rafsanjani Amin et al. "Loss mechanisms in TiN high impedance superconducting microwave circuits". In: *Applied Physics Letters* 120.16 (2022).

[And+17] Christian Kraglund Andersen and Alexandre Blais. "Ultrastrong coupling dynamics with a transmon qubit". In: *New Journal of Physics* 19.2 (2017), p. 023022.

[Ant+20] IV Antonov et al. "Superconducting 'twin'qubit". In: *Physical Review B* 102.11 (2020), p. 115422.

[Bac+13] N Bachar et al. "Kondo-like behavior near the metal-to-insulator transition of nanoscale granular aluminum". In: *Physical Review B—Condensed Matter and Materials Physics* 87.21 (2013), p. 214512.

[Bac+14] Nimrod Bachar and Guy Deutscher. "Spin-flip scattering in superconducting granular aluminum films". PhD thesis. Tel-Aviv University, 2014.

[Bac+15] N Bachar et al. "Mott transition in granular aluminum". In: *Physical Review B* 91.4 (2015), p. 041123.

[Bal+24] Yashwanth Balaji et al. "Electron-beam annealing of Josephson junctions for frequency tuning of quantum processors". In: *arXiv preprint arXiv:2402.17395* (2024).

[Bar+08] R Barends et al. "Contribution of dielectrics to frequency and noise of NbTiN superconducting resonators". In: *Applied Physics Letters* 92.22 (2008).

[Bas12] Jochem Baselmans. “Kinetic inductance detectors”. In: *Journal of Low Temperature Physics* 167 (2012), pp. 292–304.

[Bea+11] Félix Beaudoin, Jay M Gambetta, and A Blais. “Dissipation and ultrastrong coupling in circuit QED”. In: *Physical Review A—Atomic, Molecular, and Optical Physics* 84.4 (2011), p. 043832.

[Bel+12] MT Bell et al. “Quantum superinductor with tunable nonlinearity”. In: *Physical review letters* 109.13 (2012), p. 137003.

[Bia+06] Radoslaw Bialczak et al. “Fabrication and testing of AlN Josephson junction qubits”. In: *APS March Meeting Abstracts*. 2006, Y40–010.

[Bil+17] Alexander Bilmes et al. “Electronic decoherence of two-level systems in a Josephson junction”. In: *Physical review B* 96.6 (2017), p. 064504.

[Bil+21] Alexander Bilmes et al. “In-situ bandaged Josephson junctions for superconducting quantum processors”. In: *Superconductor Science and Technology* 34.12 (2021), p. 125011.

[Bla+21] Alexandre Blais et al. “Circuit quantum electrodynamics”. In: *Reviews of Modern Physics* 93.2 (2021), p. 025005.

[Blo+40] F Bloch and A Siegert. “Magnetic resonance for nonrotating fields”. In: *Physical Review* 57.6 (1940), p. 522.

[Bor+20] K Borisov et al. “Superconducting granular aluminum resonators resilient to magnetic fields up to 1 Tesla”. In: *Applied Physics Letters* 117.12 (2020).

[Bor27] Max Born. “Born-oppenheimer approximation”. In: *Ann. Phys* 84 (1927), pp. 457–484.

[Bou+09] Jérôme Bourassa et al. “Ultrastrong coupling regime of cavity QED with phase-biased flux qubits”. In: *Physical Review A—Atomic, Molecular, and Optical Physics* 80.3 (2009), p. 032109.

[Bra+20] Jochen Braumüller et al. “Characterizing and optimizing qubit coherence based on squid geometry”. In: *Physical Review Applied* 13.5 (2020), p. 054079.

[Bra11] Daniel Braak. “Integrability of the Rabi model”. In: *Physical Review Letters* 107.10 (2011), p. 100401.

[Bre+22] Terence M Bretz-Sullivan et al. “High kinetic inductance NbTiN superconducting transmission line resonators in the very thin film limit”. In: *Applied Physics Letters* 121.5 (2022).

[Bur+05] Guido Burkard et al. “Asymmetry and decoherence in a double-layer persistent-current qubit”. In: *Physical Review B—Condensed Matter and Materials Physics* 71.13 (2005), p. 134504.

[Cap+65] Sandor Caplan and Gerald Chanin. "Critical-field study of superconducting aluminum". In: *Physical Review* 138.5A (1965), A1428.

[Cas+10] Jorge Casanova et al. "Deep strong coupling regime of the Jaynes-Cummings model". In: *Physical review letters* 105.26 (2010), p. 263603.

[Cha+13] Josephine B Chang et al. "Improved superconducting qubit coherence using titanium nitride". In: *Applied Physics Letters* 103.1 (2013).

[Cha+22] T Chang et al. "Reproducibility and gap control of superconducting flux qubits". In: *Physical Review Applied* 18.6 (2022), p. 064062.

[Che+17] Zhen Chen et al. "Single-photon-driven high-order sideband transitions in an ultrastrongly coupled circuit-quantum-electrodynamics system". In: *Physical Review A* 96.1 (2017), p. 012325.

[Che+22] Mattia Checchin et al. "Measurement of the low-temperature loss tangent of high-resistivity silicon using a high-Q superconducting resonator". In: *Physical Review Applied* 18.3 (2022), p. 034013.

[Chi+22] Sai Pavan Chitta et al. "Computer-aided quantization and numerical analysis of superconducting circuits". In: *New Journal of Physics* 24.10 (2022), p. 103020.

[Cla+06] John Clarke and Alex I Braginski. *The SQUID handbook: fundamentals and technology of SQUIDs and SQUID systems*. John Wiley & Sons, 2006.

[Cle+01] AN Cleland, M Pophristic, and I Ferguson. "Single-crystal aluminum nitride nanomechanical resonators". In: *Applied Physics Letters* 79.13 (2001), pp. 2070–2072.

[Cór+11] Antonio D Córcoles et al. "Protecting superconducting qubits from radiation". In: *Applied Physics Letters* 99.18 (2011).

[Cot+91] W. N. Cottingham and D. A. Greenwood. *Electricity and Magnetism*. Cambridge University Press, 1991.

[Cou+12] PCJJ Coumou et al. "Microwave properties of superconducting atomic-layer deposited TiN films". In: *IEEE transactions on applied superconductivity* 23.3 (2012), pp. 7500404–7500404.

[De +09] Simone De Liberato et al. "Extracavity quantum vacuum radiation from a single qubit". In: *Physical Review A—Atomic, Molecular, and Optical Physics* 80.5 (2009), p. 053810.

[Den+23] Hao Deng et al. "Titanium nitride film on sapphire substrate with low dielectric loss for superconducting qubits". In: *Physical Review Applied* 19.2 (2023), p. 024013.

[Des+25] Aniruddha Deshpande et al. “Tuning the superconducting dome in granular aluminum thin films”. In: *Journal of Applied Physics* 137.1 (2025).

[Deu+73a] G Deutscher et al. *Granular superconducting films*. Tech. rep. Department of Physics and Astronomy, Tel-Aviv University, Ramat Aviv, Tel ..., 1973.

[Deu+73b] G Deutscher et al. “Transition to zero dimensionality in granular aluminum superconducting films”. In: *Journal of Low Temperature Physics* 10 (1973), pp. 231–243.

[Deu06] Guy Deutscher. *New superconductors: From granular to high Tc*. World Scientific, 2006.

[Dor+08] SN Dorenbos et al. “Low noise superconducting single photon detectors on silicon”. In: *Applied Physics Letters* 93.13 (2008).

[Doy+08] Simon Doyle et al. “Lumped element kinetic inductance detectors”. In: *Journal of Low Temperature Physics* 151 (2008), pp. 530–536.

[Dun+17] A Dunsworth et al. “Characterization and reduction of capacitive loss induced by sub-micron Josephson junction fabrication in superconducting qubits”. In: *Applied Physics Letters* 111.2 (2017).

[Ear+18] Carolyn T Earnest et al. “Substrate surface engineering for high-quality silicon/aluminum superconducting resonators”. In: *Superconductor Science and Technology* 31.12 (2018), p. 125013.

[Fal+19] G Falci et al. “Ultrastrong coupling probed by coherent population transfer”. In: *Scientific Reports* 9.1 (2019), p. 9249.

[Fed+10] A Fedorov et al. “Strong coupling of a quantum oscillator to a flux qubit at its symmetry point”. In: *Physical review letters* 105.6 (2010), p. 060503.

[Fic71] FR Fickett. “Aluminum—1. A review of resistive mechanisms in aluminum”. In: *Cryogenics* 11.5 (1971), pp. 349–367.

[For+10] Pol Forn-Díaz et al. “Observation of the Bloch-Siegert Shift in a Qubit-Oscillator System in the Ultrastrong Coupling Regime”. In: *Physical review letters* 105.23 (2010), p. 237001.

[For+16] P Forn-Díaz et al. “Broken selection rule in the quantum Rabi model”. In: *Scientific reports* 6.1 (2016), p. 26720.

[For+17] Pol Forn-Díaz et al. “Ultrastrong coupling of a single artificial atom to an electromagnetic continuum in the nonperturbative regime”. In: *Nature Physics* 13.1 (2017), pp. 39–43.

[For+19] P Forn-Díaz et al. “Ultrastrong coupling regimes of light-matter interaction”. In: *Reviews of Modern Physics* 91.2 (2019), p. 025005.

[For10] Pol Forn-Díaz. *Superconducting qubits and quantum resonators*. 2010.

[Fra+23] Simone Frasca et al. “NbN films with high kinetic inductance for high-quality compact superconducting resonators”. In: *Physical Review Applied* 20.4 (2023), p. 044021.

[Fra+25] Dorian Fraudet et al. “Direct detection of down-converted photons spontaneously produced at a single Josephson junction”. In: *Physical Review Letters* 134.1 (2025), p. 013804.

[Fra23] Dorian Fraudet. “Conversion spontanée de photons micro-ondes à partir d’une impureté quantique supraconductrice”. PhD thesis. Université Grenoble Alpes, 2023.

[Fri+19] Anton Frisk Kockum et al. “Ultrastrong coupling between light and matter”. In: *Nature Reviews Physics* 1.1 (2019), pp. 19–40.

[Gan+10] Vsevolod F Gantmakher and Valery T Dolgopolov. “Superconductor–insulator quantum phase transition”. In: *Physics-Uspekhi* 53.1 (2010), p. 1.

[Gao+12] Jiansong Gao et al. “A titanium-nitride near-infrared kinetic inductance photon-counting detector and its anomalous electrodynamics”. In: *Applied Physics Letters* 101.14 (2012).

[Gar+16] Luigi Garziano et al. “One photon can simultaneously excite two or more atoms”. In: *Physical review letters* 117.4 (2016), p. 043601.

[Gei+24] Simon Geisert et al. “Pure kinetic inductance coupling for cQED with flux qubits”. In: *Applied Physics Letters* 125.6 (2024).

[Gia+24] Luigi Giannelli et al. “Detecting virtual photons in ultrastrongly coupled superconducting quantum circuits”. In: *Physical Review Research* 6.1 (2024), p. 013008.

[Gle+20] Aviv Glezer Moshe, Eli Farber, and Guy Deutscher. “Granular superconductors for high kinetic inductance and low loss quantum devices”. In: *Applied Physics Letters* 117.6 (2020).

[Góm24] Ariadna Gómez del Pulgar Martínez. “Characterization of nitridized aluminium for quantum computing hardware applications”. MA thesis. Universitat de Barcelona, 2024.

[Gro+21] Peter Groszkowski and Jens Koch. “Scqubits: a Python package for superconducting qubits”. In: *Quantum* 5 (2021), p. 583.

[Grü+17] Lukas Grünhaupt et al. “An argon ion beam milling process for native AlOx layers enabling coherent superconducting contacts”. In: *Applied Physics Letters* 111.7 (2017).

[Grü+18] Lukas Grünhaupt et al. “Loss mechanisms and quasiparticle dynamics in superconducting microwave resonators made of thin-film granular aluminum”. In: *Physical review letters* 121.11 (2018), p. 117001.

[Grü+19] Lukas Grünhaupt et al. “Granular aluminium as a superconducting material for high-impedance quantum circuits”. In: *Nature materials* 18.8 (2019), pp. 816–819.

[Grü19] Lukas Grünhaupt. *Granular aluminium superinductors*. Vol. 26. KIT Scientific Publishing, 2019.

[Gry+10] Gilbert Grynberg, Alain Aspect, and Claude Fabre. *Introduction to quantum optics: from the semi-classical approach to quantized light*. Cambridge university press, 2010.

[Gup+25] Vishakha Gupta et al. “Low-loss lumped-element inductors made from granular aluminum”. In: *Physical Review Applied* 23.5 (2025), p. 054067.

[Har74] EP Harris. “Superconductivity in AlN bistable resistance devices”. In: *Applied Physics Letters* 24.10 (1974), p. 514.

[Haz+19] TM Hazard et al. “Nanowire superinductance fluxonium qubit”. In: *Physical review letters* 122.1 (2019), p. 010504.

[Ho +12] Byeong Ho Eom et al. “A wideband, low-noise superconducting amplifier with high dynamic range”. In: *Nature Physics* 8.8 (2012), pp. 623–627.

[Ihs+25] Soeren Ihssen et al. “Low crosstalk modular flip-chip architecture for coupled superconducting qubits”. In: *Applied Physics Letters* 126.13 (2025).

[Ith+05] G Ithier et al. “Decoherence in a superconducting quantum bit circuit”. In: *Physical Review B—Condensed Matter and Materials Physics* 72.13 (2005), p. 134519.

[Jae+89] HM Jaeger et al. “Onset of superconductivity in ultrathin granular metal films”. In: *Physical Review B* 40.1 (1989), p. 182.

[Jan+25] Marián Janík et al. “Strong charge-photon coupling in planar germanium enabled by granular aluminium superinductors”. In: *Nature Communications* 16.1 (2025), p. 2103.

[Jay+63] E. T Jaynes and F. W. Cummings. “Comparison of Quantum and Semiclassical Radiation Theories with Application to the Beam Maser”. In: *Proceedings of the IEEE* 51.1 (1963).

[Jos62] Brian David Josephson. “Possible new effects in superconductive tunnelling”. In: *Physics letters* 1.7 (1962), pp. 251–253.

[Kar+09] RB Karabalin et al. “Piezoelectric nanoelectromechanical resonators based on aluminum nitride thin films”. In: *Applied Physics Letters* 95.10 (2009).

[Kau78] Richard L Kautz. “Picosecond pulses on superconducting striplines”. In: *Journal of Applied Physics* 49.1 (1978), pp. 308–314.

[Kim+21] Sunmi Kim et al. “Enhanced coherence of all-nitride superconducting qubits epitaxially grown on silicon substrate”. In: *Communications Materials* 2.1 (2021), p. 98.

[Kja+20] Morten Kjaergaard et al. “Superconducting qubits: Current state of play”. In: *Annual Review of Condensed Matter Physics* 11.1 (2020), pp. 369–395.

[Koc+07] Jens Koch et al. “Charge-insensitive qubit design derived from the Cooper pair box”. In: *Physical Review A—Atomic, Molecular, and Optical Physics* 76.4 (2007), p. 042319.

[Kop+07] PJ Koppinen, LM Väistö, and IJ Maasilta. “Complete stabilization and improvement of the characteristics of tunnel junctions by thermal annealing”. In: *Applied physics letters* 90.5 (2007).

[Kra+19] Philip Krantz et al. “A quantum engineer’s guide to superconducting qubits”. In: *Applied physics reviews* 6.2 (2019).

[Kru+06] Jerzy Krupka et al. “Measurements of permittivity, dielectric loss tangent, and resistivity of float-zone silicon at microwave frequencies”. In: *IEEE Transactions on microwave theory and techniques* 54.11 (2006), pp. 3995–4001.

[Lan+82] L. D. Landau et al. *Mechanics*. 3rd ed. Vol. 1. Oxford: Elsevier Science & Technology, 1982.

[Lee+24] Yeonkyu Lee et al. “Influence of the reactive gas mixture on the superconducting properties of nitrogen-doped aluminum thin films”. In: *Materials Science and Engineering: B* 310 (2024), p. 117716.

[Lég+19] Sébastien Léger et al. “Observation of quantum many-body effects due to zero point fluctuations in superconducting circuits”. In: *Nature Communications* 10.1 (2019), p. 5259.

[Lev+19] Florence Levy-Bertrand et al. “Electrodynamics of granular aluminum from superconductor to insulator: Observation of collective superconducting modes”. In: *Physical Review B* 99.9 (2019), p. 094506.

[Lic98] James J Licari. *Hybrid microcircuit technology handbook: materials, processes, design, testing and production*. Elsevier, 1998.

[Lol+15] Jared Lolli et al. “Ancillary qubit spectroscopy of vacua in cavity and circuit quantum electrodynamics”. In: *Physical review letters* 114.18 (2015), p. 183601.

[Lóp+25] David López-Núñez et al. “Magnetic penetration depth of aluminum thin films”. In: *Superconductor Science and Technology* (2025).

[Lóp24] David López Núñez. “Coherent Flux Qubits for Quantum Annealing”. PhD thesis. Universitat de Barcelona, 2024.

[Mag+18] Luca Magazzù et al. “Probing the strongly driven spin-boson model in a superconducting quantum circuit”. In: *Nature communications* 9.1 (2018), p. 1403.

[Mag+21] L Magazzù, P Forn-Díaz, and M Grifoni. “Transmission spectra of the driven, dissipative Rabi model in the ultrastrong-coupling regime”. In: *Physical Review A* 104.5 (2021), p. 053711.

[Mal+18] Nataliya Maleeva et al. “Circuit quantum electrodynamics of granular aluminum resonators”. In: *Nature communications* 9.1 (2018), p. 3889.

[Man+09] Vladimir E Manucharyan et al. “Fluxonium: Single cooper-pair circuit free of charge offsets”. In: *Science* 326.5949 (2009), pp. 113–116.

[Man+17] Vladimir E Manucharyan, Alexandre Baksic, and Cristiano Ciuti. “Resilience of the quantum Rabi model in circuit QED”. In: *Journal of Physics A: Mathematical and Theoretical* 50.29 (2017), p. 294001.

[Man12] VE Manucharyan. “Superinductance ph. d”. PhD thesis. thesis Yale University, 2012.

[Mas+12] Nicholas A Masluk et al. “Microwave Characterization of Josephson Junction Arrays: Implementing a Low Loss Superinductance”. In: *Physical review letters* 109.13 (2012), p. 137002.

[Maz05] Benjamin A Mazin. *Microwave kinetic inductance detectors*. California Institute of Technology, 2005.

[McR+20] Corey Rae Harrington McRae et al. “Materials loss measurements using superconducting microwave resonators”. In: *Review of Scientific Instruments* 91.9 (2020).

[Mil22] Vladimir Milchakov. “Optimized transmon molecule for high fidelity quantum non demolition readout using cross-Kerr coupling”. PhD thesis. Université Grenoble Alpes [2020-....], 2022.

[Mor90] John Stephen Morgan. *Properties of sputtered thin films of indium nitride and aluminum nitride*. The Johns Hopkins University, 1990.

[Mos+23] Dmitry O Moskalev et al. “Optimization of shadow evaporation and oxidation for reproducible quantum Josephson junction circuits”. In: *Scientific Reports* 13.1 (2023), p. 4174.

[Mül+22] Manuel Müller et al. “Magnetic field robust high quality factor NbTiN superconducting microwave resonators”. In: *Materials for Quantum Technology* 2.1 (2022), p. 015002.

[Nak+11] Yasunobu Nakamura et al. “Superconducting qubits consisting of epitaxially grown NbN/AlN/NbN Josephson junctions”. In: *Applied Physics Letters* 99.21 (2011).

[Nak+99] Yasunobu Nakamura, Yu A Pashkin, and JS Tsai. “Coherent control of macroscopic quantum states in a single-Cooper-pair box”. In: *nature* 398.6730 (1999), pp. 786–788.

[Ngu+19] Long B Nguyen et al. “High-coherence fluxonium qubit”. In: *Physical Review X* 9.4 (2019), p. 041041.

[Nie+10] Thomas Niemczyk et al. “Circuit quantum electrodynamics in the ultrastrong-coupling regime”. In: *Nature Physics* 6.10 (2010), pp. 772–776.

[Nie+19] David Niepce, Jonathan Burnett, and Jonas Bylander. “High kinetic inductance Nb N nanowire superinductors”. In: *Physical Review Applied* 11.4 (2019), p. 044014.

[Nig+12] Simon E Nigg et al. “Black-box superconducting circuit quantization”. In: *Physical review letters* 108.24 (2012), p. 240502.

[Orl+99] Terry P Orlando et al. “Superconducting persistent-current qubit”. In: *Physical Review B* 60.22 (1999), p. 15398.

[Osm+21] A Osman et al. “Simplified Josephson-junction fabrication process for reproducibly high-performance superconducting qubits”. In: *Applied Physics Letters* 118.6 (2021).

[Paa09] Floortje Geertruida Paauw. *Superconducting Flux Qubits: Quantum Chains Ans Tunable Qubits*. 2009.

[Pau58] Leo J van der Pauw. “A method of measuring the resistivity and Hall coefficient on lamellae of arbitrary shape”. In: *Philips technical review* 20 (1958), pp. 220–224.

[Pel+18] JT Peltonen et al. “Hybrid rf SQUID qubit based on high kinetic inductance”. In: *Scientific reports* 8.1 (2018), p. 10033.

[Per+13] Borja Peropadre et al. “Nonequilibrium and nonperturbative dynamics of ultrastrong coupling in open lines”. In: *Physical review letters* 111.24 (2013), p. 243602.

[Per+20] Matilda Peruzzo et al. “Surpassing the resistance quantum with a geometric superinductor”. In: *Physical Review Applied* 14.4 (2020), p. 044055.

[Pip+53] Alfred Brian Pippard and William Lawrence Bragg. “An experimental and theoretical study of the relation between magnetic field and current in a superconductor”. In: *Proceedings of the Royal Society of London. Series A. Mathematical and Physical Sciences* 216.1127 (1953), pp. 547–568.

[Pla07] Jelle Hendrik Plantenberg. “Coupled supercnducting flux qubits”. PhD thesis. 2007.

[Pla20] Luca Planat. “Resonant and traveling-wave parametric amplification near the quantum limit”. PhD thesis. Université Grenoble Alpes, 2020.

[Pol+23] Magdaléna Poláčková et al. “Probing superconducting granularity using nonlocal four-probe measurements”. In: *The European Physical Journal Plus* 138.6 (2023), pp. 1–8.

[Poo+14] Charles P Poole et al. *Superconductivity*. Elsevier, 2014.

[Pop+12] Ioan Mihai Pop et al. “Fabrication of stable and reproducible submicron tunnel junctions”. In: *Journal of Vacuum Science & Technology B* 30.1 (2012).

[Por15] Shachaf Poran. “Granularity and Disordered Superconductors”. PhD thesis. Bar-Ilan University, 2015.

[Pot+01] A Potts et al. “Novel fabrication methods for submicrometer Josephson junction qubits”. In: *Journal of Materials Science: Materials in Electronics* 12 (2001), pp. 289–293.

[Poz21] David M Pozar. *Microwave engineering: theory and techniques*. John wiley & sons, 2021.

[Pro+15] Sebastian Probst et al. “Efficient and robust analysis of complex scattering data under noise in microwave resonators”. In: *Review of Scientific Instruments* 86.2 (2015).

[Rab36] II Rabi. “On the process of space quantization”. In: *Physical Review* 49.4 (1936), p. 324.

[Ree+10] Matthew D Reed et al. “High-Fidelity Readout in Circuit Quantum Electrodynamics Using the Jaynes-Cummings Nonlinearity”. In: *Physical review letters* 105.17 (2010), p. 173601.

[Rie+23] D Rieger et al. “Granular aluminium nanojunction fluxonium qubit”. In: *Nature Materials* 22.2 (2023), pp. 194–199.

[Rip22] Juan José García Ripoll. *Quantum information and quantum optics with superconducting circuits*. Cambridge University Press, 2022.

[Ris+13] Diego Ristè et al. "Millisecond charge-parity fluctuations and induced decoherence in a superconducting transmon qubit". In: *Nature communications* 4.1 (2013), p. 1913.

[Rob+06] TL Robertson et al. "Quantum theory of three-junction flux qubit with non-negligible loop inductance: Towards scalability". In: *Physical Review B—Condensed Matter and Materials Physics* 73.17 (2006), p. 174526.

[Ros+17a] D Rosenberg et al. "3D integrated superconducting qubits". In: *npj quantum information* 3.1 (2017), p. 42.

[Ros+17b] Daniel Z Rossatto et al. "Spectral classification of coupling regimes in the quantum Rabi model". In: *Physical Review A* 96.1 (2017), p. 013849.

[Rot+16] H Rotzinger et al. "Aluminium-oxide wires for superconducting high kinetic inductance circuits". In: *Superconductor Science and Technology* 30.2 (2016), p. 025002.

[Sag+11] Jeremy M Sage et al. "Study of loss in superconducting coplanar waveguide resonators". In: *Journal of Applied Physics* 109.6 (2011).

[Sam+16] Nodar Samkharadze et al. "High-kinetic-inductance superconducting nanowire resonators for circuit QED in a magnetic field". In: *Physical Review Applied* 5.4 (2016), p. 044004.

[Scu+97] Marlan O Scully and M Suhail Zubairy. *Quantum optics*. Cambridge university press, 1997.

[She+18] Abigail Shearrow et al. "Atomic layer deposition of titanium nitride for quantum circuits". In: *Applied Physics Letters* 113.21 (2018).

[Sid21] Irfan Siddiqi. "Engineering high-coherence superconducting qubits". In: *Nature Reviews Materials* 6.10 (2021), pp. 875–891.

[Sil+67] AH Silver and JE Zimmerman. "Quantum states and transitions in weakly connected superconducting rings". In: *Physical Review* 157.2 (1967), p. 317.

[Smi+16] WC Smith et al. "Quantization of inductively shunted superconducting circuits". In: *Physical Review B* 94.14 (2016), p. 144507.

[Som+23] Aaron Somoroff et al. "Millisecond coherence in a superconducting qubit". In: *Physical Review Letters* 130.26 (2023), p. 267001.

[Ste+10] Matthias Steffen et al. "High-coherence hybrid superconducting qubit". In: *Physical review letters* 105.10 (2010), p. 100502.

[Tin04] Michael Tinkham. *Introduction to superconductivity*. Courier Corporation, 2004.

[Tom+21] Akiyoshi Tomonaga et al. "Quasiparticle tunneling and 1/f charge noise in ultrastrongly coupled superconducting qubit and resonator". In: *Physical Review B* 104.22 (2021), p. 224509.

[Tom+25] A Tomonaga et al. "Spectral properties of two superconducting artificial atoms coupled to a resonator in the ultrastrong coupling regime". In: *Nature Communications* 16.1 (2025), pp. 1–8.

[Tor+] Alba Torras-Coloma, P. Forn-Díaz, and J.J. Garcia-Ripoll. In preparation.

[Tor+24] Alba Torras-Coloma et al. "Superconducting nitridized-aluminum thin films". In: *Superconductor Science and Technology* 37.3 (2024), p. 035017.

[Tor+25] Alba Torras-Coloma et al. "Superinductor-based ultrastrong coupling in a superconducting circuit". In: *preprint arXiv:2507.09339* (2025).

[Tor25] Torras-Coloma, Alba. *Electric dipole moment of a flux qubit*. 2025. URL: `https://github.com/atorras97/electric-dipole-moment/tree/main`.

[Ulb+21] Gerhard Ulbricht, Mario De Lucia, and Eoin Baldwin. "Applications for microwave kinetic induction detectors in advanced instrumentation". In: *Applied Sciences* 11.6 (2021), p. 2671.

[Vag+93] Ruggero Vaglio et al. "Explanation of the resistance-peak anomaly in nonhomogeneous superconductors". In: *Physical Review B* 47.22 (1993), p. 15302.

[Val+19] Francesco Valenti et al. "Interplay between kinetic inductance, nonlinearity, and quasiparticle dynamics in granular aluminum microwave kinetic inductance detectors". In: *Physical review applied* 11.5 (2019), p. 054087.

[Van+00] Caspar H Van Der Wal et al. "Quantum superposition of macroscopic persistent-current states". In: *Science* 290.5492 (2000), pp. 773–777.

[Vis+10] Michael R Vissers et al. "Low loss superconducting titanium nitride coplanar waveguide resonators". In: *Applied Physics Letters* 97.23 (2010).

[Wal+06] Herbert Walther et al. "Cavity quantum electrodynamics". In: *Reports on Progress in Physics* 69.5 (2006), p. 1325.

[Wan+25] Fei Wang et al. “High-coherence fluxonium qubits manufactured with a wafer-scale-uniformity process”. In: *Physical Review Applied* 23.4 (2025), p. 044064.

[Web+17] Steven J Weber et al. “Coherent coupled qubits for quantum annealing”. In: *Physical Review Applied* 8.1 (2017), p. 014004.

[Wer+95] W Wernsdorfer et al. “High sensitivity magnetization measurements of nanoscale cobalt clusters”. In: *Journal of Applied Physics* 78.12 (1995), pp. 7192–7195.

[Win+20] Patrick Winkel et al. “Implementation of a transmon qubit using superconducting granular aluminum”. In: *Physical Review X* 10.3 (2020), p. 031032.

[Wis+10] David S Wisbey et al. “Effect of metal/substrate interfaces on radio-frequency loss in superconducting coplanar waveguides”. In: *Journal of Applied Physics* 108.9 (2010).

[Yan+16] Fei Yan et al. “The flux qubit revisited to enhance coherence and reproducibility”. In: *Nature communications* 7.1 (2016), p. 12964.

[Yan+20] Fei Yan et al. “Engineering framework for optimizing superconducting qubit designs”. In: *arXiv preprint arXiv:2006.04130* (2020).

[Ye+21] Yufeng Ye et al. “Engineering purely nonlinear coupling between superconducting qubits using a quarton”. In: *Physical Review Letters* 127.5 (2021), p. 050502.

[Ye+24] Yufeng Ye et al. “Ultrafast superconducting qubit readout with the quarton coupler”. In: *Science Advances* 10.41 (2024), eado9094.

[Yos+06] F Yoshihara et al. “Decoherence of flux qubits due to 1/f flux noise”. In: *Physical review letters* 97.16 (2006), p. 167001.

[Yos+17a] Fumiki Yoshihara et al. “Characteristic spectra of circuit quantum electrodynamics systems from the ultrastrong-to the deep-strong-coupling regime”. In: *Physical Review A* 95.5 (2017), p. 053824.

[Yos+17b] Fumiki Yoshihara et al. “Superconducting qubit–oscillator circuit beyond the ultrastrong-coupling regime”. In: *Nature Physics* 13.1 (2017), pp. 44–47.

[Zap+24] Nicolas Zapata et al. “Granular aluminum parametric amplifier for low-noise measurements in tesla fields”. In: *Physical Review Letters* 133.26 (2024), p. 260604.

[Zha+19] Wenyuan Zhang et al. “Microresonators fabricated from high-kinetic-inductance aluminum films”. In: *Physical Review Applied* 11.1 (2019), p. 011003.